Photon Management for Thin-Film Quantum Dot Solar Cells


Doctoral Dissertation
Doctoral Program in Electrical, Electronics, and Communications Enginering
(32nd cycle)

Photon Management for Thin-Film Quantum Dot Solar Cells

Farid Elsehrawy

* * * * * *

Supervisor
Prof. Federica Cappelluti

Doctoral Examination Committee
Prof. Lucio Andreani, Referee, Università di Pavia
Prof. Antonio Martí, Referee, Universidad Politécnica de Madrid
Dr. Andrea Cattoni, French National Centre for Scientific Research
Prof. Michele Goano, Politecnico di Torino
Prof. Marko Topič, University of Ljubljana

Politecnico di Torino
June 22nd, 2020

Acknowledgments

First and foremost, I would like to express my deepest gratitude to my doctoral thesis advisor, Prof. Federica Cappelluti. Without her persistent guidance and patience, this work would not have been possible. She has been and will continue to be my greatest mentor.

I gratefully acknowledge the vital technical contributions of Dr. Alberto Tibaldi, which enabled many of our research endeavors to materialize. I am forever thankful to Prof. Michele Goano and Andrea Palmieri for their friendly support and assistance throughout my doctoral studies.

I want to thank our colleagues at the Tampere University, whose contributions were indispensable to the success of the TFQD project. I would like to thank Timo Aho for his invaluable experimental work and for always sharing insightful suggestions. I wish to thank Prof. Tapio Niemi and Prof. Mircea Guina for their continuous support and for hosting me at the TU research facilities during my mobility periods.

Finally, I am forever indebted to my family, without whom I would not be here. I wish to thank my loving, supportive parents who always provided me with inspiration and encouragement to pursue this. I am grateful to my brother and my sister for always being there for me. I want to express my most sincere appreciation to my loving wife, Hedayat, who constantly supported me throughout this journey.

Abstract

The demand for a source of renewable energy has been the driving force to achieve significant advancements in the field of photovoltaic energy generation during the past decades. To reach the goal of solar cell efficiency enhancement, the development of novel materials is a strategy of paramount importance. Research towards multijunction solar cells has resulted in record-breaking efficiencies, at the expense of structural complexity and high cost. A promising concept to overcome this is the use of quantum dots embedded within the cell active region to absorb lower energy photons in the near infrared region that would otherwise not be absorbed by the main cell. The resulting quantum dot solar cells (QDSCs) therefore enable an increase in the short-circuit current while theoretically maintaining a high open-circuit voltage, assuming perfect material growth. However, QDSCs suffer from limitations such as the low absorption of the QD layer stack and the difficulty in growing a large number of layers to compensate for the low absorption. In fact, increasing the number of layers in the stack results in an increasingly large reduction of the open circuit voltage.

Light trapping is a photon management technique used to enhance the effective optical path length of the solar cell in order to increase the photogeneration in thin or low absorbing QD layers. The potential optical path length enhancement is dependent on the refractive index of the active region material, and for III-V solar cells it turns into an enhancement of approximately fifty times. Owing to the fact that light trapping enables the use of thin-film cells by reducing the active region thickness keeping the same short-circuit current density, it allows for reduced volume recombination loss and can result in higher open-circuit voltage. Finally, light trapping-enhanced thin-film cells exhibit a high power-to-weight ratio, which is a desirable feature for space power sources.

The research presented in this dissertation was undertaken as part of the European H2020 project Thin-Film Quantum Dot (TFQD) photovoltaic cells. The project aimed to develop light-trapping enhanced TFQD cells as an enabling technology for lightweight, flexible, high-efficiency space solar arrays. The project involved multiple academic as well as industrial partners, and allowed the candidate to undertake two mobility periods at the Tampere University in order to participate in experimental characterization activities.

The scope of the studies in this dissertation covers the investigation of different photon management techniques to enhance the photoabsorption of thin-film QDSCs. Additionally, an approach to the self-consistent electro-optical modelling of light-trapping enhanced solar cells is investigated as an enabling tool for the optimization of such cells.

The introduction (Chapter 1) provides a brief overview about thin-film solar cells. The theory behind light trapping is described, where the enhancement limits are derived. An introduction to QDSCs is also provided to contextualize the requirement for light trapping methods.

The first study investigates light trapping-enhanced III-V QDSCs incorporating back-side diffraction gratings. The gratings are designed and optimized to efficiently diffract the light towards high-order modes using full-wave electromagnetic simulations implementing the rigorous coupled wave analysis method. The optimization is performed with the target of enhancing interband photoabsorption in the near infrared region. Nanostructured anti-reflection coatings are also studied with the aim of increasing the fraction of light injected into the cell and reducing front-side surface reflectance. It is then demonstrated using simulations that light trapping effectiveness can be improved in double-sided nanostructured cells, owing to the interplay between the diffraction grating and antireflection coating. Prototype diffraction gratings were fabricated by nanoimprint lithography on GaAs wafer. Efficient diffraction of light was observed in both simulated and experimental results using periodic gratings, allowing for the validation of the modelling appoach and the proof of concept of the designed structures.

The following study aims to improve the absorption of low-energy photons for QDSCs working in the intermediate band regime, where mid-far infrared photoabsorption is low. Guided-mode resonance effects may enable large enhancement of QD intraband optical transitions. Ultra thin-film QDSCs are designed to have significant field waveguiding in the QD stack region and patterned at the rear-side with a sub-wavelength diffraction grating. Remarkable increase of the optical path length at mid-infrared wavelengths is shown owing to guided-mode resonances. Design guidelines are presented for typical energy and strength of the second-photon absorption of III-V QDs, such as InAs/GaAs and GaSb/GaAs.

The design of the aforementioned periodic photonic structures generally requires 2D or 3D full-wave approaches that are difficult to combine in a self-consistent fashion with electronic transport models to fully account for carrier collection and carrier-photon interactions. A novel and computationally efficient multiphysics approach is presented for coupled electrical-optical simulations, based on the multimodal scattering matrix formalism, wherein the grating is modelled by a scattering matrix that can be derived from simulations performed by the rigorous coupled wave analysis method.

Contents

Chapter 1

Introduction

III-V semiconductors have allowed the development of the highest performing single-junction solar cells due to their superior optical and transport properties, as well as the maturity of their processing technology. Single junction GaAs solar cells hit a record efficiency of 29.1% [1], approaching the Shockley-Queisser (SQ) limit [2] of 33.5% under the standard terrestrial solar spectrum AM1.5G. The SQ limit determines the highest obtainable efficiency by a single-junction solar cell based on the material energy bandgap and the incident solar spectrum. The energy bandgap sets the minimum photon energy necessary to be converted into free charge carriers as well as the maximum energy of those carriers, with the excess photon energy lost through thermalization processes. The solar cell efficiency can exceed the SQ limit by stacking multiple individual cells, each selectively absorbing a fraction of the solar spectrum [3]. The resulting multi-junction solar cell (MJSC) has a maximum theoretical efficiency of 67% under the AM1.5G spectrum [4]. The subcells in MJSCs are commonly connected in series through tunnel diodes, which limits the maximum current of the solar cell to that of the subcell producing the lowest current. Accordingly, it is necessary to design the subcells to provide similar photocurrents while using lattice matched materials for higher quality of the epitaxial growth [5]. Other approaches such as wafer-bonded solar cells have also been developed. The current highest efficiency solar cell uses a multi-junction configuration to provide an efficiency exceeding 46% [1], and further improvement is still possible.

Despite the prevalence of silicon-based solar cells at the terrestrial level, III-V solar cells are dominant in space applications due to their high power-to-weight ratio, high radiation tolerance, and resistance to temperature changes. Current research towards the development of III-V solar cells aims to increase their output power while reducing the production costs. Thin-film configurations based on epitaxial lift-off (ELO) technologies are promising to reduce the amount of active material used (and therefore the cost) as well as resulting in a significantly improved power-to-weight ratio due to the large optical thickness of III-V materials [6]. One

drawback of MJSCs is their high cost due to the complexity of the fabrication process. This necessitates the use of novel materials for the development of high-efficiency, thin-film solar cells at a reasonable cost. Nanostructured absorbers such as quantum well (QW) and quantum dot (QD) materials offer a promising path towards the development of novel photovoltaics concepts, beyond the SQ limit, such as the intermediate band (IB) solar cell [7].

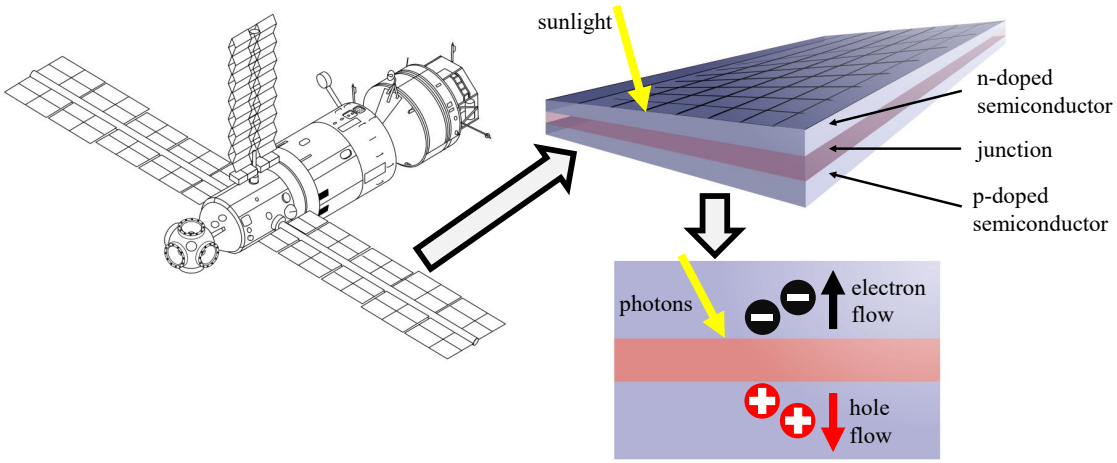

Figure 1.1: Solar cells geared towards space applications. The basic structure of a solar cell junction is shown, with the junction producing free charge carriers when illuminated.

1.1 Basics of photovoltaics

The basic solar cell structure consists of a $p-n$ junction that converts photons into charge carriers, as shown in Fig. 1.1. Light absorption results when photons are incident with an energy greater than that of the semiconductor material bandgap (E_g). The absorption process results in raising the energy of an electron from the valence band (VB) to the conduction band (CB), creating an electron-hole pair. The photogenerated carriers collected at the contacts will deliver energy to the load. However, a fraction of them undergo recombination in the bulk or at the surface of the device.

Charge carriers may recombine radiatively, with the relaxation of an electron from the CB to the VB and emission of a photon with bandgap energy. Alternatively, non-radiative recombination mechanisms may take place, where the released energy is instead transferred to other charge carriers (Auger recombination) or to

phonons (impurity recombination) [8]. Auger recombination occurs when the released energy by a recombination event is transferred to another carrier as kinetic energy and then lost through collisions with phonons. Impurity recombination is the dominant non-radiative recombination mechanism in III-V semiconductors under low injection conditions, and is primarily caused by defects in the semiconductor crystal that lead to electron states in the forbidden zone trapping the charge carriers.

For charge carriers that do not recombine and instead reach the contacts of the solar cell, a photocurrent is generated. When the cell is connected to a load, the photocurrent flow through the load causes the onset of a forwad bias across the cell: a current which opposes to the photocurrent is generated. Therefore, the net current across the solar cell, I, can be expressed as:

$$I = -I_s(e^{\frac{q_{\mathrm{el}}V}{\eta k_{\mathrm{B}}T}} - 1) + I_{\mathrm{SC}} \tag{1.1}$$

where I_s is the reverse saturation current, q_{el} the elementary charge constant, V the voltage of the solar cell, η the ideality factor, k_B the Boltzmann constant, T the temperature, and I_{SC} the light-induced current.

The reverse saturation current characterizes the solar cell behavior under dark and reverse bias condition. The ideality factor (in general, voltage dependent) provides insight towards the recombination mechanisms in the solar cell, where a cell exhibiting $\eta \approx 1$ is dominated by recombination in the quasi-neutral regions, while a cell operating exhibiting $\eta \approx 2$ is dominated by non-radiative recombination in the space charge region.

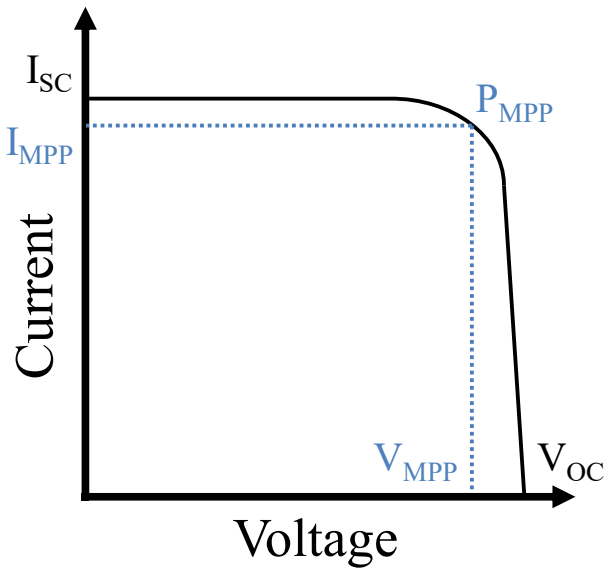

Figure 1.2: Current-voltage characteristic of a solar cell.

The current-voltage characteristic from Equation 1.1 is shown in Fig. 1.2. At open-circuit conditions (I=0), the open-circuit voltage V_{OC} can be derived. The V_{OC} sets the condition wherein the forward bias current (usually referred to as dark current) and the photocurrent cancel out. The maximum power, P_{MPP}, is generated when the product of the current and voltage is maximized, corresponding to the maximum power point (MPP) voltage (V_{MPP}) and current (I_{MPP}). The ratio of the maximum power rectangle area to the area of the rectangle identified by I_{SC} and V_{OC} corresponds to the solar cell fill factor (FF) which is defined as:

$$FF = \frac{I_{MPP}V_{MPP}}{I_{\mathrm{SC}}V_{\mathrm{OC}}} \tag{1.2}$$

Combining the previously mentioned metrics, the overall conversion efficiency of a solar cell can then be calculated as:

$$\text{Efficiency} = \frac{V_{\mathrm{OC}}I_{\mathrm{SC}}FF}{P_{sun}} \tag{1.3}$$

P_{sun} being the incident power density from the sun. The different solar irradiance spectra are shown in Fig. 1.3 classified according to the Air Mass (AM).

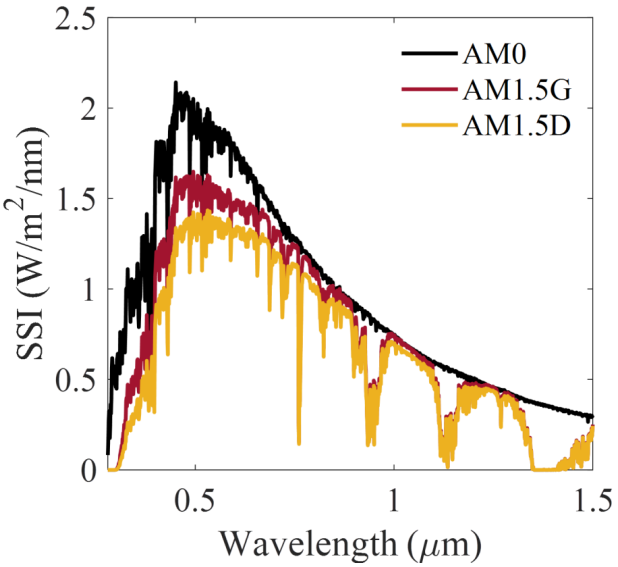

Figure 1.3: Solar spectral irradiance (SSI) for space/extraterrestrial (AM0), terrestrial (AM1.5G), and concentration (AM1.5D) conditions.

In order to facilitate the comparison between cells of different sizes, the short-circuit current density (J_{SC}) is generally used as a reference. The photogenerated short-circuit current density (occasionally referred to as the photocurrent density), can be expressed as:

$$J_{\mathrm{SC}} = \int_{\lambda_i}^{\lambda_f} q_{\mathrm{el}} SPF(\lambda) EQE(\lambda)\,\mathrm{d}\lambda = \int_{\lambda_i}^{\lambda_f} q_{\mathrm{el}} A(\lambda) SPF(\lambda) IQE\,\mathrm{d}\lambda \tag{1.4}$$

where λ is the wavelength, $A(\lambda)$ the absorbance in the active region, SPF the spectral photon flux, EQE the external quantum efficiency, and IQE the internal quantum efficiency. The short-circuit current density is computed by integrating the ratio of photons absorbed in the active region of the solar cell over the wavelength range of interest, weighted by the incident solar spectrum. The incident photon flux is evaluated from a specific air mass solar irradiance as spectral solar irradiance (SSI) divided by photon energy ($h\nu$) as:

$$SPF(\lambda) = \frac{SSI(\lambda)}{h\nu} \tag{1.5}$$

The internal quantum efficiency is the collection efficiency of the generated charge carriers. By assuming that each absorbed photon produces one electron-hole pair, i.e. that the quantum yield is one, the IQE is defined as:

$$IQE = \frac{\text{no. of collected charge carriers}}{\text{no. of photons absorbed by the cell}} \tag{1.6}$$

The external quantum efficiency is a more inclusive metric that accounts for optical and electric efficiency loss mechanisms, defined as:

$$EQE = \frac{\text{no. of collected charge carriers}}{\text{no. of photons incident on the cell}} = A(\lambda)\, IQE \tag{1.7}$$

A high E_g results in a smaller J_{SC} as the material is not capable of absorbing low energy photons. For example, the bandgap energy of GaAs is approximately 1.4 eV (corresponding to $\lambda \approx$900 nm), which results in no absorption below the band edge for photons with $E_g < 1.4$ eV ($\lambda > 900$ nm). The maximum open-circuit voltage is proportional to the bandgap of the material, making a high E_g material more favorable for high V_{OC}. This leads to a trade-off between V_{OC} and J_{SC} optimization, so that the energy gap resulting in highest efficiency for a single-gap solar cell is in the range of the energy gap of silicon and GaAs, as shown by the Shockley-Queisser efficiency vs. energy gap curves reported in Fig. 1.4 [2].

1.2 Light trapping-enabled thin-film solar cells

III-V cells require a minimum thickness of a few micrometers to absorb almost all the light going through the cell once, i.e. in a single-pass configuration [9]. III-V materials exhibit an optical thickness larger than that of silicon, which instead requires a few hundred micrometers to achieve the same result. To fully exploit

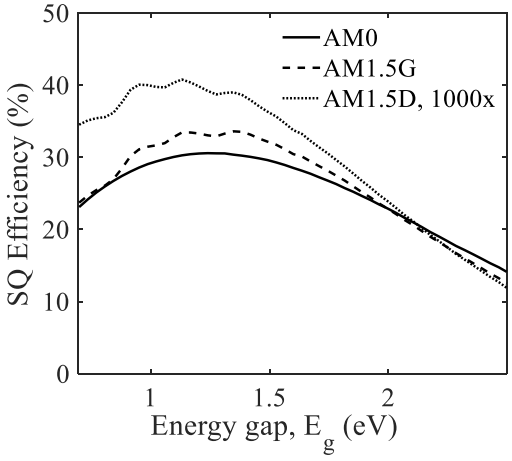

Figure 1.4: The SQ efficiency limit relative to the semiconductor bandgap energy (E_g) is shown for single-gap solar cells at AM0, AM1.5G, and 1000×AM1.5D illumination.

the potential advantage of thin film architectures, a marked reduction of the active region thickness can be pursued provided that the Optical Path Length (OPL) is substantially increased using light trapping approaches.

Developing strategies for light trapping is a growing research topic that encompasses a wide spectrum of photovoltaic technologies. In solar cells realized with high-quality semiconductors, light trapping allows for enhanced efficiency at lower cost by reducing the required material consumption. Light trapping concepts allow the use of a thin active region while maintaining constant short-circuit current, thereby minimizing volume recombination losses. This enables a higher open circuit voltage and overall external quantum efficiency [10, 11, 12].

On the other hand, for devices based on materials with an unfavorable diffusion length to absorption length ratio such as organics, polycrystalline and amorphous semiconductors, light trapping enables maximizing the optical absorption length while minimizing the electrical length for carrier preservation. Light trapping-enhanced harvesting is also going to play a major role in the development of next-generation photovoltaic concepts featuring quantum-confined materials such as QWs and QDs, which typically suffer from low light absorption [13, 14, 15].

The simplest form of light trapping can be implemented by adding a back-side reflector to the cell, which doubles the OPL. The $J-V$ characteristics of an ideal thin-film GaAs solar cell are shown in Fig. 1.5 (a), where the reflector results in an increased OPL through the cell, enabling more photons to be absorbed and leading to a higher J_{SC}. The EQE, shown in Fig. 1.5 (b) demonstrates the increased photon absorption around the GaAs bandgap at $\lambda \approx 900$ nm.

A common method to evaluate the impact of light trapping is the calculation

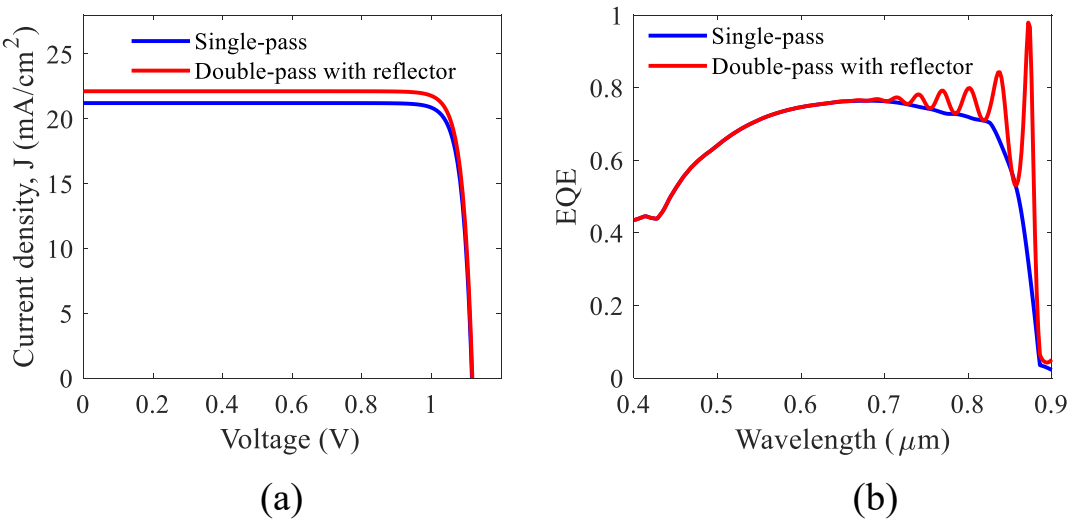

Figure 1.5: (a) The $J-V$ characteristics and (b) EQE of an ideal thin-film GaAs solar cell with (red) and without (blue) a back-side reflector. The solar cell active region thickness is 2 μm.

of the photocurrent density enhancement factor of a light trapping sample relative to a reference sample, in particular at the long wavelengths where the material is weakly absorbing. The enhancement factor is simply the ratio of the photocurrent densities of the different samples as $J_{\mathrm{SC,LT}}/J_{\mathrm{SC,REF}}$.

The performance of diverse light trapping structures can be compared with reference to the maximum enhancement limit proposed in [16]. For an ideal Lambertian scattering surface on the cell back-side, as shown in Fig. 1.6 (a), light is isotropically scattered within the structure at all diffraction angles from $\theta = 0°$ to $\theta = 90°$. Diffracted rays at an angle higher than that of the escape cone are internally reflected and propagate within the device, while rays diffracted within the escape cone may be transmitted out of the solar cell. The escape cone angle θ_c can be given by:

$$\theta_c = \sin^{-1}(1/n) \tag{1.8}$$

where n is the refractive index of the material and incidence from air is assumed.

Thereby, the OPL of a solar cell is enhanced due to the light rays trapped within the cell active region. First, the ratio of the light rays escaping the cell to the total incoming light is examined, which can be expressed as:

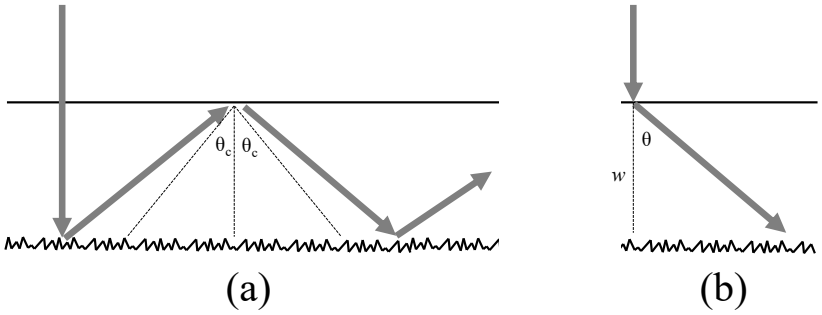

Figure 1.6: (a) The behavior of light when it is diffracted within the escape cone (θ<θ_c) due to a Lambertian scattering surface. (b) The average distance traveled by light within a solar cell of thickness w.

$$f = \frac{\int_0^{\theta_c} B\cos\theta\sin\theta d\theta}{\int_0^{\frac{\pi}{2}} B\cos\theta\sin\theta d\theta} = \sin^2\theta_c = \frac{1}{n^2} \tag{1.9}$$

with B being the intensity per solid angle of the light ray inside the active material [17]. Next, the OPL of the diffracted light is studied. For a solar cell with a thickness w, normally incident light will travel an average distance of w, in the case without a back-side reflector. A ray diffracted at an angle of θ will then travel an average distance of $w/\cos\theta$ for a single pass through the solar cell. It is then possible to express the average path length of a single pass through the solar cell for all the light rays diffracted by a Lambertian scattering surface as:

$$w_{eff} = \frac{\int_0^{\frac{\pi}{2}} \frac{w}{\cos\theta_c}\sin\theta d\theta}{\int_0^{\frac{\pi}{2}} \cos\theta\sin\theta d\theta} = 2w \tag{1.10}$$

For a structure with a randomized front surface combined with a back-side reflector of reflectivity R, the Lambertian limit can be derived by evaluating the path length of all possible rays propagating within the cell. The average path length P of weakly absorbed light is expressed as:

$$\begin{aligned} \overline{P} &= w[2(1-R) + 4fR + 6R(1-f)(1-R) + 8f(1-f)R^2 + ...] \\ &= 2w(\sum_{N=0}^{\infty}[(2N+1)(1-R) + (2N+2)fR][R(1-f)]^N) \end{aligned} \tag{1.11}$$

where f is the fraction of light escaping from the front surface. By utilizing the power series expansion of $1/(1-x)$, Equation 1.11 is reduced to:

$$\overline{P} = \frac{2w(1+R)}{[1-R(1-f)]} \tag{1.12}$$

In the ideal case for light trapping, the front surface has unity transmissivity ($f = 1/n^2$) and the back-side reflector is assumed to be perfect ($R = 1$). This allows the derivation of the maximum OPL enhancement of $4n^2$ due to the use of a Lambertian scatterer with a back-side reflector [16, 17, 9]. For the case without a back-side reflector, the reflectivity is assumed to be $1 - f$, resulting in an OPL enhancement of $2n^2$.

By applying the effective OPL to the Shockley-Queisser limit [2], the dependence of the solar cell metrics on the active region thickness for a GaAs solar cell can be computed using the method in [18], as shown in Fig. 1.7. The planar structure with a single-pass of light through the cell has OPL=1, the mirror structure resulting in a double-pass has OPL=2, and the textured surface demonstrating full light trapping has OPL=$4n^2$. Figure 1.7 (b) demonstrates the impact of OPL enhancement on J_{SC} due to the incorporation of a textured surface for active regions with low absorption lengths. The mirror structure provides up to 7% improvement of J_{SC} as the GaAs active region thickness approaches 1μm, which corresponds to a conversion efficiency enhancement of a few percentage points. For thinner active regions of 300 nm, the potential enhancement is significantly higher, i.e. over 50% increase in J_{SC} by using the texturing compared to that of the planar configuration, which would ideally boost the conversion efficiency by up to 10%. On the contrary, a thicker active region results in diminishing gain from light trapping. As anticipated, the impact of light trapping is notable for small active material thicknesses or low absorbing materials.

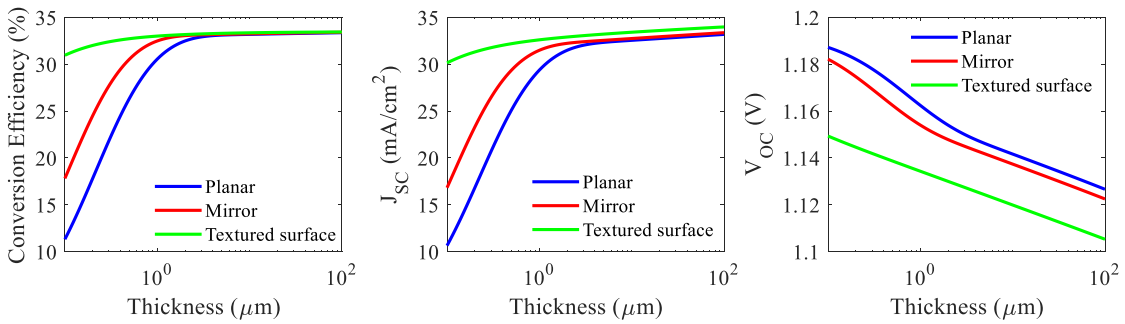

Figure 1.7: The SQ limit to (a) conversion efficiency, (b) J_{SC}, and (c) V_{OC} is shown against the active region thickness for a typical GaAs solar cell with a single-pass planar configuration (blue), double-pass mirror configuration (red), and full light trapping with a Lambertian textured surface (green). The figures are produced using the method in [18].

Several photon management techniques have been previously investigated for light trapping in photovoltaics. These techniques include, but are not limited to, randomly-textured scattering surfaces [19, 20, 21, 22], plasmonic structures [23, 24, 25], photonic crystals [26, 27], resonant waveguiding structures [28, 29], and diffraction gratings [11, 30]. The mechanism of optical enhancement may drastically vary based on the method. For instance, randomly-textured surface scatter the light inside the cell at a multitude of angles while diffraction gratings couple light into well-defined high order modes whose excitation can be controlled by grating features such as period, aspect ratio, and material. Plasmonic structures rely on the interaction of surface plasmon polaritons (SPP) at metallic surfaces to produce electromagnetic resonances that can be harvested. The diverse methodologies share the common aim of maximizing the photon absorption in the cell active region to result in the highest possible J_{SC}.

One of the most promising strategies for light trapping is the patterning of the solar cell surface(s) with semiconductor or dielectric periodic diffraction gratings [11, 12, 31, 32, 33]. Diffraction gratings directly etched on the back-side of wafer-based QD-IBSCs were theoretically studied in [34], pointing out the potential for a large increase of the intraband absorption for QD cells much thicker than the sun radiation coherence length.

Uni-periodic and bi-periodic gratings allow the excitation of high order diffraction modes, with the design constraint being that the grating period must be larger than the incident wavelength. The angle of propagation of the diffracted mode is defined by the grating equation which reads:

$$n_1 \sin\theta_{1,m} = n_2 \sin\theta_{2,m} = \frac{m\lambda}{\Lambda} \tag{1.13}$$

where θ is the medium-dependent angle of propagation, m is the integer grating order, λ is the wavelength of propagating light, and Λ is the grating period. The subscript 1 refers to the incident medium and subscript 2 refers to the grating. Designing diffraction gratings to enable light trapping requires coupling most of the incident light to diffraction orders that will propagate outside of the escape cone ($\theta > \theta_c$) in the cell's absorbing region, as shown in Fig. 1.8 for a uni-periodic grating. Diffraction gratings with large period (with respect to the wavelength) are less wavelength-sensitive than small period gratings due to the higher number of propagating modes, a characteristic which is critical to achieve light trapping for thin-film solar cells that are weakly absorbing over a broad wavelength range [11]. Diffraction gratings with period larger than the wavelength, mounted on thick (with respect to the wavelength) active regions, reach the same OPL as structures with random texturing. However, as the period and the cell thickness are down-scaled, wave optics effects become important and the simulation and design of such structures require rigorous electromagnetic approaches. Being the problem linear and the analyzed structures periodic, in this thesis we resorted to the rigorous

coupled-wave analysis (RCWA) method, whose fundamentals are described in the Appendix A.1.

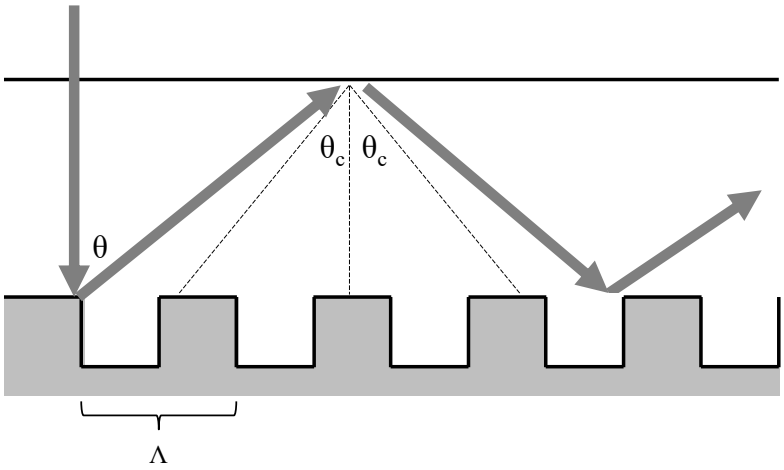

Figure 1.8: A back-side uni-periodic grating with period Λ diffracts normally incident light at a propagation angle θ that exceeds the escape cone of the active material, resulting in total internal reflection.

1.3 Quantum Dot Solar cells

1.3.1 Intermediate band QDSC

The Intermediate band solar cell (IBSC) is an attractive concept as it promises to overcome the SQ efficiency limit [7]. The operating principle is based on the sequential absorption of two sub-bandgap photons using an IB that is only optically coupled to the conduction and valence band, as sketched in Fig. 1.9. This allows extending the harvested solar spectrum up to the mid-Infrared (MIR) range, yielding large photocurrent and high voltage [35]. In fact, whereas the voltage of single-gap solar cells is limited by the lowest energy of the single photon they can absorb (E_g), in IBSCs a comparable voltage is generated by the absorption of two photons with sub-bandgap energies.

The IBSC therefore enables an extremely high efficiency limit, based on the Detailed Balance (DB) calculation performed in [7]. The calculated efficiency limit of an IBSC is compared to that of a single-gap solar cell in Fig. 1.10, where the IBSC reaches up to 63% efficiency under full concentration relative to an efficiency of 40% for a conventional single-gap solar cell under the same conditions. The optimized absorption energies of the IB system are approximately 1.2 eV (VB→IB), 0.7 eV (IB→CB), and 1.9 eV (VB→CB).

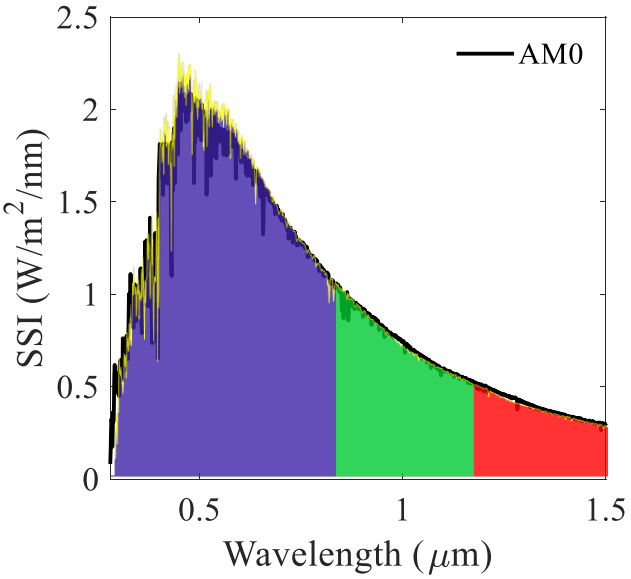

(a)

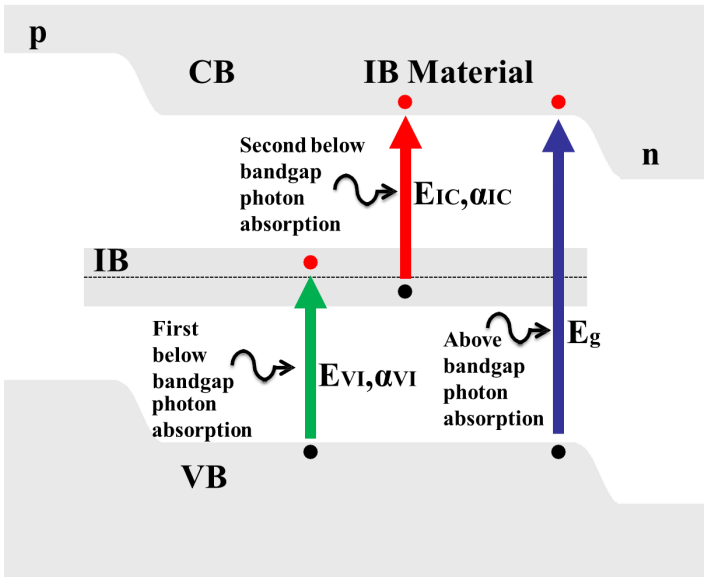

(b)

Figure 1.9: (a) The harvested spectral solar irradiance by an IBSC and (b) the schematic band diagram of an IBSC highlighting the sub-bandgap optical transitions between valence band and IB (VB→IB, green) and conduction band and IB (IB→CB, red), and the above gap (VB→CB, blue) optical transition.

Nanostructured materials such as QWs and QDs are widely studied for next generation photovoltaics as they provide multiple beneficial features. Their tunable

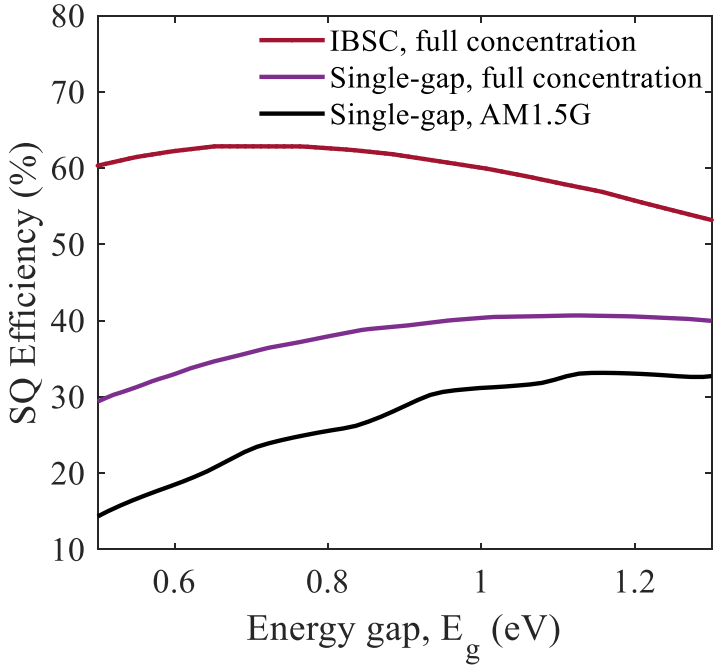

Figure 1.10: The SQ efficiency limit relative to the semiconductor bandgap energy (E_g) is shown for a single-gap solar cell at AM1.5G illumination, single-solar cell at full concentration, and an IBSC at full concentration.

optoelectronic characteristics provide a promising platform for single- and multi-junction solar cell optimization. QD layers embedded in a semiconductor barrier introduce sub-bandgap discrete energy levels, namely ground state (GS), excited state (ES), and a quasi 2-D wetting layer (WL) for electrons and holes due to the 3D carrier confinement. The energy states of a basic InAs/GaAs QDSC are shown in Fig. 1.11. The relative energy separation of these states depends on QD size, material, and lattice strain caused by the QD growth. Under illumination, charge carriers are photogenerated in the extended and bound states through interband and intraband optical absorption.

QDs are well suited as an IB material as they form three-dimensional potential wells that provide bound states fully isolated from the continuum bands owing to their zero-dimensional density of states [35]. In addition, they allow bandgap engineering through control of the growth process parameters, and in turn the QD size and density. Extensive research on III-V QD-IBSCs has allowed the experimental proof of the IBSC operating principles [36].

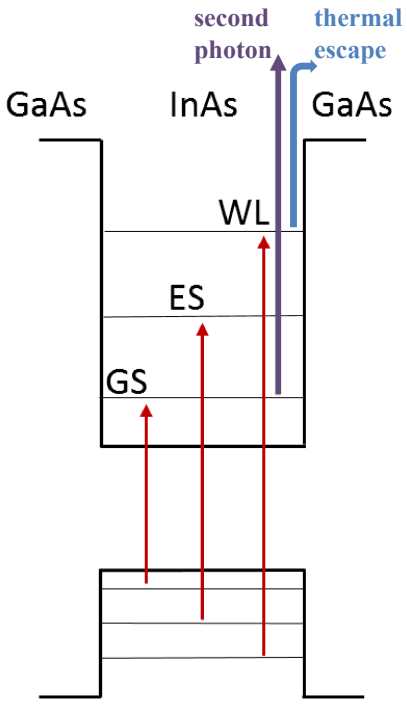

Figure 1.11: Employing QDs introduces 3D potential wells within the host semiconductor, which confine carriers in energy states within the forbidden energy band of the host semiconductor. The energy states of an InAs QD embedded within a GaAs active region consist of the GS, ES, and WL. The red arrows indicate the interband photoabsorption processes, while the intraband photoabsorption is represented by the GS transition.

1.3.2 Thermally limited QDSC

The demonstration of high-efficiency QD-IBSCs remains challenging due to fundamental limitations inherent to the QD themselves. First, the IB operation requires strong absorption coefficients (α_{VI}, α_{IC}) for the sub-bandgap optical transitions (i.e. the interband and intraband photon absorption) [36]. From the practical standpoint, their absorption is limited by the small optical cross-section of QDs and by the relatively low QD areal density and number of layers that can be used without compromising the solar cell crystal quality. Moreover, thermal and field-activated escape from the bound states forming the IB competes and hinders the second-photon absorption process to such an extent that the observation of two-photon absorption usually requires cryogenic temperatures, as highlighted in Fig. 1.11. Therefore, QDSCs generally operate in the thermally limited regime where interband carrier thermalization processes dominate over radiative recombination. At room temperature, photocarriers escape the QD confined states and

contribute to the photocurrent [37]. Accordingly, the spectral response directly indicates the absorption strength of the QDs. Even though incorporating QDs allows extending the spectral response, the strength of the response is relatively weak due to the inherent limitations of the QDs, such as the limited optical absorption cross section and low QD density that is typically obtained by self-assembled growth processes. Their conversion efficiency is further impacted by a drop in the open-circuit voltage. The best performing InAs/GaAs QDSC achieved a maximum efficiency of 18.7% [38], which is much lower than the record efficiency of 28.8% for a thin-film single-junction GaAs cell [39].

Nevertheless, thermally limited QDSCs are interesting to be studied due to their potential for enhanced radiation hardness, which is useful for space applications [40, 41]. The bandgap engineering of QDSCs can also be particularly useful for improved spectral tuning and optimization of MJSCs [42, 40]. In addition, thermal-escape limited QDSCs demonstrate an enhancement of the infrared spectral response. The additional optical transitions increase the photoabsorption of the cell, thereby widening the spectral response of the EQE in the QD absorption region (beyond $\lambda \approx$900 nm). The enhanced near-IR spectral response increases the obtainable photocurrent density at the cost of an open-circuit voltage penalty due to the embedding of the QD stack, which occurs due to defect mediated recombination induced by QD growth-related crystal strain. It is important to note that the quantification in terms of additional QD photocurrent from the interband (NIR) transitions is useful with respect only to this class of thermally-limited QDSCs that are not operating in the IB regime.

Figure 1.12 demonstrates $J-V$ and EQE simulations and measurements of practical InAs/GaAs QDSCs [43]. The $J-V$ in Fig. 1.12 (a) shows the notable V_{OC} penalty in the QDSCs relative to the reference bulk GaAs cell. The EQE spectrum is interesting as the addition of a 20-layer QD stack results in increased current density beyond the GaAs band edge as well as in the GaAs absorption range. For the sample with a 50-layer QD stack, the photocurrent in the QD range is enhanced while the GaAs range suffers due to reduced collection efficiency.

For perfect material growth, the simulated V_{OC} penalty is proportional to the number of stacked layers and the GS bandgap of the QDSC system. Figure 1.13 shows the scaling of V_{OC} with the number of QD layers and $E_{g,GS}$ for a thermally-limited QDSC operating at the radiative recombination limit, without accounting for material defects [43]. Accordingly, another design compromise is presented where the number of layers is proportional to the V_{OC} penalty but a small QD stack results in low absorption. Moreover, accounting for non-radiative recombination results in a further drop in V_{OC} due to material defects. Therefore, setting an upper limit on the QD density and number of QD layers that can be stacked is essential for improved crystal quality. Therefore, strain compensation techniques, QD material engineering [36], and photon management approaches are indispensable to overcome the limitations of QDSCs [13].

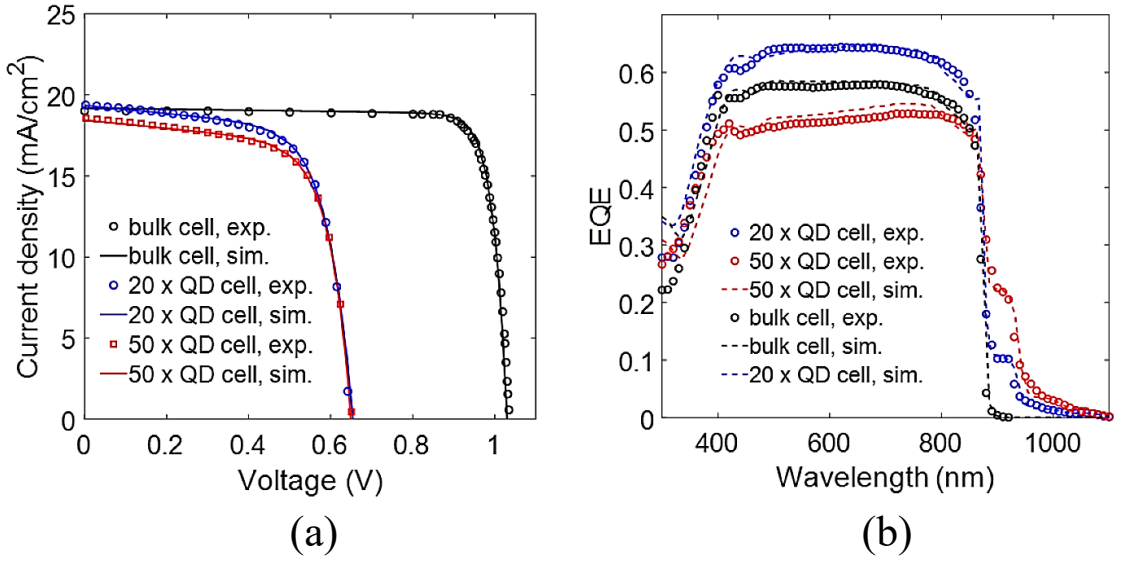

Figure 1.12: (a) $J-V$ and (b) EQE simulations and measurements of practical InAs/GaAs QDSCs relative to a bulk GaAs solar cell. The figure is adapted from [43].

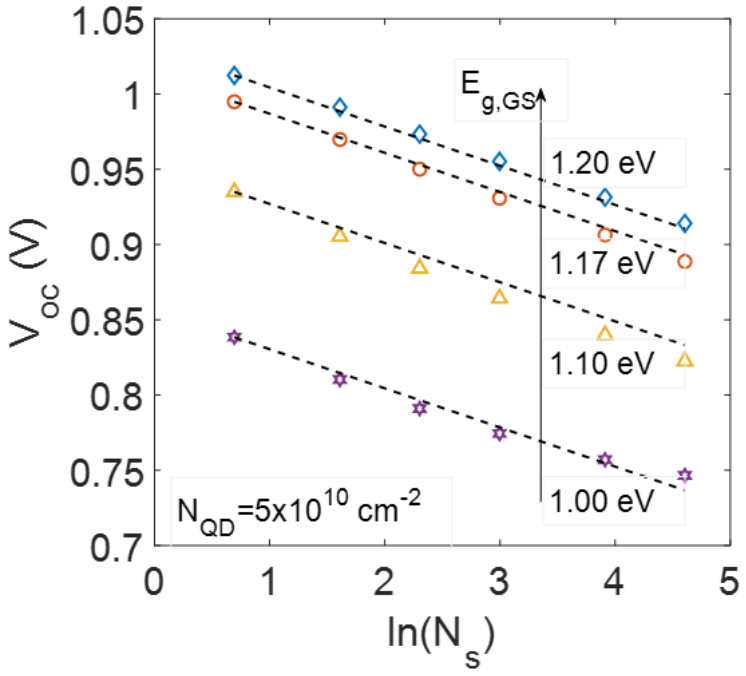

Figure 1.13: The scaling of the QDSC open-circuit voltage with the number of QD layers and the bandgap of the GS ($E_{g,GS}$) is shown for a fixed QD areal density of N_{QD}=$5\times10^{1}0\,cm^2$. The figure is adapted from [44].

1.3.3 Light trapping enhanced QDSC

Light trapping allows overcoming limitations faced by QDSCs and IBSCs, which generally suffer from weak QD interband and intraband photo-generation [45, 13]. It can be used to increase the effective OPL of the QD layers, thereby resulting in higher photogeneration and overall efficiency [10]. QD thin-film cells fabricated by epitaxial lift-off have been reported demonstrating a two-fold increase of QD near IR photocurrent through the integration of a planar reflector [43]. In addition, light trapping may relax the requirements in terms of crystal growth quality (resulting in a higher V_{OC}), while increasing the spectral photocurrent density that can be absorbed by the cell (resulting in an improved J_{SC}).

Regarding the impact to IBSCs, light trapping can be used to enhance the first and second photon transitions by increasing the absorbance at their corresponding wavelengths. The simultaneous enhancement of both transitions (interband and intraband) is essential to overcome one of the limitations to realize the IBSC concept. Light trapping also relaxes the competition between intraband absorption (corresponds to the second photon transition) and thermal escape of carriers. Physics-based simulations of InAs/GaAs QDs are used to compute the equivalent current density contribution from second photon absorption and thermal escape processes at varying solar concentration, for structures with a planar reflector (effective OPL=2) and a textured reflector (effective OPL=25), as shown in Fig. 1.14. The point at which second photon absorption generated current exceeds that of thermal escape indicates the theoretical solar concentration required for the IBSC to operate properly. At lower concentrations, thermal escape processes dominate and the second photon transition is not observed. However, it is shown through numerical simulations that the use of a textured reflector allows the second photon transition to be observed at a lower solar concentration, thereby relaxing the competition between both processes.

The calculated efficiency of a thermally-limited QDSC vs. photocurrent enhancement from light trapping is shown in Fig. 1.15 for different QD-layer stacks (N=20, 50, 100) to emphasize the potential efficiency enhancement due to light trapping [43]. Increasing the QD layer stack from 20 to 100 would require a significant effort from the practical standpoint (assuming perfect material growth) to obtain a small boost in efficiency, while a similar efficiency enhancement can be achieved using a simple light trapping strategy without incurring significant costs.

The generic light trapping structure utilizing back-side diffraction gratings for thin-film QD solar cells is presented in Fig. 1.16. The grating patterning process is carried out after wafer removal using techniques such as epitaxial lift-off [46]. The studied fabrication process generally consists of growing the AlInP/GaAs layers using molecular beam epitaxy and patterning of the periodic gratings on AlInP using nanoimprint lithography (NIL) [47]. Direct texturing of the semiconductor surface presents the concern of increased parasitic losses caused by the large

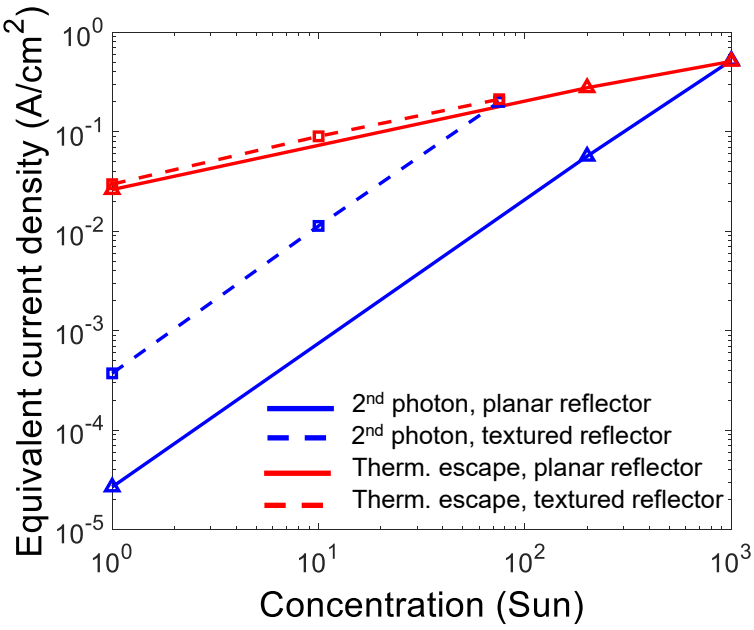

Figure 1.14: The computed equivalent current density contributions from second photon absorption and thermal escape processes are shown at varying solar concentration, for structures with a planar reflector (effective OPL=2) and a textured reflector (effective OPL=25).

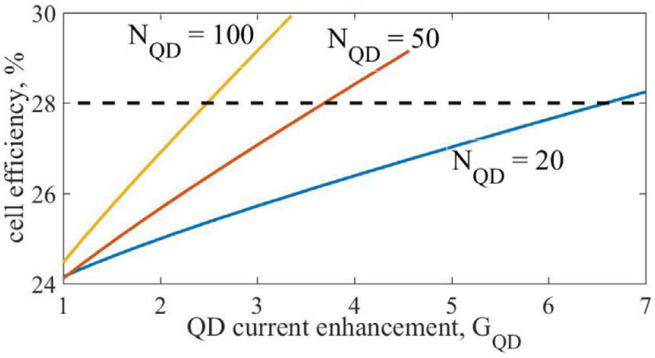

Figure 1.15: The cell efficiency vs. the QD current enhancement factor for QDSCs with varying number of QD layers, where the dotted line represents the efficiency of a single-gap GaAs cell.

semiconductor-metal interface. Hence, a dielectric layer is used to planarize the gratings and passivate the semiconductor surface in order to resolve the issue of electrical loss. The studied concepts are extendable to other photovoltaic configurations such as dilute nitride solar cells [48].

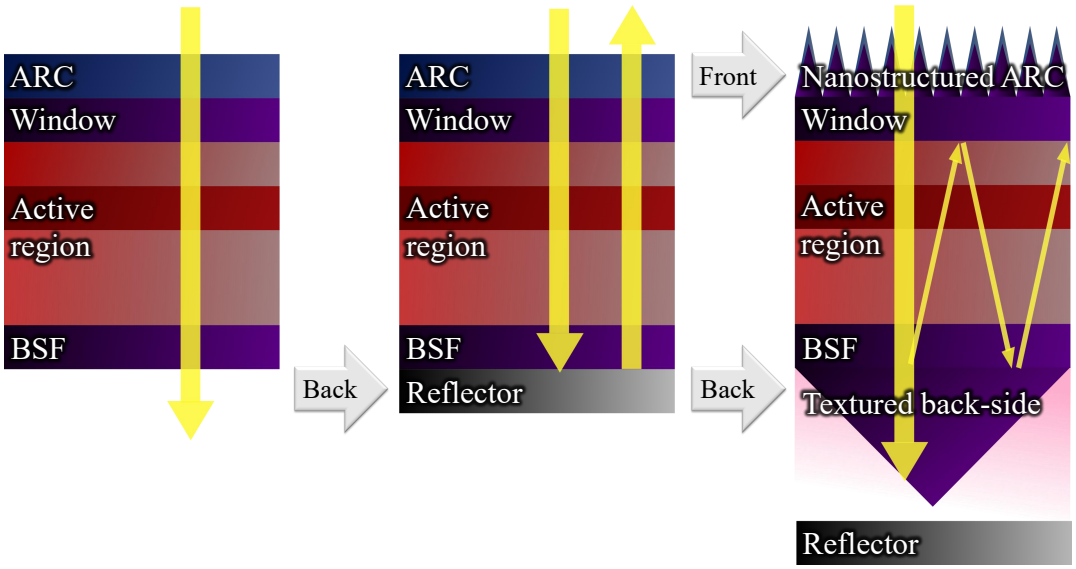

Figure 1.16: Basic InAs/GaAs QD solar cell structure implementing a wafer-based configuration (single-pass), double-pass configuration using a planar reflector, and full light trapping using double-side texturing.

1.4 Structure of this work

This work investigates photon management to enhance the performance of QDSCs. Several approaches are studied for the optical design and modelling of photonic structures to implement light trapping. The studies are validated using numerical and experimental methods. The research was conducted as part of the European H2020 project Thin-film Quantum Dot Solar Cells (TFQD), which aimed to investigate thin-film III-V quantum dot solar cells for space applications.

Following the introduction to the relevant topics, Chapter 2 focuses on the study of light trapping concepts using numerical methods. Photonic grating structures are employed to achieve light trapping for thermally-limited QDSCs. The optical design and optimization of the photonic structures is performed using numerical simulations. First, ubiquitous methods for reducing front surface reflectance are introduced, including planar and nano-structured anti-reflection coatings. Next, the QDSC structure under study is described and its simulation methodology is detailed. Numerical methods are utilized to perform the electromagnetic simulations of the studied solar cells, and a detailed description of the utilized methods can be found in Appendix A. Next, the optical modelling method of the QD layers is explained. The QD model is obtained from experimental methods as well as

the literature, and a study of QD material characterization using photoluminescence is described in Appendix B. After examining the models and methodology, full wave simulations are used to optimize periodic diffraction gratings on the cell back side with the purpose of maximizing the portion of light diffracted to high order modes, which contribute to an increased photocurrent by the QD layers. The grating optimization includes a study of different grating shapes and dimensions. The study then addresses combining both front side and back side texturing approaches for maximum enhancement of the effective optical path length. Finally, an analytical model is used to examine the impact due to the different light trapping configurations.

In Chapter 3, the validity of the theoretical concepts discussed in Chapter 2 is examined using experimental methods. Both numerical simulations and experimental characterizations of micro- and nano-structures are demonstrated for light trapping-enhanced cells. The optical characterization performed by the candidate as part of the TFQD project at the laboratories of Tampere University during his research exchange period is presented. First, planar structures are optically characterized and simulated to confirm the accuracy of the material models. Next, diffraction gratings imprinted on glass substrates are examined to characterize the impact of textured reflectors on light scattering without an absorber. The highest performing diffraction gratings are then imprinted on GaAs wafers and the samples are optically characterized in terms of reflectance and diffraction efficiency. The periodic structures on GaAs are also studied using full wave electromagnetic simulations. Finally, the results are used to predict the performance of a thin-film InAs/GaAs QDSC with textured reflectors.

A theoretical study is performed in Chapter 4 where periodic gratings are employed for ultra thin-film QDSCs operating in the IB regime. The aim of the study is to significantly increase the electromagnetic field intensity of a thin active region in a relatively narrow band, despite being achieved using gratings similar to those previously utilized for diffraction. The photonic gratings are employed to couple the incoming light to one or few modes, which requires the grating period to be comparable to the enhanced wavelength. Unlike Lambertian light trapping using diffraction gratings as investigated in previous Chapters, the guided-mode resonance (GMR) approach promises a significantly higher narrowband photoabsorption enhancement at target wavelengths for very thin cells. The cells studied in Chapters 2 and 3 demonstrate optically thick active regions and utilize gratings with large periods relative to the wavelength, thereby exciting several modes. The GMR gratings studied in Chapter 4 have periods comparable to the wavelength and ultra-thin active regions. Accordingly, only the GMR grating excited modes that resonate with the guided modes supported by the active region will be coupled into the cell, leading to narrowband OPL enhancement.

The GMR approach is particularly promising for the realization of the intermediate band solar cell concept. One of the main challenges of IBSCs is that they

require high interband and intraband photoabsorption at similar rates. First, the resonant gratings are used to enhance interband absorption of an example IBSC system. Next, the intraband absorption is targeted at the longer wavelength of the second photon. The grating dimensions are optimized using full wave three-dimensional simulations and angle selectivity is addressed. The parameters of the IBSC system are scanned by changing the absorption coefficient and the second photon energy to verify the applicability of the approach to different IBSC systems.

An efficient numerical modelling method is introduced in Chapter 5 that is applicable to solar cell structures incorporating periodic texturing, similar to those studied previously. The need for an efficient method arises due to the high computational resources demanded by electromagnetic simulations, in particular when including photonic gratings. In addition, realistic electrical simulations that account for QD dynamics are also computationally intensive. Accordingly, obtaining a self-consistent solution of QDSCs employing diffraction gratings requires a more computationally efficient approach that reduces the system complexity. The proposed method reduces the electromagnetic simulation to be one-dimensional, with the periodic grating modelled as a scattering matrix composed of the reflection coefficients for each diffracted mode. This requires a single step of extracting the scattering matrix of a grating from simulations performed using a commercial software. The efficient method renders the electromagnetic computations substantially faster, thereby enabling coupled and self-consistent electro-optical simulations. Finally, the optical method is verified against results produced the commercial software for an example QDSC.

The main conclusions of the research are summarized in Chapter 6. The dissertation concludes with a discussion regarding the impact of the proposed photon management techniques on the realization of QDSCs with efficiencies exceeding that of the SQ efficiency limit of single-junction solar cells. Despite the emphasis of this work on light trapping approaches applied to QDSCs, the photon management techniques are applicable to other solar cell configurations. In addition, other light trapping techniques are briefly introduced. Finally, an outlook is provided on the recent trends in the field of photon management.

Chapter 2

Light trapping for high-efficiency thin-film QDSCs

2.1 Introduction

Light-trapping can be used to significantly enhance the effective optical path length of thin-film solar cells or solar cells utilizing weakly absorbing materials. Due to the limitation of weak absorption within the QD stack, the use of light trapping approaches is necessary. Previous work on the feasibility of InAs/GaAs IB solar cells has shown the advantages of light trapping for absorption enhancement of the QDs [13]. The theoretical maximum optical path length enhancement, known as the Yablonovitch model [16], is around $4n^2$ for a given material with real refractive index n, which enables reduction of the number of QD layers by several orders of magnitude for practical implementation [13]. A recent implementation of light trapping for GaAs multiple quantum well solar cells has demonstrated an increase of the optical path length by five times, proving the potential for absorption enhancement [14]. Another promising work utilizing self-organized rear texturing for a 50-layer InGaAs/GaAs QDSC demonstrates enhanced photoabsorption in the QD layers by 2.4 times due to light trapping [50]. The aim of the study presented in this Chapter is to enhance interband absorption for thermally-limited QDSCs. The photocurrent generated by the QDs is a representative figure of merit for thermally-limited QDSCs where the aim of light trapping is to maximize the cell absorptivity in the whole wavelength range up to the QD bandgap. In view of QD-based IBSCs, the interband absorption must be combined with intraband absorption enhancement

---

The work presented in this Chapter is based on "Improved Light Trapping in Quantum Dot Solar Cells Using Double-sided Nanostructuring", F. Elsehrawy, T. Aho, T. Niemi, M. Guina, and F. Cappelluti [49].

in order to achieve proper operation of the cell in the IB regime.

Diffraction gratings and back mirrors have been studied extensively for light trapping in III-V QD and mullti-junction solar cells to enhance absorption and reduce the cell thickness, leading to improved radiation hardness [51, 52]. The scope of the work in this Chapter is bound to the enhancement of the effective optical path length of the active region by utilizing symmetric, periodic, square-base pyramid diffraction gratings on the back-side, while other techniques could also provide high enhancement. Front-side pyramidal and tetrahedral gratings with features greater than the wavelength promise high coupling of light to the absorbing material, while minimizing the probability of escape from the front surface, thereby providing strong light trapping characteristics [53]. Other work using asymmetrical pyramid-shaped gratings has demonstrated interesting results, with improved performance relative to symmetrical ones [54]. In addition, pyramid gratings with different base shapes (with n base points) exhibit interesting effects that warrant further research [55, 53]. A noteworthy result reported in [56] is the achievement of an ultra-thin GaAs solar cell with an active region thickness of 205 nm that demonstrated 19.9% efficiency by utilizing a nanostructured backside reflector. Furthermore, the work finds that achieving up 25% efficiency is feasible as a short-term goal using the same light trapping structure.

Randomly textured surfaces have also been studied for light trapping in [57, 50], which would constitute a simple etching process that can be applied to many solar cell processing technologies. The randomly textured surfaces would ideally result in Lambertian scattering, which is particularly useful when addressing incident angle insensitivity. Random scattering surfaces can also be combined with diffraction gratings to create hybrid surfaces that approach the Lambertian limit [22].

In this Chapter, cells employing intermediate band materials adapted from the literature are studied [43]. These cells demonstrate promising performance and can be realized using epitaxial lift-off techniques. Initially, light trapping methods are investigated for thin-film InAs/GaAs QD solar cells by utilizing back-side diffraction gratings and planar metal reflectors. A systematic grating design optimization methodology is followed in order to obtain the maximum absorption in the QD stack. The back gratings are designed with the aim of exciting high order diffraction modes, enabling total internal reflection at the surface of the cell [11, 12, 58]. This effectively leads to an enhanced effective optical path length and therefore improved photocurrent. Next, the impact of double-sided gratings on light trapping is examined using several mechanisms. Nanostructured gratings were fabricated on the front or back-side for antireflection or diffraction, respectively, where the optimization process for the different regimes is decoupled [59, 60]. Light trapping effects are simulated in thin-film quantum dot solar cells with integrated double-sided gratings, demonstrating a significant enhancement of the achievable QD photocurrent.

First, the QDSC structures and their optical modelling methods are introduced. Next, the optimization methodology of the double-side gratings and the simulation results are presented. Finally, an analysis of the factors contributing to the QD photocurrent enhancement is performed. The simulation results are interpreted by evaluating the light path enhancement factor [61] and the light trapping enhancement [62], aiming to provide deeper insight into the double-side grating solar cell operation.

2.2 Anti-reflection coatings

Due to the large index mismatch at the incident light interface between the front surface of the solar cell and air, it is necessary to design an anti-reflection coating (ARC) in order to minimize the front surface reflection. Materials for ARCs are generally selected using the optimum refractive index at the desired wavelength, as described by $n_{ARC} = \sqrt{n_{air} * n_{window}}$, with the optimum layer thickness (t_{opt}) for a desired wavelength found to be an odd multiple of $\lambda/4$ [63]. The obtainment of a wider anti-reflection spectrum is also possible using a multi-layered ARC. Extending the principle for a double layer ARC requires optimum refractive indexes n_1 and n_2 to follow $n_1 n_2 = n_{air} n_{window}$ for a wide band reflectance reduction [64].

The conventional ARC for solar cells consists of single- or double-layer dielectric coating using, for example, SiN_x, ZnS/MgF_2 or SiO_2/TiO_2. The challenge with double-layer dielectric coating is achieving low (<5 %) reflectance over the entire GaAs and QD wavelength range (400 – 1200 nm). An extreme generalization of the multi-layered ARC is the use of pyramidal bi-periodic gratings, where the graded variation of refractive index from the tip to the base of the pyramid mimics the presence of multiple layers, enabling broadband anti-reflection operation.

Front-side bi-periodic gratings can be used to reduce the reflection from the front surface of the solar cell or for trapping the light inside the active region of the cell. For front-side gratings with periods that are much smaller than the wavelength, the 0^{th} diffraction order is the only order propagating from air into the substrate. This does not allow light trapping since the incident light is not diffracted to higher order modes. However, such gratings allow significant reduction of the front surface reflection by matching the in-plane components of the wave vectors between the grating modes and diffraction modes in air and the substrate [11]. Therefore, a broadband, efficient anti-reflection coating could be implemented using gratings with features much smaller than that of the wavelength of incident light.

While the nanostructured shape has a minor impact on the antireflection properties, the aspect ratio is essential to minimize the reflection. The longer height with a small period relative to the target wavelength allows a smooth grading of the refractive index from the air to the window layer, thereby reducing the index mismatch. Initial optimizations of a bi-periodic pyramidal AlInP nanostructure

demonstrate that a minimum height of around 350 nm with a period below 400 nm is necessary to maintain a reflectance below 5 %. However, further increases of the height result in a detrimental parasitic absorption in the AlInP due to an increased effective optical thickness. The structures with AlInP pyramids on top of GaAs are 3D simulated using the rigorous coupled wave analysis (RCWA) method and the results are presented in Fig. 2.1.

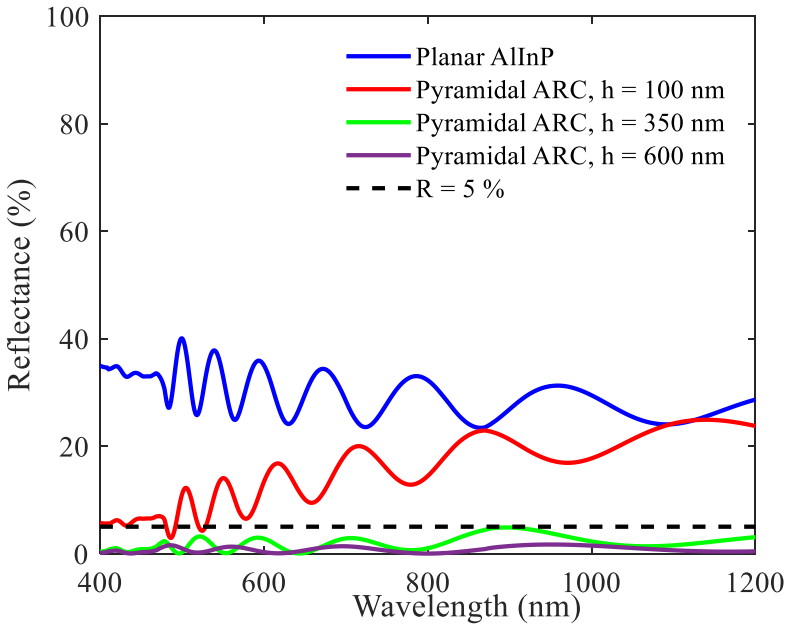

Figure 2.1: Simulation of 180 nm period pyramids on AlInP on top of GaAs substrate. The height of the pyramids is compared to the reflectance.

2.3 QDSC structures

The basic structure and detailed layer thicknesses of the thin-film QDSC used for the back-side grating optimization is found in Table 2.1. The reference planar ARC is composed of a single SiN_x layer at the interface with air, and a second investigated planar configuration includes a standard two-layer SiO_2 and TiO_2 ARC. The planar ARC layer thicknesses were selected based on simulations using the transfer matrix method (TMM) [65], where the reflected power density under extra-terrestrial solar spectrum AM0 illumination is minimized at $\lambda = 0.4$ μm – 1.2 μm for the unpatterned structure without the back reflecting mirror. An AlInP window layer is then used to reduce surface recombination at the interface of the active layer. The absorbing layers (photoactive region) consist of GaAs embedded

with a stack of 20 InAs/GaAs QD layers, with each layer composed of 4 nm QD followed by 16 nm GaAs spacers. Next, an AlInP layer is added as the back surface field layer and is the material on which the gratings are fabricated for two reasons: first, the simplified fabrication process of etching on the back surface field layer and second, the high index of the AlInP material (and therefore larger refractive index contrast) which leads to improved diffraction performance [12, 62]. A planarizing polymer layer ($n = 1.5$) is added as an interface between the AlInP and the Ag mirror to reduce parasitic losses due to conformal rear reflectors [11]. The structure is terminated with a planar silver (Ag) mirror to maximize the back-side reflectivity.

Table 2.1: Thin-film cell structure: materials and thicknesses (starting with layer at which light is incident)

Layer	Thickness (nm)
SiN_x ARC	80
AlInP window	40
GaAs emitter	160
20-Layer InAs/GaAs QD Stack	140
GaAs base	1700
AlInP back surface field (BSF)	40

The light trapping-enhanced InAs/GaAs QD thin-film solar cells under analysis are shown in Fig. 2.2. Five configurations are analyzed and compared in terms of photocurrent enhancement: 1) unpatterned cell with a planar ARC and a planar back-side mirror, 2) cell with a nanostructured ARC and a planar back-side mirror, 3) cell with a planar ARC and a bi-periodic back-side pyramid grating with Ag mirror, 4) cell with a nanostructured ARC and a bi-periodic back-side pyramid grating with Ag mirror, and 5) cell with a multilayer nanostructured ARC and a bi-periodic back-side pyramid grating with Ag mirror. The unpatterned cell without a reflecting mirror is equivalent to a reference wafer configuration in which the sample does not go through further processing.

The back-side grating is optimized to enhance diffraction in the QD wavelength range of 895 nm – 1200 nm, where light trapping is necessary. The final nanostructured front-side ARC is optimized to have low reflectivity over the entire GaAs and QD spectrum, in the wavelength range of 400 nm – 1200 nm.

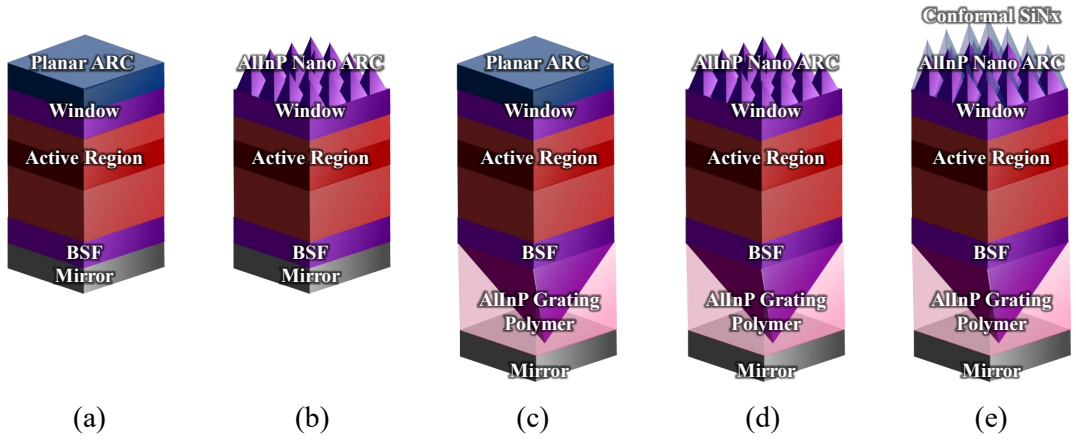

Figure 2.2: (a) Reference planar structure. (b) Cell with nanostructured ARC and planar mirror. (c) Cell with planar ARC and back-side grating. (d) Cell with nanostructured ARC and back-side grating. (e) Cell with double-layer nanostructured ARC and back-side grating.

2.4 Modelling approach

2.4.1 Materials optical properties

Optical properties of the materials, including a realistic model of Ag, are adapted either from the literature [66] or from experimental characterization [47]. Several Ag sources in the literature provide inconsistent optical data due to discrepancies in the measurement conditions [67]. However, the Ag model presented in [66] is found to be the less optimistic yet most ubiquitous source, and therefore provides a low estimate of enhancement due to light trapping. The optical models (real and imaginary refractive indexes) of the materials used in the simulations are found in Fig. 2.3.

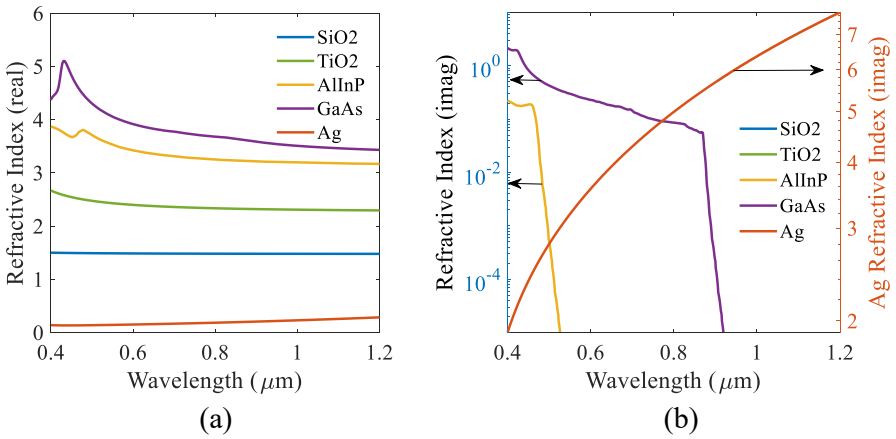

Figure 2.3: Optical models of the materials (complex refractive indexes) are shown. The models are obtained from the literature, while the SiO_2 and TiO_2 models are adjusted using ellipsometry measurements. The SiN_x, OrmoComp, and SU-8 models are assumed to be a constant over the spectrum and do not account for any absorption.

The model for the QD layers (described as effective medium) is derived from experimental data [43]. The optical absorption coefficient has been derived from photoluminescence and external quantum efficiency measurements. It may be noted that:

- The optical absorption extracted from these measurements represents the effective absorption of the QD layer intended as a composite material made of the QD nanostructures and bulk GaAs (and accounting for the volume fraction of QDs within the host semiconductor).
- The QD nanostructures add further electronic states which are separated from the bulk states in energy or wavelength. Thus, the absorption spectrum associated to the QD states consists of discrete lines (or more realistically resonances with finite width) appearing at wavelengths where the host material is transparent (zero absorption).

In view of the above points, it is appropriate to represent the overall absorption coefficient as the superposition of the bulk absorption coefficient (α_{GaAs}) and the absorption coefficient induced by the presence of the QDs ($\alpha_{QD,eff}$):

$$\alpha_{eff} = \alpha_{QD,eff} + \alpha_{GaAs} \tag{2.1}$$

The effective QD coefficient $\alpha_{QD,eff}$ should be differentiated from the absorption coefficient of the single QD [cm^{-1}], which is a less relevant physical quantity than the optical cross-section [cm^2] of the QDs [68]. The coefficient $\alpha_{QD,eff}$ then inherently

accounts for the in-plane density and size of the QDs, and the interdot vertical spacing which implies the QD volume filling factor.

From the definition of α_{eff} and applying the Kramers-Kronig relations, the refractive index of the equivalent medium can be derived. It can then be shown that $n_{eff} = n_{QD,eff} + n_{GaAs}$, with $n_{QD,eff}$ and n_{GaAs} derived from $\alpha_{QD,eff}$, α_{GaAs}, respectively, through Kramers-Kronig. The derived spectral dependence of the refractive index of the QD stack is shown in Fig. 2.4, where the bandgap of the GS, ES, and WL states is set to 1.14, 1.21, and 1.39 eV, respectively. The optical absorption in the QD layers associated to each interband transition is modelled by a Gaussian function with absorption peaks on the order of 10^3 cm^{-1} for the GS and ES states, and 10^4 cm^{-1} for the WL state. The QD optical model used in this study was calibrated based on epxerimental EQE and photoluminescence measurements of QDSCs fabricated within the TFQD project [43]. These cells had QD layers with an areal density of around 6×10^{10} cm^{-2}, with QD height of about 4 nm. Appendix B reports the results of the PL characterization of some of the samples produced in the project.

2.4.2 Simulation method

The structures in this study are simulated using the Synopsys RSoft tool DiffractMOD [69], by implementing the rigorous coupled wave analysis method, a well-suited method for periodic diffractive structures [70, 71]. The methods used for the electromagnetic simulations of the studied cells are reviewed in Appendix A.1. The simulations assume normal incidence for the extra-terrestrial solar spectrum, AM0. The optical absorbance in the photoactive region is given by Equation (2.2), which allows differentiating between the useful absorption increase in the active region and the optical losses in the electrically passive layers, such as the ARC, AlInP grating, and lossy Ag mirror. The parameters are computed region by region at each wavelength using the spatial distribution of the electromagnetic field, where V is the volume consisting of the GaAs and QD layers, E is the spatially dependent normalized electric field of the volume, and α is the absorption coefficient specific to the discretized layer.

$$A(\lambda) = \int_V n\alpha|E|^2 \,\mathrm{d}V \tag{2.2}$$

Comparison between different photonic configurations and the optimization of the grating parameters is carried out with reference to the photogenerated short-circuit current density, J_{SC} [mA/cm^2] obtained using Equation (1.4). Light trapping primarily enhances absorption on the longer wavelengths, for which near-ideal carrier collection efficiency can be obtained by careful electrical design [72, 73, 68]. The J_{SC} estimation is based on optical simulations and does not consider electrical transport losses. An example demonstrating the effectiveness of this approach is

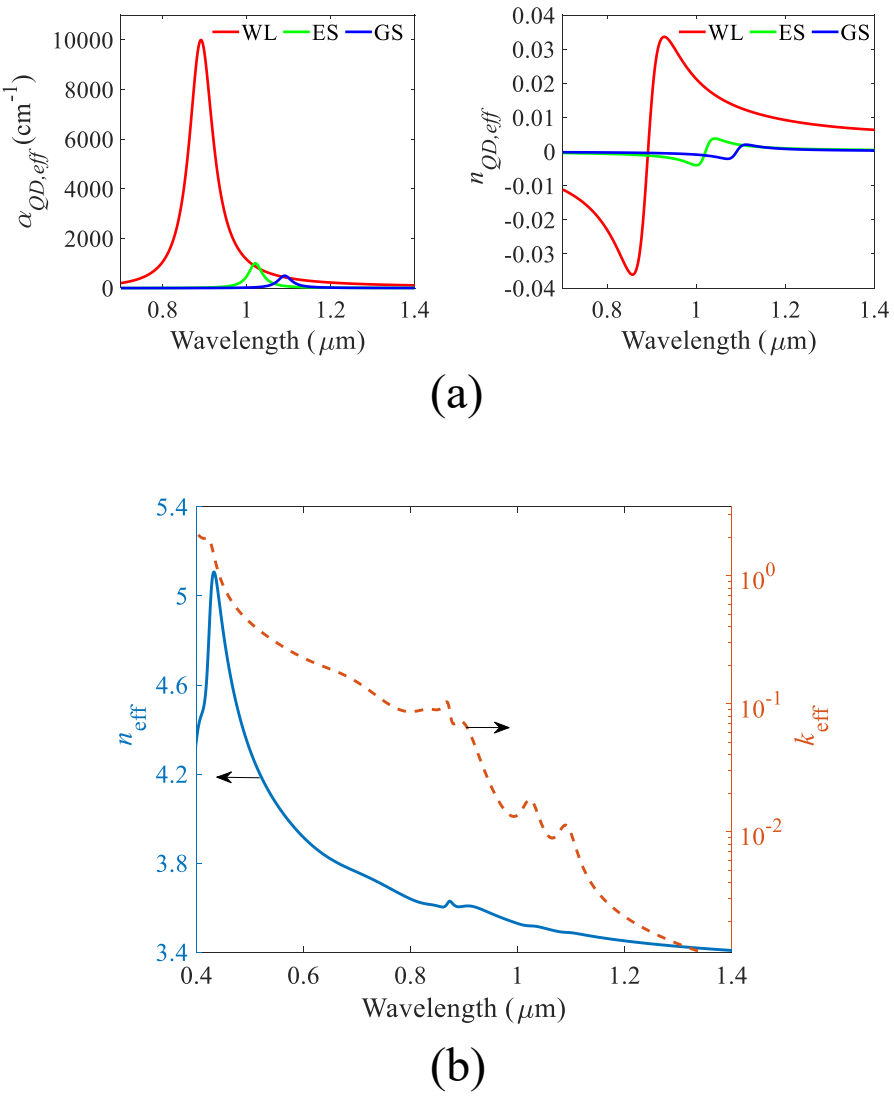

Figure 2.4: The optical model of the QD layer is described where (a) the absorption coefficients and (b) the combined complex refractive index are displayed.

performed using a thin-film GaAs solar cell with a 2μm active region incorporating a 10-layer InAs/GaAs QD layer stack with a planar ARC and a planar backside reflector. The example structure is modelled optically and electrically using the methodology described in Chapter 5. The absorbance, EQE, and IQE spectra of such QDSC are shown in Fig. 2.5, where the IQE approaches 1 at the longer wavelengths. Accordingly, this allows us to consider a unit collection efficiency in the study, and one can then rely on absorbance simulations to provide a meaningful prediction of the expected short circuit current in the QD region.

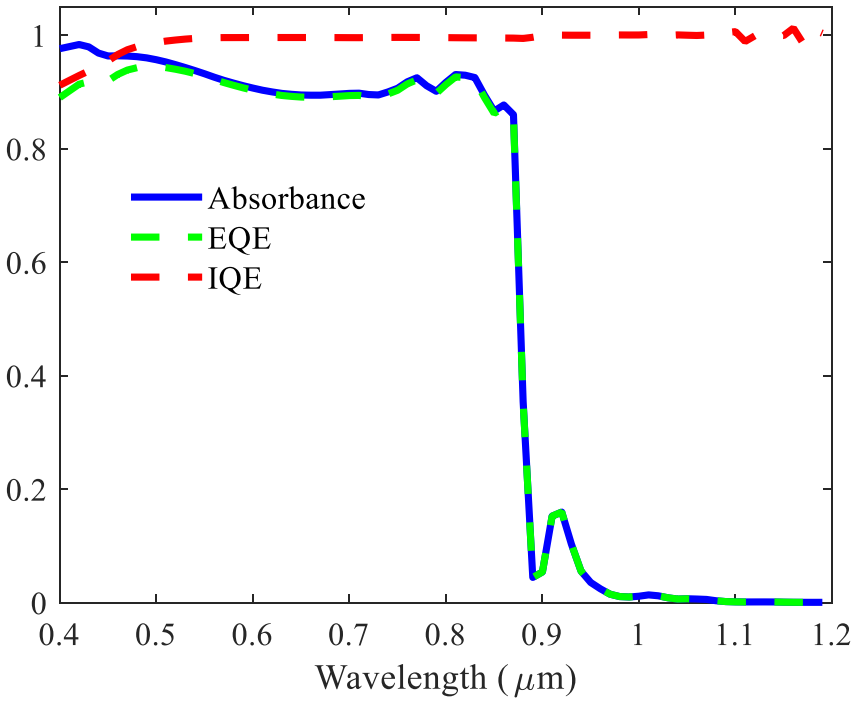

Figure 2.5: The absorbance, external quantum efficiency, and internal quantum efficiency spectra of a thin-film solar cell incorporating a 10-layer InAs/GaAs QD layer stack with a planar backside reflector. A high IQE is observed at longer wavelengths that approaches 1, implying ideal carrier collection efficiency.

A convergence study was performed for the cell structures with a back-side grating prior to the simulations; 10 harmonics (i.e. Fourier order = 21) was found to be sufficient to reach a reasonable accuracy without added computational cost, and the results of the convergence study displayed in Fig. 2.6.

For the simulation of the InAs/GaAs QD stack, two approaches were investigated in order to obtain a computationally efficient model with high accuracy:

- Using discrete stratification of 4 nm-thick QD layers (i.e. N layers of QD with 4nm thickness) separated by interdot GaAs layers, as in the QD real stack
- Using an equivalent QD layer ($4N$ nm total thickness) treated as homogenous medium, and taking into account the GaAs interdot layers by thickening the surrounding GaAs layers in order to conserve the total thickness of the photo-active region

The accuracy of the equivalent QD model compared to the stratified layers was studied based on simulations of planar reference structures, with the absorbance and reflectance spectra displayed in Fig. 2.7. The qualitative analysis shows high

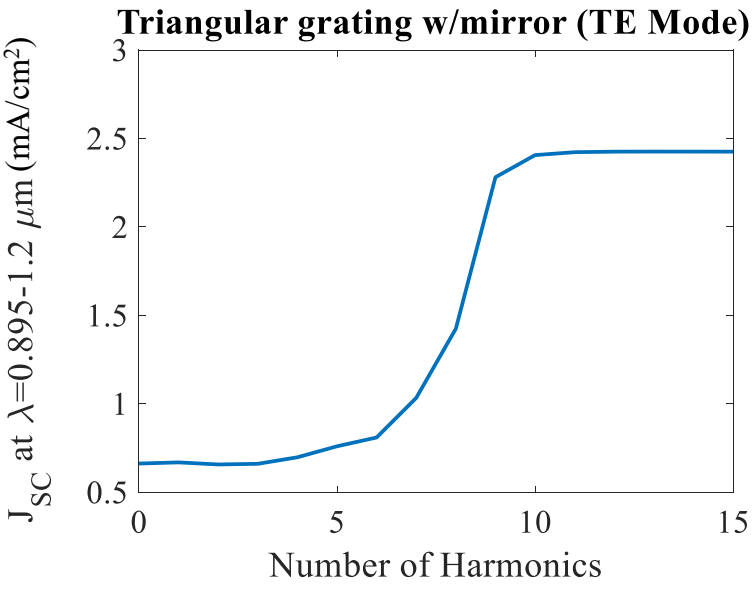

Figure 2.6: The convergence study for the minimum number of Fourier orders necessary to obtain an accurate simulation output is shown. The number of harmonics was increased until convergence is observed for the computed short-circuit current density J_{SC} (mA/cm^2) in the QD region (λ=0.895−1.2μm), which occurs at around 10 harmonics.

agreement between both QD models. The study was repeated for structures with a uni-periodic back grating and similar trends were observed. The simulation requirements for the multilayer QD model are more demanding as the discretization step in the z-direction needs to be as low as or lower than the single layer thickness of 4nm.

It can be concluded that the equivalent layer QD model provides a useful approximation. It relieves the necessity to simulate the cell at a high resolution, where a refractive index spatial resolution of 4 nm or lower is necessary to obtain convergence for the multilayer QD model. However, using the equivalent layer model with a step size of 10 nm is sufficient to obtain sufficient agreement between the models, which was used for the following simulations.

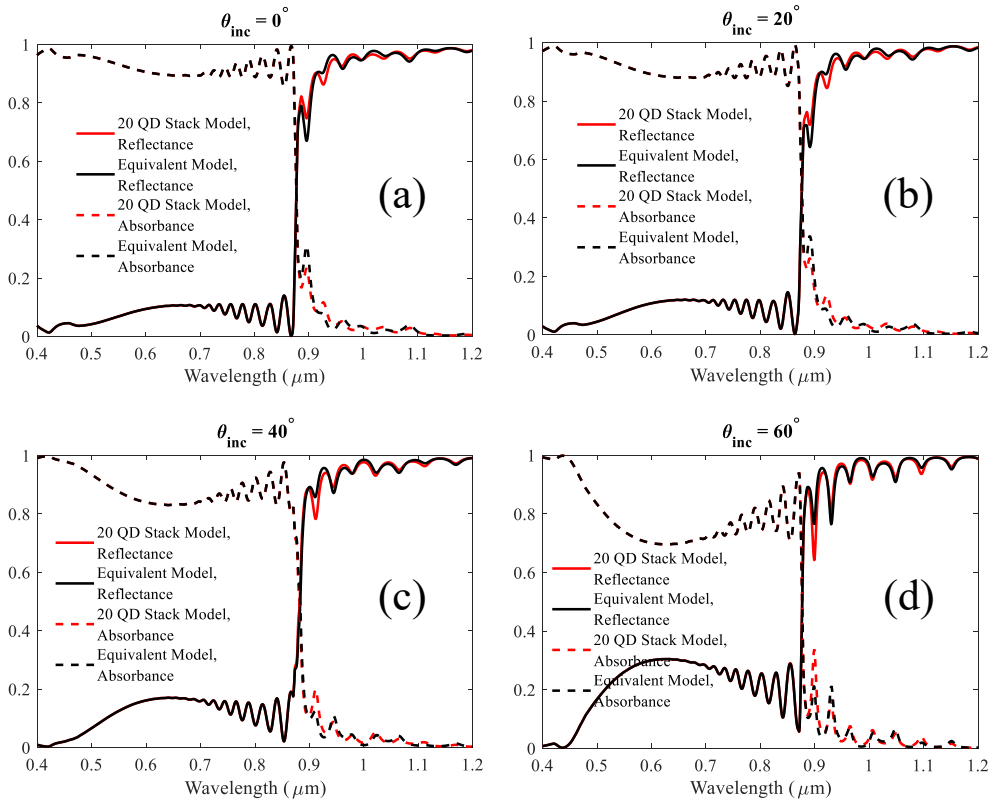

Figure 2.7: Total absorbance (dashed) and reflectance (solid) spectra simulated at the angles of incidence (a) $\theta_{inc} = 0°$, (b) $\theta_{inc} = 20°$, (c) $\theta_{inc} = 40°$, and (d) $\theta_{inc} = 60°$. The simulation is performed using the TMM method for QDSC structures implementing the Equivalent (black) and 20-layer stratified (red) QD models.

2.5 Back-side grating geometry optimization

Back-side diffraction gratings can be utilized to implement light trapping through two mechanisms. First, the incident light could be coupled into the guided modes of the active region for an ultrathin structure that supports few waveguide modes [74]. Secondly, the light could be coupled into higher order diffraction modes which propagate within an active region that supports a multitude of photonic modes, as is intended in this study [60]. A common strategy is using back-side gratings with a period of multiples of the enhanced wavelength for maximum light scattering [34, 54].

The grating design process aims primarily to couple incoming light into high order diffraction modes. The diffracted light propagates at angles higher than the cell escape cone (which corresponds to $\theta_c \approx 16°$ for the GaAs refractive index of 3.6 at longer wavelengths). This allows multiple total internal reflections in

the photoactive region, thereby enhancing the effective optical path length. In the planar configuration, the high reflectivity mirror enables the doubling of the optical path length in the weak absorption regime.

2.5.1 Aspect ratio design

The back grating shapes are designed to be triangular for the uni-periodic (1D) gratings and pyramidal for the bi-periodic (2D) gratings. Higher efficiency enhancement is expected for pyramidal gratings as opposed to more rounded geometries originating from the fabrication process [75]. The active region photogenerated current is examined as a function of the grating period (Λ) and height (h). From the results exhibited in Fig. 2.8, the relevant parameter for light trapping optimization is found to be the aspect ratio, defined as the ratio of height h to period Λ $AR = h/\Lambda$. For any grating period in the considered range (1 μm – 3.4 μm), the maximum photocurrent is achieved for the aspect ratios in the range between 0.32 – 0.38. Additionally, the optimization was repeated for structures with various GaAs emitter thicknesses (1.0 μm, 1.6 μm, and 2.2 μm) and the ideal aspect ratio was consistently found to be in the same range. This proves that, for periods sufficiently large to support an adequate number of diffracted orders, the most relevant parameter for light trapping optimization is the grating aspect ratio.

Figure 2.8b also reports the mean diffraction efficiency computed for angles greater than θ_c. The behavior is quite similar to that of Fig. 2.8a, strengthening the validity of the interpretation of the back-side grating operation. As a result of this parametric investigation, a reasonable choice for the grating period and height, accounting for possible fabrication tolerances, is $\Lambda = 2.4\mu$m and $h = 0.9\,\mu$m.

2.5.2 Impact of the grating shape

Analysis of multiple grating shapes has been previously studied in other works such as [11], where uni-periodic lamellar, bi-periodic pillar, and asymmetric blazed gratings are among the investigated shapes. The grating period is found to have a higher impact on diffraction efficiency, despite the different effects observed by each grating shape [58]. To further investigate alternative grating shapes for the proposed cell structure, a parameter adapted from [75] is defined, the order of taper (OT), which varies the grating shape according to:

$$r = R\left(\frac{z}{h}\right)^{OT} \tag{2.3}$$

where r is the radius of the grating in the XY-plane, h is the grating height, and R is the grating bottom radius. The formulation allows the attainment of multiple shapes as shown in Fig. 2.9 by varying the OT from 0.1 to 10.

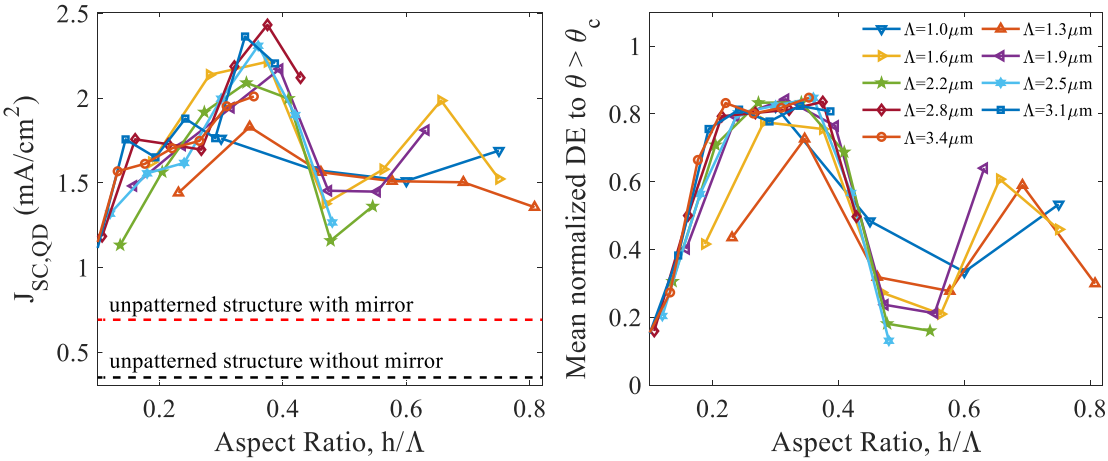

Figure 2.8: Aspect ratio optimization relative to (a) the photocurrent and (b) the mean normalized power diffracted towards higher order modes ($\theta > \theta_c$), in the QD absorption wavelength range $(0.895 - 1.2)\,\mu$m for different values of the grating period.

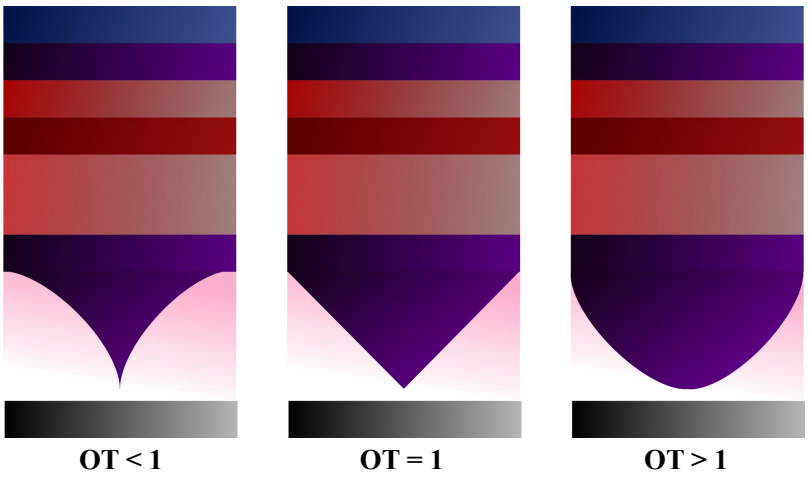

Figure 2.9: (a) Cell structures with uni-periodic gratings for varying grating Order of Taper (OT).

The short-circuit current density exhibits a strong dependence on the grating shape, as shown in Fig. 2.10a, where the J_{SC} enhancement is shown for different values of OT in the QD range ($\lambda_i = 0.895$ μm to $\lambda_f = 1.2$ μm). The maximum photocurrent enhancement occurs at $OT = 1$ for a uni-periodic triangular grating,

with a similar trend expected for the bi-periodic pyramidal grating. In addition, the impact of the OT on the diffractive properties of the grating is examined. The uni-periodic triangular grating was analyzed separately without the active region, and its wavelength dependent diffraction angle and normalized diffraction efficiency are demonstrated in Fig. 2.11 for three values of OT. The highest amount of light coupling to modes with angles higher than 16°, corresponding to the GaAs escape cone, occurs at $OT = 1$. The photocurrent density enhancement due to back-side gratings in solar cells could then be correlated to the higher order diffraction efficiency, as shown in Fig. 2.10b where the diffracted power attainable by only the grating follows the same trend as the J_{SC} of the complete solar cell. This study also provides insight towards the impact of fabrication imperfections on the achievable photocurrent enhancement, where a slightly flattened grating would still result in a high improvement.

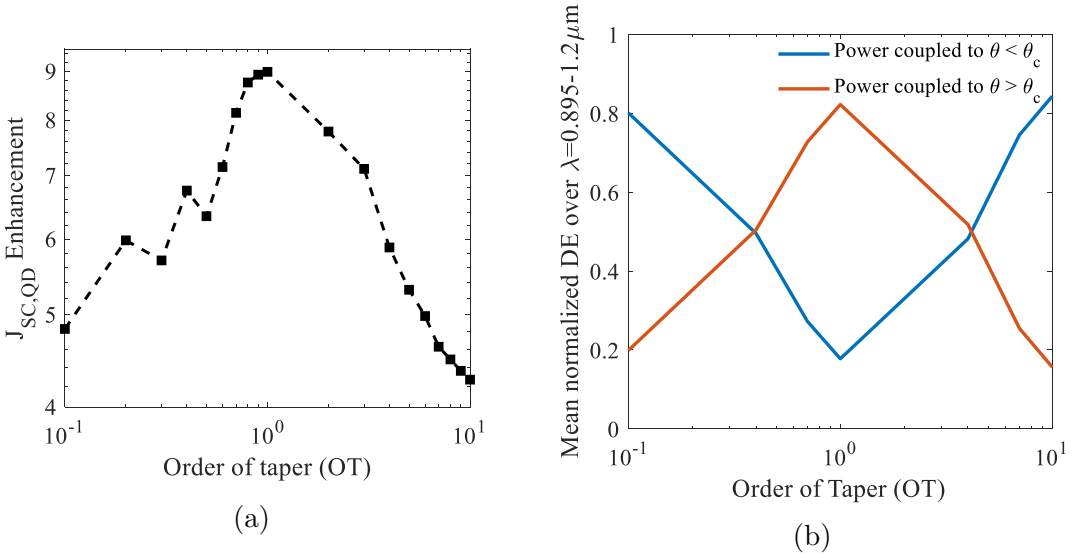

Figure 2.10: (a) Short circuit current density (J_{SC}) enhancement vs. order of taper (OT) for uni-periodic gratings. (b) The mean normalized power diffracted to angles above or below 16° at $\lambda = 0.895 - 1.2\mu$m relative to the OT for uni-periodic gratings.

This leads to an interesting observation: by examining Fig. 2.9, one could note that, for an increasing or decreasing OT, the profiles tend to be flattened, making the grating more similar to a slab. It is possible that less power is coupled to the diverging orders. This theory is strengthened by the results of the RCWA simulations reported in Fig. 2.11, which clearly shows how, in the triangular grating profile, significantly more power is coupled to diverging orders. The observed trends are exhibited for the uni-periodic case and were also observed in simulations of bi-periodic gratings. This confirms the previous assumption of the triangular grating as the optimal shape for enhanced light trapping.

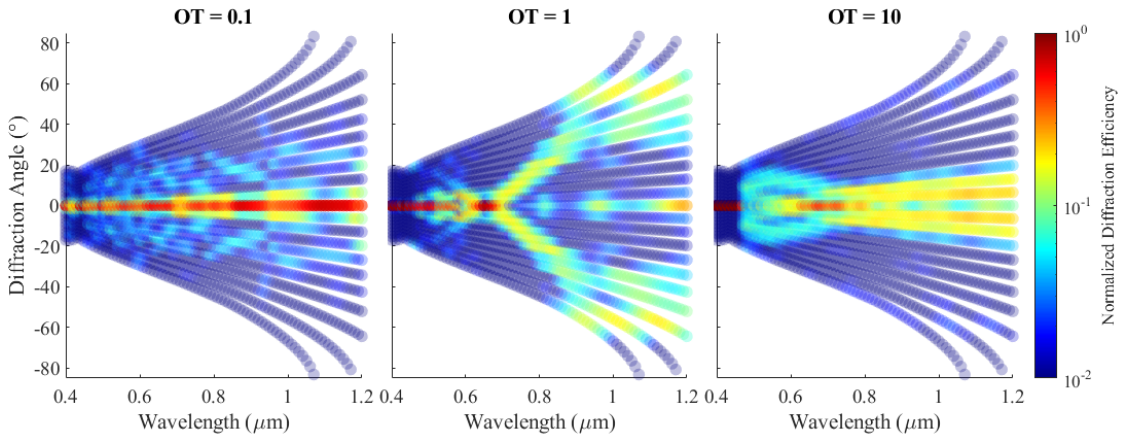

Figure 2.11: The wavelength dependent diffraction angle and normalized diffraction efficiency for OT=0.1 (left), OT=1 (center), and OT=10 (right).

2.5.3 Mitigation of plasmonic losses

The plasmonic interaction of the metal mirror must be carefully taken into account during the design process. The integration of textured metallic reflectors on the backside results in losses caused by the plasmonic modes propagating in the metal [11]. In addition, if the grating corners are too close to the metal, the scattered field could couple to the surface plasmonic modes propagating at the metal interface, resulting in additional losses in the short-circuit current density. By observing the spatial photon absorption (not shown), it becomes clear that the metallic losses inhibit the QD absorption. Therefore, the planarization the backside grating with a polymer layer is necessary to mitigate the metallic losses. The losses dominate in TM incidence but are also present for TE incidence, due to the excitation of TM modes by the grating relative to the metal surface.

Another degree of freedom in the design is the width of the SU-8 layer surronding the grating. Regarding the thickness of the planarizing polymer layer, a sweep to optimize the layer thickness was done in order to identify the minimum threshold for sufficient reduction in Ag absorption. The layer thickness optimization with regards to the QD photocurrent is shown in Fig. 2.12. The figure shows the QD short-circuit current density versus the polymer layer thickness measured from the triangle base, where a thickness of 0 corresponds to the direct deposition of Ag on the AlInP grating. For the optimized triangular grating with 1.05 μm height, a polymer thickness of 1.2 μm (corresponding to 150 nm beyond the grating triangular grating edge) was selected to reduce the losses while maintaining the light trapping characteristics of the diffraction grating.

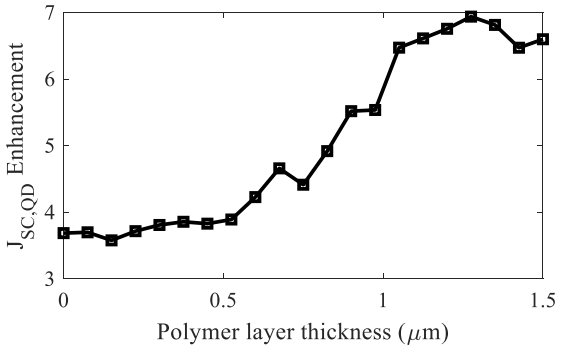

Figure 2.12: Short circuit current density (J_{SC}) enhancement vs. planarizing polymer layer total thickness, for a triangular grating structure with $h = 1.05$ μm.

2.5.4 Optimization results

The absorbance spectra of the structures with back-side gratings and planar ARCs is shown in Fig. 2.13, where a notable enhancement is demonstrated around the GaAs band-edge and in the QD wavelength range. The corresponding J_{SC} under AM0 illumination are obtained by integrating over the wavelength range of $\lambda_i = 0.895$ μm to $\lambda_f = 1.2$ μm (QD absorption region) using Equation (1.4). The optimized back-side pyramidal grating provides a QD region photocurrent enhancement of over 13 times with respect to a conventional unpatterned wafer configuration cell and a similar enhancement factor is obtained for terrestrial solar spectrum AM1.5G illumination (not shown).

The structure with a polymer layer interface between the grating and the mirror allows a significant reduction of metallic losses in the QD range, as well as improved QD photocurrent. For comparison, a structure with the Ag layer deposited directly on the AlInP triangular grating observes QD region J_{SC} that is 45 % lower relative to the optimized triangular grating with the planarizing polymer. This corresponds to a notable difference in QD photogeneration enhancement, going from 3.69 times for the Ag on AlInP to 6.72 times for the planarized triangular grating, with a similar trend observed for pyramidal gratings.

2.6 Double-side gratings

After independently exploring the possibility to improve both the light trapping and anti-reflection by designing periodic nanostructures, the two approaches are combined and their impact on the solar cell is assessed.

In order to systematically study the impact of front- and back-side gratings, the five solar cells shown in Fig. 2.2 are simulated, which are obtained modifying the single-pass device described in Table 2.1, from here on used as reference. In cell (a)

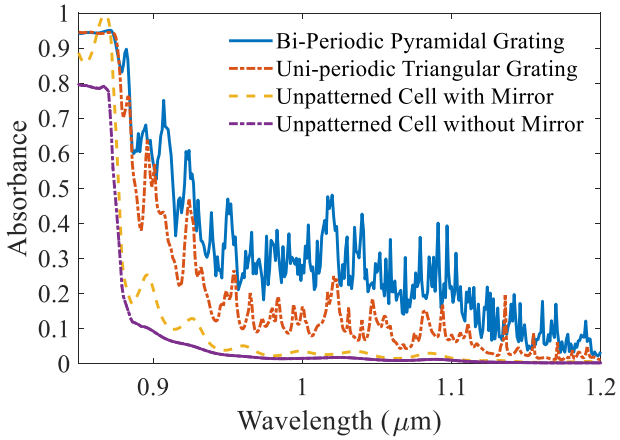

Figure 2.13: Absorbance comparison for the simulated cell structures employing a back-side grating only and planar ARCs. The grating height (h) is 1.05 μm and period (Λ) is 3.1 μm for both the triangular and pyramidal gratings.

a 200 nm thick Ag mirror is introduced after the BSF, making the cell double-pass. In cell (b), compared to cell (a), the top 80 nm SiNx ARC layer is replaced by the previously described AlInP front-side grating, having a period of 215 nm and height of 400 nm. The nanostructured AlInP ARC provides a smooth gradient of the index from air to the AlInP window layer. In cell (c), compared to cell (a), the previously designed AlInP/SU-8 back-side grating has a period = 2.4μm, height = 0.9μm, and a 150 nm thick separation SU-8 layer (measured from the pyramid corner) is included between the BSF and the Ag planar mirror. Cell (d) includes both front- and back-side gratings. Finally, cell (e) features a conformal SiN_x layer on top of the front-side ARC grating, which further improves its antireflection properties.

2.6.1 Impact of double-side texturing

As shown in Fig. 2.14 (a), the integration of the high-index AlInP nanostructured ARC provides a significant reduction of the front-side reflectance. A further improvement is achieved by further matching the refractive index of air to that of AlInP using a conformal SiN_x layer. The improvement obtained due to the use of front nanostructures and back diffraction gratings is measured by examining the active region absorbance (GaAs and QD layers) in Fig. 2.14 (b) and its corresponding photocurrent at AM0 illumination.

The enhancement of the five solar cell configurations is quantified as the ratio of their short-circuit current to that of the single-pass reference structure. The photocurrent in QD absorption range $J_{SC,QD}$ enhancement is reported in Fig. 2.15. Devices (a) and (b), which are double-pass cells (not including light trapping features) exhibit an approximated $J_{SC,QD}$ improvement factor of 2, and the grating

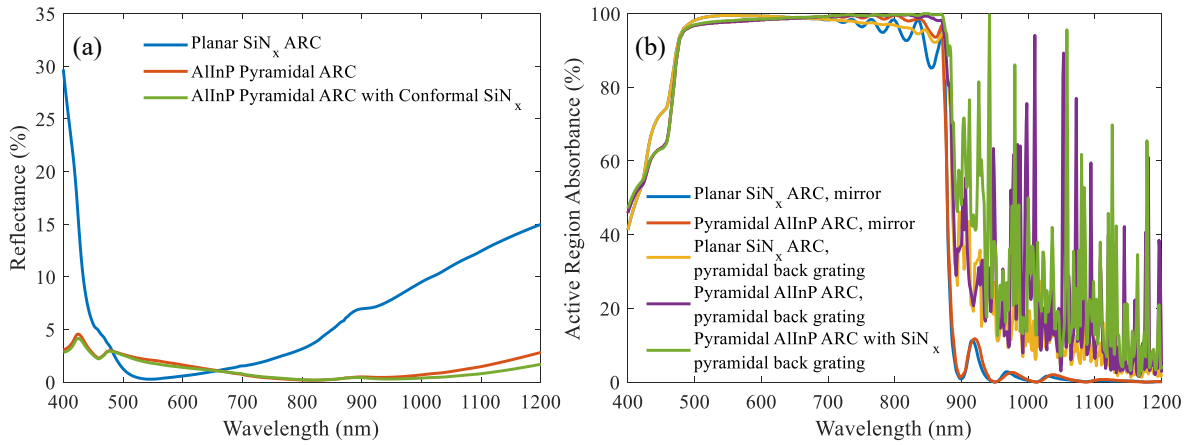

Figure 2.14: (a) Front-side reflectance comparison between the unpatterned ARC, nanostructured AlInP ARC, and the nanostructured ARC with a conformal SiN_x layer. (b) Absorbance comparison between the planar reference cell, cell with nanostructured (nano) ARC with mirror, cell with planar ARC and back-side grating, cell with nano ARC and back-side grating, and a cell with dual-layer nano ARC and back-side grating.

ARC (b) results to be slightly more effective than the planar one (a). A major improvement of approximately 18 times is observed for cell (c), which includes light trapping features. Cells (d) and (e) exhibit a significant conclusion: including both the nanostructured anti-reflection coating and the diffraction gratings results in a $J_{SC,QD}$ enhancement much larger than the combination of the individual contributions. Cell (e) (double-sided grating cell with AlInP front and back-side gratings) exhibits a short circuit current 32 times larger than the reference single-pass counterpart, which is promising towards overcoming the low absorption issues faced by thin-film QD solar cells. This enhancement corresponds to an equivalent absorption of 320 QD layers as opposed to realistic growths of approximately 10 QD layers. The structure with a planar ARC, back side grating, and reflecting mirror also results in a photocurrent enhancement of approximately 18 times.

2.6.2 Light trapping enhancement analysis

In view of achieving deeper insight into the results reported in Fig. 2.15, an analysis based on the methodology described in [61] is now implemented. This is a post-processing of the diffraction efficiencies $\eta_{\mathrm{D},k}$, which quantify incident light coupling into each k-th order diffracted by the grating. The optical path enhancement factor F is related to the wavelength-dependent absorption efficiency $A(\lambda)$ defined in Equation (2.2) through the expression:

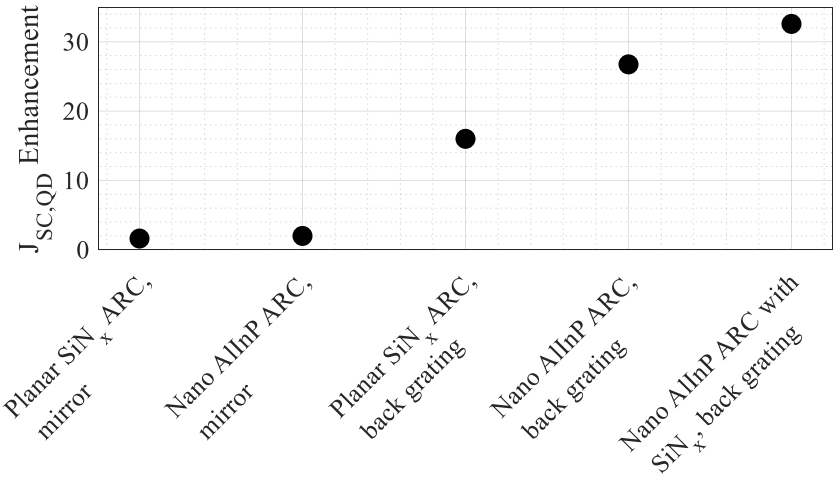

Figure 2.15: Short circuit current density enhancement comparison between the different cell configurations for the QD absorption region ($\lambda = 895$ nm to 1200 nm).

$$A(\lambda) = \frac{\alpha(\lambda) d_{\text{act}}}{\alpha(\lambda) d_{\text{act}} + \dfrac{1}{F}}, \tag{2.4}$$

where d_{act} is the thickness of the photoactive region (40 nm QD stack in our case study), and the absorption profile from Fig. 2.16a has been used for the computations. This expression can be plugged in Equation (1.4) to compute the short circuit current in the QD absorption range, and F can be determined as the value fitting the results of Fig. 2.15, which are obtained with the Beer-Lambert (BL) model [76]. As it is shown in Table 2.2, $F = 2$ for cells (a) and (b). This is clear as both are double-pass with no back-side diffraction grating, so light crosses a maximum of twice the active region. The estimated mean light path enhancement factor in the QD absorption region is 18 for cell (c), 35 for cell (d), and 45 for cell (e), following the trend of the results obtained by the Beer-Lambert law.

Once the factor F is estimated, it is deconstructed as:

$$F = 2 \frac{\overline{d_{\text{eff}}}}{d_{\text{act}}} \frac{1}{P_{\text{esc}}}, \tag{2.5}$$

where the factor of 2 is related to the use of a back reflector, P_{esc} is the mean probability of light escape from the active region towards the front surface, and $\overline{d_{\text{eff}}}$ is the mean normalized effective thickness. The quantity $\overline{d_{\text{eff}}}$ is computed as:

$$\overline{d_{\text{eff}}} = \overline{\sum_{k=-N_{\text{h}}}^{N_{\text{h}}} \frac{d_{\text{act}}}{\cos(\vartheta_k(\lambda))} \eta_{\text{D},k}(\lambda)}, \qquad \lambda \in (0.895 - 1.2)\,\mu\text{m}. \tag{2.6}$$

Both diffraction efficiency and order angles depend on wavelength; therefore, this expression is the sum of the effective thicknesses experienced by each k-th diffracted order (*i.e.,* $d_{\mathrm{act}}/\cos(\vartheta_k)$), weighted by the corresponding diffraction efficiencies. Applying these models to the studied cells in the QD absorption region provides $\overline{d_{\mathrm{eff}}}$ of 1.41 for cell (c), of 1.50 for cell (d), and of 1.50 for cell (e). Having computed these values, it is possible to estimate the probability of escape for each of these cells, resulting to be 15.67 % for cell (c), 8.61 % for cell (d), and 6.7 % for cell (e). Finally, to give an idea of the double-sided grating solar cell performance compared to the theoretical limit, Fig. 2.16b shows the wavelength averaging, $d_{\mathrm{eff}}(\lambda)/d_{\mathrm{act}}$ for the double-sided grating solar cell (solid blue curve), compared to the theoretical limit estimated by Yablonovitch [16] ($\overline{d_{\mathrm{eff}}} = 2d_{\mathrm{act}}$ and $F = 4n^2$ being n the refractive index of the active region, dashed black line) and to the starting planar mirror structure ($\overline{d_{\mathrm{eff}}} = d_{\mathrm{act}}$ and $F = 2$, dotted black line), demonstrating the impact of this solution. Finally, the QD photocurrent collection efficiency ($\eta_{J_{SC,QD}}$) is computed by normalizing the collected $J_{SC,QD}$ with the maximum attainable photocurrent for $\lambda_i = 0.895$ μm to $\lambda_f = 1.2$ μm at AM0 illumination, with the comparison shown in Table 2.2.

Table 2.2: QD photocurrent collection efficiency ($\eta_{J_{SC,QD}}$) at AM0 illumination and light trapping properties comparison of the simulated cell structures for the QD region ($\lambda_i = 0.895$ μm to $\lambda_f = 1.2$ μm).

Parameter	Cell (a)	Cell (b)	Cell (c)	Cell (d)	Cell (e)
$\eta_{J_{\mathrm{SC,QD}}}$ (%)	1.38	1.71	14.27	23.16	28.40
F	2	2	18	35	45
$\overline{d_{\mathrm{eff}}}$	-	-	1.41	1.50	1.50
P_{esc} (%)	-	-	15.67	8.61	6.67

An alternative analysis is performed, based on the light trapping efficiency η_{LT} [62] as a figure of merit:

$$\eta_{\mathrm{LT}} = \frac{J_{\mathrm{max}} - J_{\mathrm{ref}}}{J_{\mathrm{LL}} - J_{\mathrm{MB}}}. \tag{2.7}$$

Here, J_{max} and J_{ref} are the short-circuit currents of the structure under analysis and of an identical structure featuring a planar back-side mirror without any diffraction grating, J_{LL} is achieved with a perfect antireflection coating and a Lambertian reflector, also referred to as the Yablonovitch limit, and J_{MB} is obtained using a perfect metal back-side reflector, also referred to as the dual-pass limit.

Since this analysis focuses on light trapping enhancement (*i.e.,* on the back-side grating) considering equal front-side ARC, cell (c) can be compared only with (a), resulting in a η_{LT} estimate of 0.51, cell (d) can be compared only with (b),

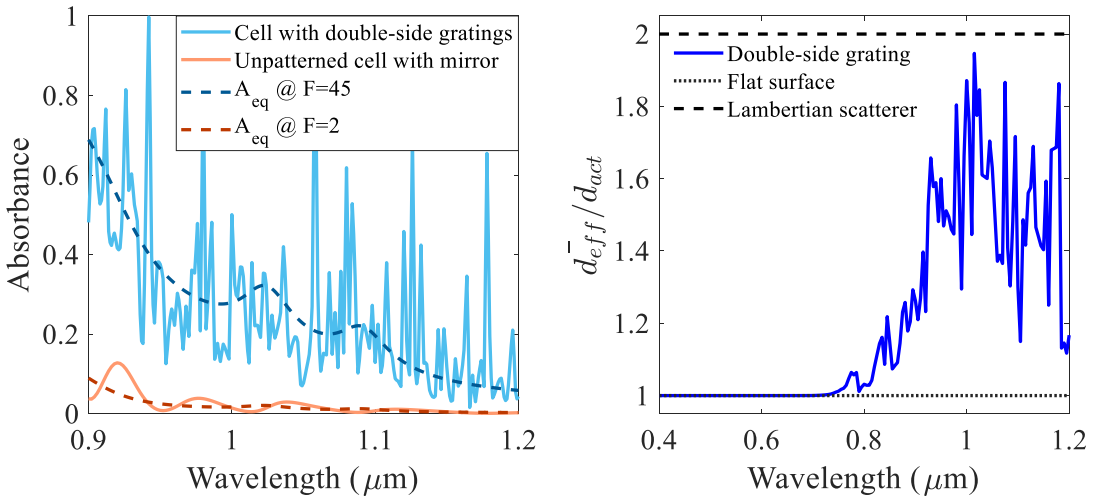

(a) (b)

Figure 2.16: (a) Active region optical absorbance for the structures used in the light trapping analysis. (b) Mean normalized effective thickness at different wavelengths for the structure with double-side pyramidal gratings.

resulting in a η_{LT} estimate of 0.79, and cell (e) can be compared to a cell with a planar back-side mirror and the same front-side ARC, resulting in a η_{LT} estimate of 0.95.

2.7 Conclusions

A light trapping design methodology was investigated, which applies several configurations of front-side nanostructured subwavelength ARCs, back-side diffraction gratings, and Ag mirrors for thin-film quantum dot solar cells using full-wave electromagnetic simulations based on the RCWA method. Optimizations for the front and back-sides were independently performed for antireflection and diffraction, respectively. The double-side grating results in the highest effective optical path length enhancement, allowing a QD photocurrent enhancement that can mitigate the low absorption issue. Accordingly, the requirement for intricate strain balanced epitaxial growth to achieve an increased number of QD layers is minimized, as well as the open circuit voltage penalty due to the addition of a QD stack. The proposed structures provide a useful frame of reference for the design and analysis of light trapping enhanced thin-film QD solar cells.

Chapter 3

Fabrication and characterization of diffraction gratings

3.1 Introduction

In this study, different structures were simulated and fabricated for assessing diffraction efficiencies and their dependence on the design features. The structures integrating gratings with the back reflectors were previously simulated to find the optimum dimensions for absorption near the GaAs absorption edge. According to these simulations, the maximum photocurrent is achieved when the height-to-period aspect ratio is 0.32–0.38, which was employed to fabricate the gratings in this work.

First, fused silica (glass) samples were utilized as substrates for tuning of the optical models as well as for characterizing the diffraction gratings in the absence of an absorbing active region, which is generally composed of GaAs. Using transparent substrates allows viewing of the diffraction characteristics throughout the entire visible and Near IR spectra. The unpatterned samples are simulated using the transfer matrix method (TMM) and the optical models are tuned in order to provide the highest possible matching between measured and simulated results. Next, the gratings fabricated on GaAs wafers are simulated in order to quantify their impact on diffraction for QDSCs. The grating simulations are performed using the RCWA method in order to obtain their direct and total reflectance as well as the diffraction efficiency for some of the propagating modes.

The work presented in this Chapter is based on "Comparison of metal/polymer back reflectors with half-sphere, blazed, and pyramid gratings for light trapping in III-V solar cells", T. Aho, M. Guina, F. Elsehrawy, F. Cappelluti, M. Raappana, A. Tukiainen, A. K. Alam, I. Vartiainen, M. Kuittinen, and T. Niemi [52].

3.2 Diffraction gratings on glass substrates

3.2.1 Grating patterning process

The gratings were fabricated at the Tampere University (TU) laboratories (as a joint effort between the candidate and the solar cells team at TU) using nanoimprint lithography (NIL) on a polymer following a process developed by the Optoelectronics Research Centre at the University. To this end, a commercial OrmoComp NIL photoresist (Micro Resist Technology GmbH) [77] was utilized to implement a uni-periodic blazed grating and a bi-periodic pyramidal grating. A commercial master (Thorlabs) was used for the blazed grating and an in-house fabricated Si master for the pyramidal grating. Using the NIL processes, the gratings were transferred from the masters to polydimethylsiloxane stamps, in order to be imprinted onto the NIL photoresist.

The process includes multiple steps to realize the polymer gratings, which are followed by the deposition of the metal film to obtain textured reflectors. The OrmoComp polymer is deposited on clean glass substrates, and then a spin coating technique is used to spread an even distribution of OrmoComp on the surface. Next, multiple thermal cycling steps are performed in order to further dispose of any trapped air particles in the polymer and to obtain higher surface uniformity. Then, the planar samples undergo a period of exposure to ultraviolet (UV) radiation in order to harden the polymer. For other samples, gratings are imprinted using previously fabricated stamps to obtain blazed- and pyramid-shaped gratings, while simultaneously being exposed to UV radiation in order to harden the polymer taking the shape of the gratings. A final thermal cycle is performed as an additional measure to ensure structural integrity.

The fabricated gratings have aspect ratios within the optimized range, as the blazed grating has a height of 1.2 μm and a period of 3.2 μm and the pyramid grating has the height of 700 nm and the period of 2.5 μm. Next, a Ag layer was deposited using electron beam evaporator on top of the polymer layer for planar and grating samples. The Ag thickness of around 200 nm is found to be sufficient in order to prevent peeling off of the layer as well as providing high reflectivity.

Additional samples were fabricated using a different architecture that incorporates a planarization layer to compare both textured and planarized reflectors. The final processed glass samples are shown in Fig. 3.1 and their multilayer structures are detailed in Table 3.1. The two main architectures under study are demonstrated in Fig. 3.2, and comprise of:

1. OrmoComp gratings with a conformal Ag layer directly deposited resulting in a patterned back reflector.

2. OrmoComp gratings with a conformal TiO_2 layer followed by a polymer (SU-8) planarization layer, and a planar Ag back reflector.

Figure 3.1: The reference and processed glass samples are shown after completing the NIL process for patterning of the diffraction gratings and deposition of the back reflectors.

In the first configuration, diffraction originates from the patterned reflectors according to the grating dimensions. In the second configuration, the diffraction would result from the index difference at the grating interface between the polymer and TiO_2, and the transmitted light would be reflected at the planar reflector to be again diffracted by the gratings. The aim of planarizing the reflecting mirror is due to the previously mentioned concerns of plasmonic absorption due to curved metallic surfaces.

3.2.2 Optical characterization

The optical characterization of the glass samples was performed by the candidate at the Optoelectronics Reseach Centre laboratory. The specular (direct) reflectance was measured at an 8° incident angle using the PerkinElmer Lambda 1050 spectrophotometer, while the total reflectance was measured using its integrating sphere module. Transmittance measurements were also performed using an additional module for samples without integrated reflectors on the back-side. The specular reflectance and transmittance measurements assume air as the medium before and after the samples, and similar boundary conditions are considered in the TMM simulations. The integrating sphere module provides a white reflecting background behind the sample, which is modelled as a lossless reflector for samples that are not terminated with a Ag layer. In addition, some integrating sphere measurements were repeated with a black absorbing background just behind the sample in order to account only for reflections caused by the samples. The difference between the specular and total reflectance provides an estimate of the amount of diffuse light that is diffracted within the cell.

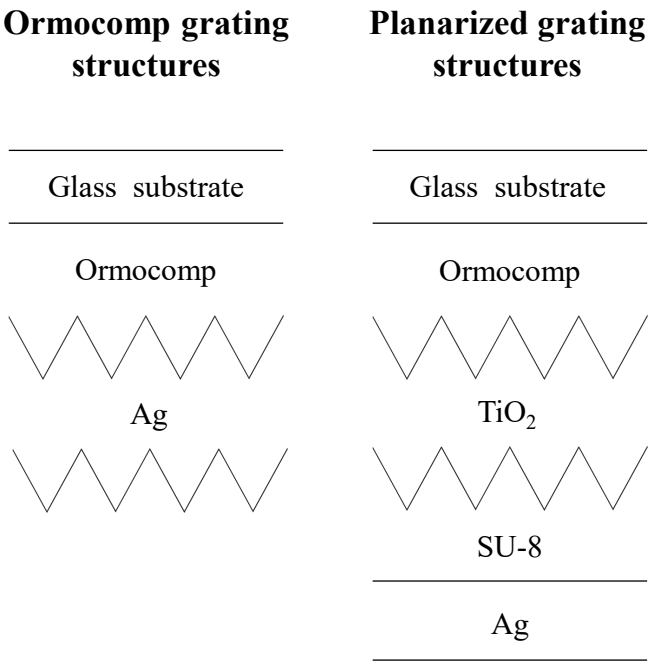

Figure 3.2: The OrmoComp gratings (left) and planarized gratings (right) architectures are displayed, for the case of structures with uni-periodic gratings. For the planar reference structures, the NIL process is not performed, resulting in planar layers.

Initially, the reference glass samples are measured to calibrate the optical models. The specular reflectance and transmittance are measured for the plain glass samples, glass with TiO_2, and glass with TiO_2 and SU-8. The structures are also simulated using TMM in order to ensure that the optical properties observed through the measurements are in line with the numerical models. The structures were modelled without taking account for geometrical imperfections. A comparison is shown in Fig. 3.3, where high qualitative agreement is demonstrated between measured and simulated results. However, the glass substrates exhibit slightly higher reflectance that could be attributed to material defects or microscopic scratches on the glass.

Next, the planar OrmoComp and the planarized samples are characterized and simulated. The samples are examined in terms of their specular reflectance and transmittance, which are shown in Fig. 3.4. The planar structure composed of glass and OrmoComp is compared to the second architecture with TiO_2 and SU-8 added. The examined structures exhibit strong correlation with the measurements despite the added complexity of the multilayer structure. As anticipated, adding the backside Ag reflector provides high reflectance for both architectures in simulations and measurements.

Table 3.1: Structural description of the analyzed glass samples in this study. The layer compositions are listed in order, starting with the surface at which light is incident.

Reference structures	**Composition**
Reference glass	≈ 1mm glass substrate
Reference glass w/TiO_2	glass, 200 nm TiO_2
Reference glass w/TiO_2 + SU8	glass, 200 nm TiO_2, 3000 nm SU-8
OrmoComp grating structures	**Composition**
Planar	glass, 3800 nm planar OrmoComp
Planar and Ag Reflector	glass, 3800 nm planar OrmoComp, 200 nm planar Ag
Blazed grating	glass, 3800 nm textured OrmoComp, 200 nm conformal Ag
Pyramid grating	glass, 3800 nm textured OrmoComp, 200 nm conformal Ag
Planarized grating structures	**Composition**
Planar w/TiO_2 + SU8	glass, 200 nm TiO_2
Planar w/TiO_2 + SU8 and Ag Reflector	glass, 3800 nm planar OrmoComp, 200 nm planar TiO_2, 3000 nm planar SU-8, 200 nm planar Ag
Blazed grating w/TiO_2 + SU8	glass, 3800 nm textured OrmoComp 200 nm conformal TiO_2, 3000 nm planarizing SU-8, 200 nm planar Ag
Pyramid grating w/TiO_2 + SU8	glass, 3800 nm textured OrmoComp 200 nm conformal TiO_2, 3000 nm planarizing SU-8, 200 nm planar Ag

Total reflectance measurements are obtained using the integrating sphere module for both black and white backgrounds, indicating an absorbing or reflecting boundary condition for the cell back-side, respectively. The results for the reference

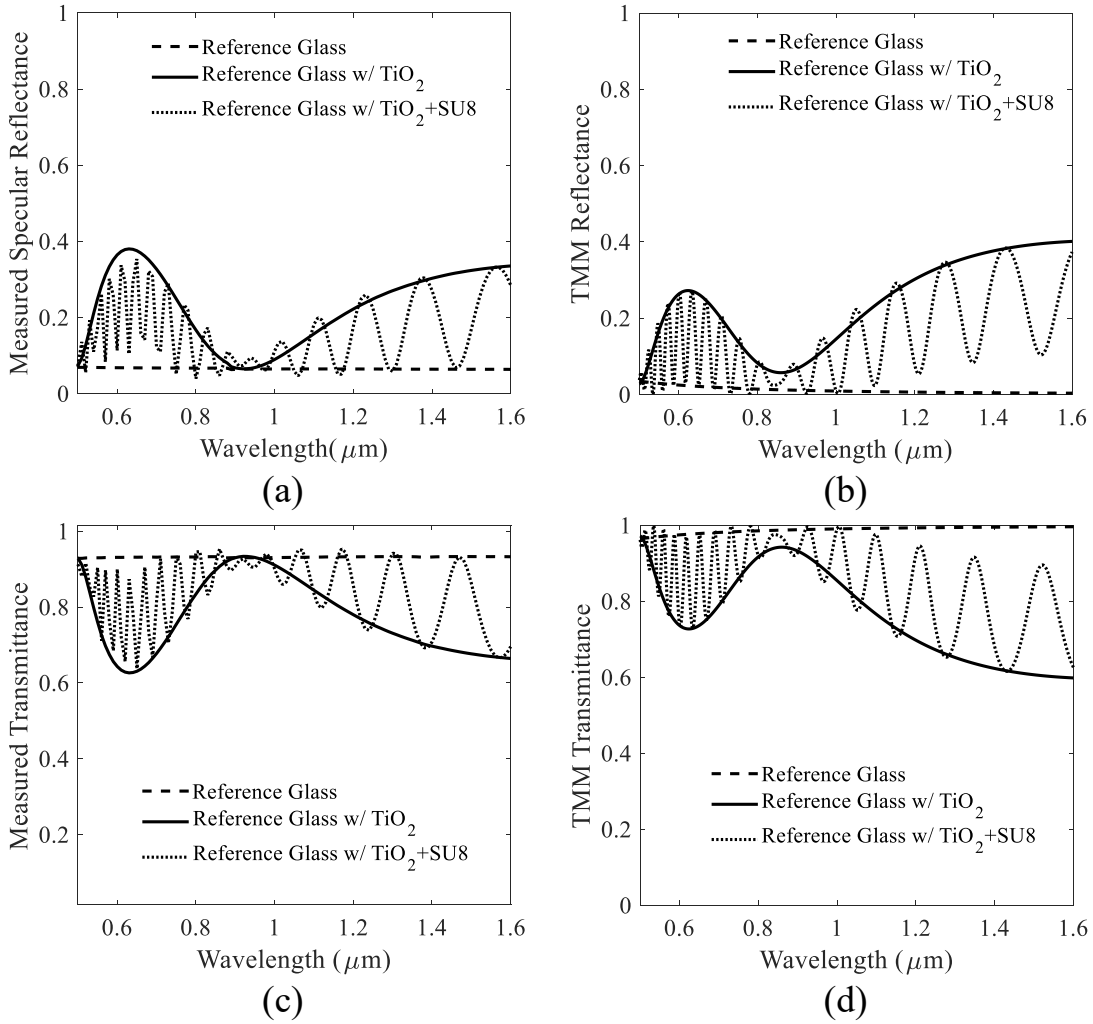

Figure 3.3: (a) The measured and (b) TMM simulated specular reflectance of the reference samples. (c) The measured and (d) TMM simulated transmittance of the reference samples. The simulations exhibit strong matching with the experimental results.

glass samples are shown in Fig. 3.5 (a) and those of the planar structures incorporating OrmoComp are shown in Fig. 3.5 (b). The integrating sphere measurements of the reference glass using the reflecting white background do not display the differences between the structures, while those using an absorbing black background clearly demonstrate the impact of the additional layers. The measurements show the combined influence of the conformal TiO_2 and SU-8 layers, which increase the total reflectance due to the added index mismatch between the multilayers.

The patterned samples are then characterized and compared in terms of their diffractive properties. The results of the measurements are displayed in Fig. 3.6 (a).

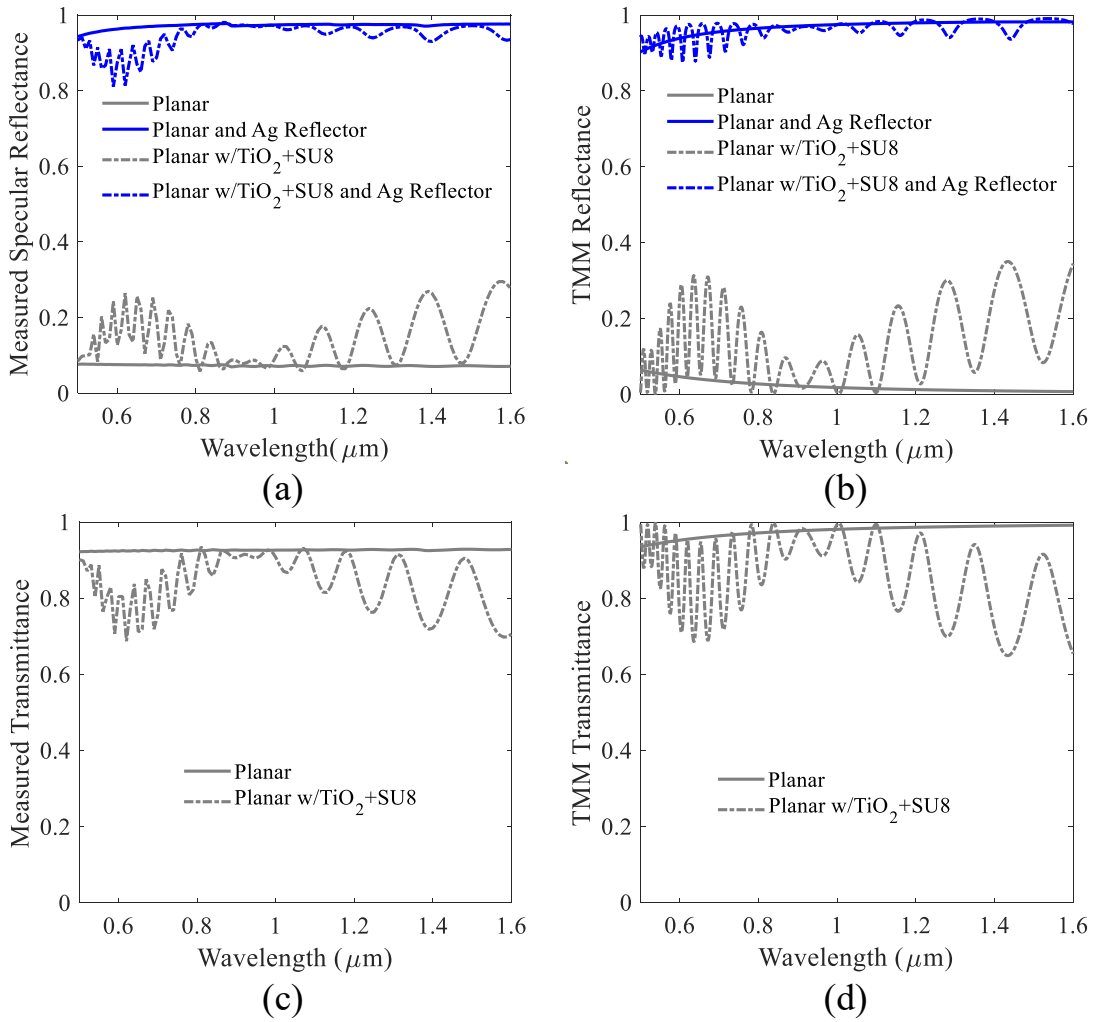

Figure 3.4: (a) The measured and (b) TMM simulated specular reflectance of the planar samples for both architectures (OrmoComp only vs. OrmoComp with TiO_2 planarized with SU8). (c) The measured and (d) TMM simulated transmittance of the planar samples.

The aim is to maximize the amount of light diffracted within the structure due to the gratings. The OrmoComp structures exhibit better diffraction of light due to the significantly higher grating index difference as opposed to the low grating index difference for the planarized structures. The planarized structures show higher total reflectance than the OrmoComp samples for all planar and grating samples due to the planarization of the back reflector. Seeing as the estimate of diffuse light relies on the reflectance difference, a lower direct reflectance for a constant total reflectance indicates higher diffraction. The planar samples exhibit the highest total reflectance as there are minimal metallic losses, with the pyramid and blazed

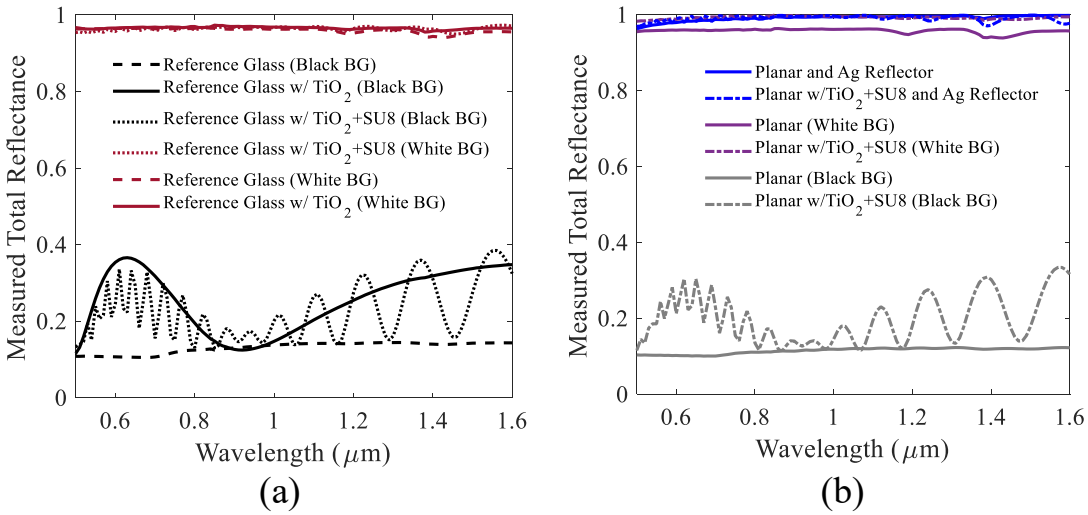

Figure 3.5: The integrating sphere measurements of (a) the reference and (b) the planar samples, utilizing black and white backgrounds as the object after the sample. This allows observation of the impact of the different boundary conditions.

grating structures showing lower total reflectance. The diffraction effect is reduced for the planarized samples due to the small refractive index difference at the grating, and this architecture is found to be less effective than the textured reflectors on polymer (OrmoComp grating structures).

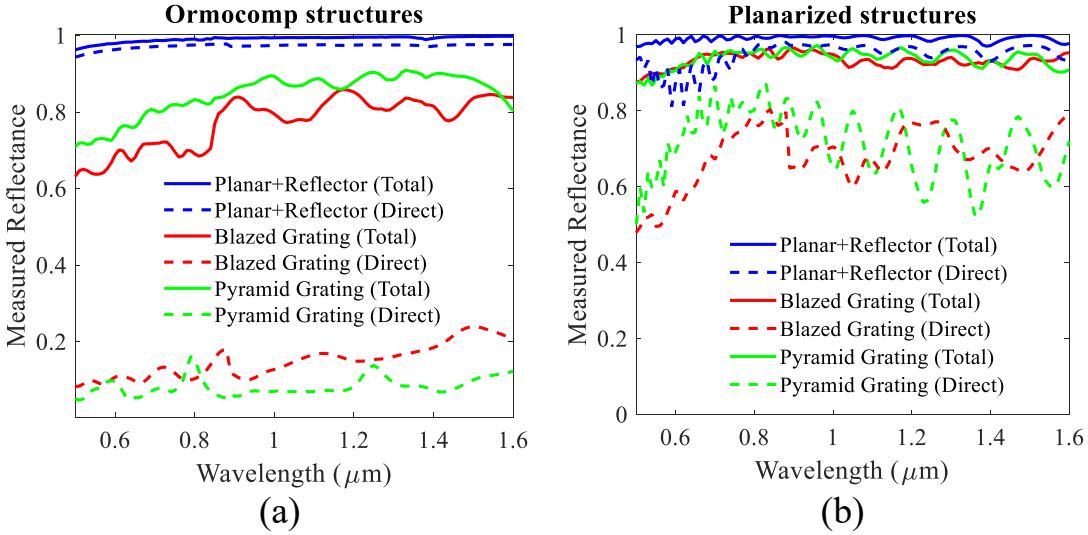

Figure 3.6: The measured specular and total reflectance is shown for (a) the OrmoComp structures and (b) the planarized structures (with TiO_2 and SU-8).

3.3 GaAs solar cells with patterned reflectors

To examine the impact of diffraction gratings on light trapping in the wavelength range of interest, back-side grating structures were fabricated on GaAs wafers at the Optoelectronics Research Centre of the Tampere University by the solar cells team at TU and their optical characterization was performed. During the candidate's mobility period, the optical characterization of the cells was replicated to enable a well-informed approach to their modelling.

A double-side polished semi-insulating GaAs (SI-GaAs) wafer with a thickness of 350μm was used as a substrate. Single-layer SiN_x antireflection coatings (ARCs) were deposited by plasma enhanced chemical vapor deposition on the both sides of the substrate. The front ARC was optimized to minimize the reflectance at the air/GaAs interface, while the backside ARC was optimized to minimize the reflectance at the GaAs/polymer interface. The properties of the SiN_x layers were tuned by varying the process parameters such as NH_3 and SiH_4 gas flows and time. The ARC thicknesses and refractive indices are presented in Fig. 3.7, which also introduces the three structures and the planar references.

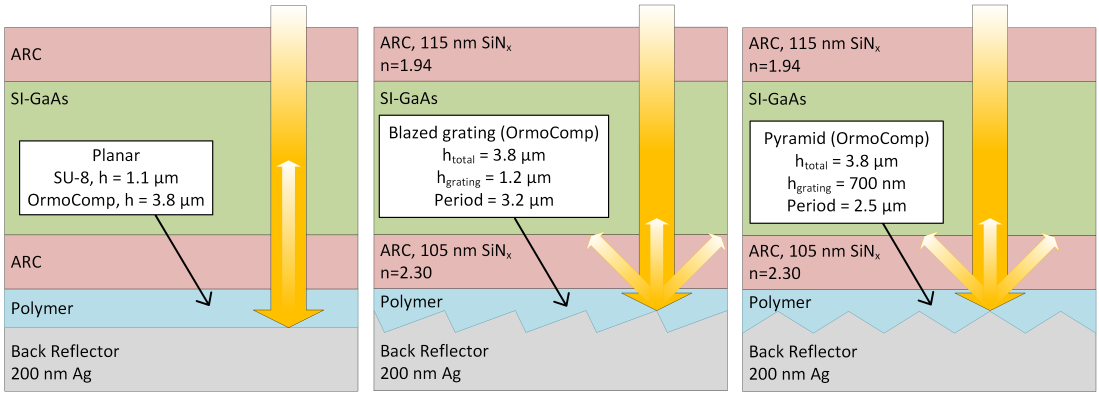

Figure 3.7: The structural composition of the different samples fabricated by the Tampere University with diffraction gratings on GaAs wafers. A planar reference structure (left), a structure with uni-periodic blazed grating (middle), and a structure with a bi-periodic pyramid grating (right) are displayed. The figure is adapted from [52].

3.3.1 Optical simulation methodology

The fabricated grating structures were simulated using the RCWA method and the planar structures were analyzed with TMM. The gratings are designed for both 2D (linear gratings) and 3D (crossed gratings) configurations. In the 2D

simulations, the results are an average of the TE and TM polarizations for each of the diffraction orders. In the 3D case, the gratings are symmetric and therefore both polarizations are equal for direct incidence (i.e. θ_{inc}=0°).

The simulated gratings have the nominal geometrical features, i.e. flattening and rounding of the grating shape due to processing imperfections were not taken into account in the simulations. A convergence study showed minor changes in the average reflectance over a wide range of wavelengths. As presented in Fig. 3.8, a minimum of around 8–10 harmonics were found to be sufficient to reach a reasonable accuracy while avoiding an excessive computational cost. Accordingly, all the presented simulations use 10 harmonics (i.e. Fourier order=21) for each in-plane direction A similar trend was also observed for 3D structures. Numerically, the grating structure is approximated by a layered geometry with a spatial resolution of 70–75 nm. The optical models for GaAs and Ag are obtained from [66], while constant real refractive indices are used for the ARC layers (see values in Fig. 3.7) and for the polymers (n=1.51).

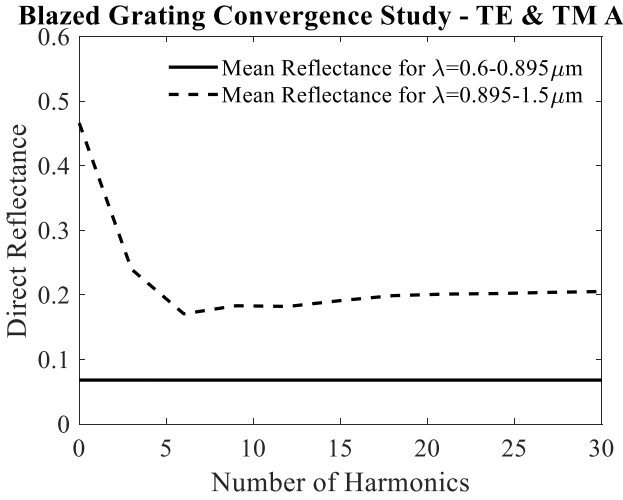

Figure 3.8: Number of harmonics vs. the mean reflectance for the wavelength ranges corresponding to a portion of the GaAs absorption (λ=0.6–0.895μm) and the QD absorption (λ=0.895–1.5μm).

One limitation of the RCWA method lies in the simulation of structures thicker than the coherence length of sunlight (around 1μm), because fictitious interference effects cause high-frequency noise. Such artifacts can possibly be eliminated by using the methodology presented in [78], where the results of the thick slab are averaged over wavelength or for multiple thicknesses (varying by a few percentage points). In this work, the results were obtained by varying the substrate thickness of $\pm$5μm in 5 steps and averaging across the simulations. Further reduction of interference effects was then achieved by averaging the calculated reflectance spectra and diffraction efficiency over 10 nm wavelength interval.

3.3.2 Optical characterization

Diffuse reflectance

All the measurements were conducted through the SI-GaAs wafer and the performance of the back reflectors were evaluated at the wavelengths for which SI-GaAs is transparent. The measured and simulated reflectance for the blazed and pyramidal gratings are compared in Fig. 3.9, demonstrating high matching between experimental and numerical results. The reflectance measurements of the blazed grating and the pyramid grating are compared in Fig. 3.9 (a). The pyramidal grating results in the highest diffuse reflectance in the wavelengths corresponding to the photogeneration in InAs/GaAs QDSCs, relative to the blazed grating and planar reference structures.

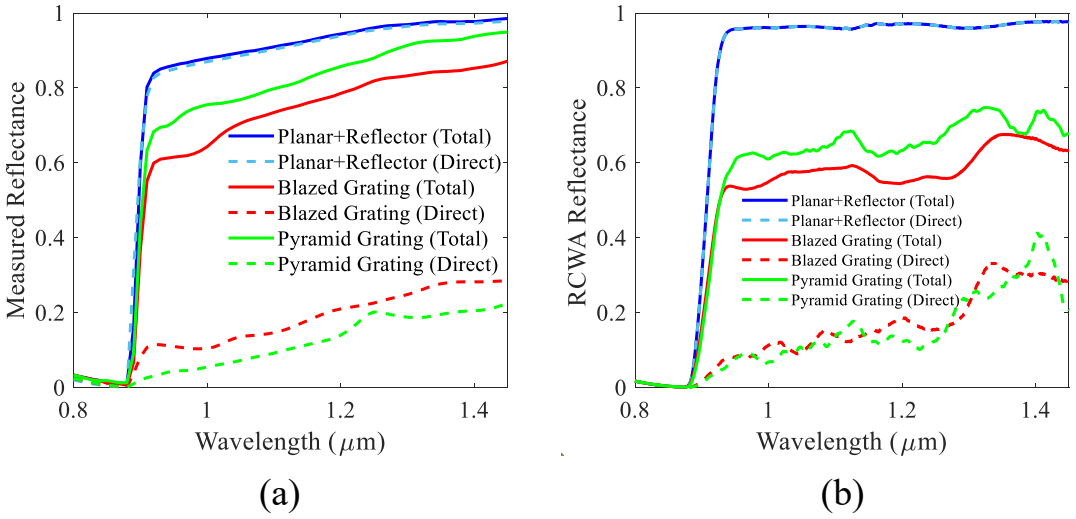

Figure 3.9: The RCWA simulated and measured reflectance of the planar reference, blazed grating, and the pyramid grating structures. The difference between the total and the direct reflectance represents the amount of diffracted light.

Since the blazed grating is asymmetrical, the diffraction orders are not symmetrical along the x-plane. Yet, the difference in measured reflectance for both directions of the blazed grating is negligible. The blazed grating shows low specular reflectance, which is beneficial for high diffraction of light. However, the total reflectance of the blazed grating was reduced compared to the pyramid grating, indicating the presence of additional losses in the structure, potentially originating from the surface plasmon resonance in the metal reflector. This behavior can also be seen in the simulations in Fig. 3.9 (b). In fact, the analysis of the calculated distribution of absorbed photon density pointed out large optical loss at the polymer/metal interface of patterned structures, whereas marginal optical loss were observed in the reflector of the planar structure.

The discrepancy between the simulated and measured reflectance is primarily caused by overestimation of the losses in the structured metallic reflector as well as coherence effects due to the use of the RCWA method. The simulated total reflectance for both the blazed grating and the pyramid grating is approximately 10 percentage points lower than the measured total reflectance. The lower loss observed in experiments could be attributed to a reduction of the SPR effect owing to the flattening of the fabricated structures with respect to the nominal ones. Moreover, some inaccuracy might originate also from the simple optical model adopted for the SiN_x and polymer layers. Nevertheless, an overall good agreement between measured and simulated trends is achieved, supporting the conclusions of the diffractive properties of the structures.

Regarding the planar reflector, the simulated total reflectance curve is horizontal, whereas the measured one is increasing towards higher wavelengths. This difference mostly arises from the residual absorption into SI-GaAs. From transmittance measurements across the SI-GaAs wafer, an extinction coefficient $k \approx 6 \times 10^{-6}$ was estimated, whereas the adopted GaAs optical model uses $k = 1 \times 10^{-6}$ above 890 nm.

Diffraction efficiency

To quantify the amount of the diffracted light, the spectral diffraction efficiency was measured at diffraction orders of m=0, 1, and 2. This measurement was carried out by variable angle measurement technique where the sample is illuminated by a white light beam at an incident angle of 8°. The diffracted light is collected at variable angles from 8° to 48° with an optical fiber connected to a spectrometer, shown in Fig. 3.10. As a result, the diffraction efficiency is defined as the diffracted power divided by the incident power. With the utilized system, only the diffraction orders within the escape cone of the SI-GaAs wafer can be measured. The measurements are performed after optimizing the intensity integration time and performing two calibration steps consisting of first subtracting the measured noise in dark conditions and then normalizing the measured intensity by the reflected light intensity of a silver mirror.

The diffraction efficiency results of the blazed and pyramid gratings are presented in Fig. 3.11 (a). At m=0, a small difference between the 8° and -8° angles of incident light is noticed, due to asymmetric grating, while the variations for higher orders are more noticeable. Due to the difficulty in measuring the fabricated gratings in multiple dimensions and directions due to limitations in the measurement setup, the available measured results are limited to m=0, 1, and 2.

The 2D and 3D RCWA simulations of the diffraction efficiencies, in Fig. 3.11 (b), support the measurements, despite imperfect matching. Regarding the blazed grating, the 2D simulations predict low frequency oscillations of the m=0 spectrum which were not observed in the experiments. Such oscillations could be attributed

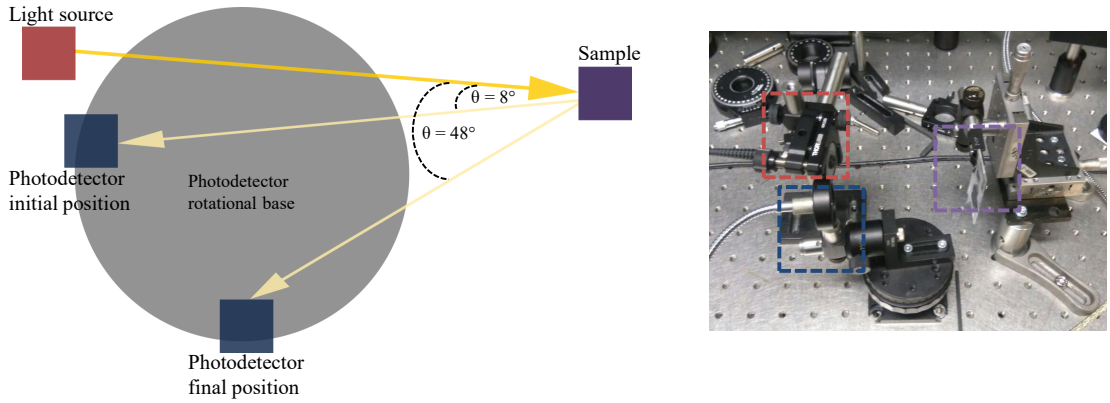

Figure 3.10: The measurement setup used to characterize the diffraction efficiency of the different samples. The different modes are measured at their respective angles.

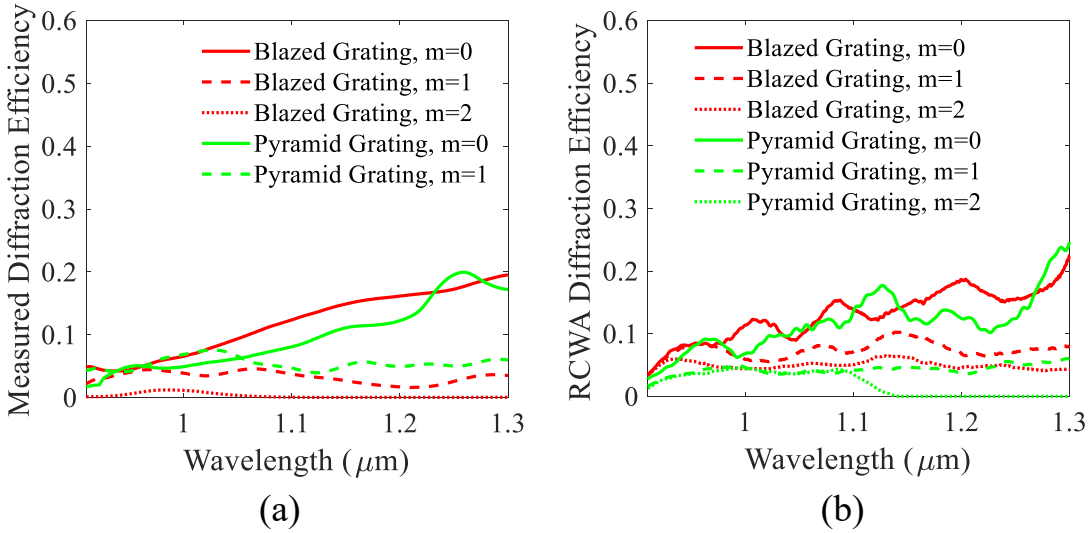

Figure 3.11: The RCWA simulated and measured diffraction efficiency of the planar reference, blazed grating, and the pyramid grating structures. The different modes are measured at their respective angles.

to the onset of a Fabry-Perot cavity effect in the polymer layer. The wavelength period (about 75–80 nm at λ=1050 nm) is in fact well correlated with the polymer thickness and the oscillations were mainly visible in the TE polarization, which suffers less for the optical loss at the polymer/metal interface. On the other hand, such interference effects are not visible in the experimental data due to the non-uniformity of the fabricated polymer layer.

In the pyramid grating measurements, power coupling to the first diffraction order is observed. The second diffraction order was not observed in the measurements, since they were performed up to a 48° angle, where m=2 is not yet present. However, according to the simulations, there is power coupling also to the second diffraction order. Furthermore, the m=0 diffraction order is well in line with the specular reflectance results, previously shown in Fig. 3.9 (a).

3.3.3 Thin-film QDSCs with textured reflectors

Implementing the textured metal/polymer back reflectors in a thin-film QD solar cell can provide significant enhancement of the QD photogenerated current, despite the lower index of the polymer relative to the previously studied AlInP diffraction gratings. As an example, a QDSC structure can be considered which contains a 2.6μm thick GaAs active region embedding a stack of 20 InAs/GaAs QD layers with overall thickness of about 400 nm. The structure includes top and bottom ARC layers similar to those reported in Fig. 3.7. Further details on the structure can be found in [79]. The QD stack's optical model was adapted from the previously mentioned models. Figure 3.12 shows the calculated absorbance spectrum for the QDSC in the substrate-based configuration and for two thin-film configurations, one with planar backside reflector and one integrating a pyramid backside grating. The grating has period of 3μm and height of 0.75μm and is terminated by a 200 nm thick Ag mirror. The absorbance spectrum is calculated by integrating the absorbed photon density only in the cell active region (i.e. low-doped GaAs and QD stack), and thus is not affected by optical loss in the contact and metal layers.

The pyramid grating shows a significant increase of absorbance in the QD wavelength region with respect to the reference structures. The light trapping scheme using patterned reflectors on polymer allows for up to a four times increase of current density from the quantum dot stack. Further optimization of the structure and the use of higher index materials for the grating yields higher current enhancement, as shown in the studies using double-sided gratings.

3.4 Conclusions

Samples with integrated diffraction gratings have been fabricated and characterized as a proof of concept. Simulations and experimental results of structures incorporating back-side gratings demonstrated the advantages of texturing to achieve significant light trapping. Structured metal/polymer back reflectors were studied for the III-V solar cells with the blazed and pyramid gratings processed using NIL. Simulations results obtained by the TMM and RCWA simulations exhibit strong agreement with the optical characterization for samples fabricated on both glass

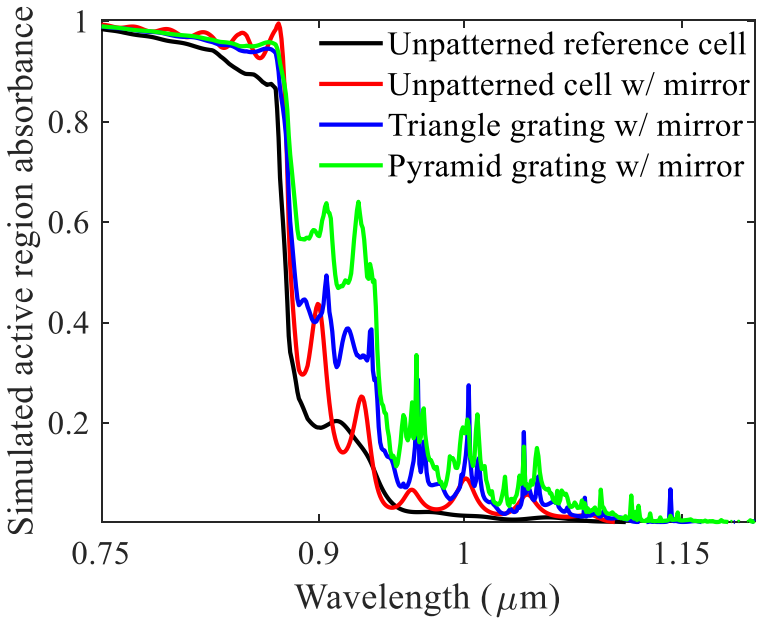

Figure 3.12: The RCWA simulated spectral dependence of the active region absorbance in a reference planar cell without mirror, planar cell with mirror, cell with a uni-periodic triangular grating and conformal mirror (period=3μm, thickness=0.75μm), and cell with bi-periodic pyramidal grating and conformal mirror (period=3μm, thickness=0.75μm). Average TE and TM polarization is used for 2D simulations.

and GaAs substrates. Efficient diffraction of light was observed for the polymer gratings with metallic reflectors deposited directly on them as opposed to the low index TiO_2 gratings. Even higher enhancement is attainable using high index materials (e.g. AlInP) to fabricate bi-periodic back-side gratings and reflectors as in the previous optimizations, which are more challenging to process. Nevertheless, both simulations and measurements indicate significant potential for improving the absorption and hence the photocurrent generation in thin-film solar cells.

Chapter 4

Guided-mode resonance for intermediate band solar cells

4.1 Introduction

The ideal intermediate band solar cell overcomes Shockley-Queisser efficiency limit of single-gap cells through two-step absorption of below-gap photons [7]. III-V QDs can be used for the realization of IBSCs due to their confined states acting as the IBs between the valence and conduction bands. QD are well-suited for this purpose due to the electrical isolation of their confined states. However, the operation of QDSCs in the IB regime currently faces many challenges. First, the first and second photon absorption rates need to be similar. This requires optimization of the bandgaps and half filling of the intermediate band [80, 81, 82]. In addition, the intraband photon absorption competes with thermal escape of carriers at room temperature operation, resulting in difficulty in current matching [83]. One method that has been studied is illuminating the IBSCs with high solar concentration, which improve the cell characteristics due to the photofilling effects [84]. Alternatively, the absorption coefficients corresponding to the interband and intraband absorption need to be very high to overcome the carrier thermal escape process. However, one of the main limitations of QDs is their weak absorption due to the difficulty in fabricating high QD layer stacks and the open-circuit voltage penalty associated with them [36].

In this Chapter, guided-mode resonance (GMR) effects are investigated to enhance the weak near-infrared (NIR) interband and mid-infrared (MIR) intraband

---

The work presented in this Chapter is based on "Guided-mode resonance gratings for enhanced mid-infrared absorption in quantum dot intermediate-band solar cells", F. Elsehrawy, T. Niemi, and F. Cappelluti [74].

absorption in thin-film QDSCs operating in the IB regime[85]. The excitation of waveguide-mode resonances for absorption enhancement beyond the Yablonovitch limit has been extensively studied and is found to be promising [54]. Resonant waveguide-grating structures patterned on the surface of thin-film silicon cells on quartz substrate were proposed in [28, 29]. Enhancing QD optical transitions in the MIR range is also a key task in the development of QD infrared detectors (QDIP). The use of a GMR grating on the top surface and a distributed Bragg reflector on the bottom has been proposed in [86] to implement resonant-cavity enhanced QDIPs.

The use of GMR gratings enables a narrowband optical absorption enhancement that exceeds traditional Lambertian light trapping by relying on resonance between the diffracted and guided modes, where the solar cell is designed as a waveguide. The GMR effect requires an ultra-thin cell active region relative to the wavelength, unlike the cells with thick active regions previously studied in Chapters 2 and 3. In contrast with Lambertian light trapping using diffraction gratings, GMR gratings diffract the light to one or few diffracted waves that can couple to guided modes, and therefore require grating periods comparable to the enhanced wavelength. The previously studied diffraction gratings differ in that their period is much larger than the wavelength, resulting in several modes being excited by the gratings and the optically thick cells result in negligible waveguiding effects. This allows all the modes excited by the grating to be be coupled to modes that can propagate in the cell [11, 12]. Diffraction gratings with optically large periods allow decreased sensitivity to the wavelength and incident angle. The GMR gratings studied in this Chapter, however, employ small grating periods and active region thickness relative to the enhanced wavelength, resulting in few modes being excited by the grating [54]. GMR gratings therefore result in higher angular selectivity. Due to the ultra-thin active region, waveguide effects are prominent and only the excited modes coupling (or resonating) with the guided modes supported by active region will be coupled into the cell. This provides high OPL enhancement (even higher than the Lambertian limit) but in a narrower wavelength range. Due to the narrowband nature of the GMR effect, it can be tuned to provide high absorbance enhancement at the wavelengths corresponding to the first or second photon transitions of an IBSC system, with absorption coefficients α_{VI} and α_{IC}, respectively.

This Chapter begins by introducing the operating principle of GMR enhancement. The GMR effect is first investigated for interband absorbance enhancement of the first photon transition of IBSCs. Two architectures are investigated in which gratings are employed either on the front or the back-side of the cell. Next, the GMR effect is studied for intraband absorbance enhancement of the second photon transition. A typical IBSC system is then used as an example to demonstrate the GMR principles. Following the design and optimization of the grating, the absorbance enhancement results are presented. The proposed structure's performance at different IBSC configurations is addressed as well as its sensitivity to the angle

of incidence. Finally, the Chapter concludes with remarks on the applicability of such concepts to other devices.

4.2 GMR operating principle

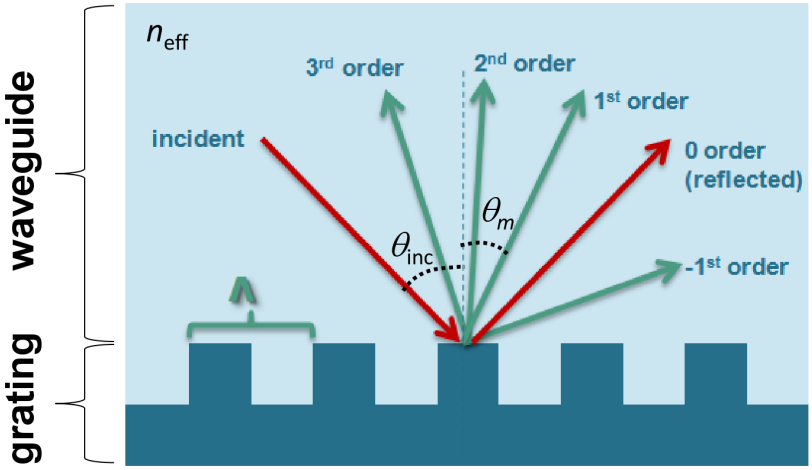

Figure 4.1: Schematic sketch of an elementary GMR structure composed of a slab waveguide characterized by effective index n_{eff} with a grating integrated at the rear side.

The GMR operating principle and designed solar structure are sketched in Fig. 4.1. To exploit waveguide-grating resonances, the solar cell is designed to be sufficiently thin ($\leq 1\,\mu$m) and with a sub-wavelength grating integrated on the front or back side. As shown in Fig. 4.1, GMR arises when the diffracted orders excited by the grating couple the incoming light into one or few waveguide modes. Thus, a phase matching condition must occur between the evanescent diffracted waves excited by the grating and the waveguides modes supported by the waveguiding structure [85, 29]. Under the hypothesis of a uni-periodic grating with weak index modulation, the resonances with a guided mode of effective index n_{eff} may be identified according to the grating equation:

$$n_{\text{eff}} = n_{\text{air}} \sin\theta_{\text{inc}} - \frac{m\lambda}{\Lambda} \tag{4.1}$$

Λ being the grating period, m the diffraction order, λ the incident wavelength, and n_{air} the air refractive index. At normal incidence and cutoff of the grating mode,

the resonance condition reads as $n_{\text{eff}} = m\lambda/\Lambda$. Equation 4.1 provides a simple tool to gain a preliminary understanding of the impact of parameters such as the grating period, material properties, waveguide layers thickness, and angle of incidence on the GMR onset.

4.3 Interband enhancement using GMR gratings

Taking advantage of the studied thin-film architectures, the GMR grating is structured on the front or back side of the thin cell active region, with the different configurations shown in Fig. 4.2. The active region of the cells is made of a stack of InAs/GaAs QD layers with overall thickness of 150 nm (10 QD layers with GaAs interdot layers of 10 nm), embedded within two GaAs layers of 300 nm and 200 nm, respectively. A conventional two-layer ARC composed of SiO_2 and TiO_2 is used. Figure 4.2 (a) shows the planar reference cell used for comparison. Figure 4.2 (b) displays the front side GMR grating approach, where the patterning is performed to the top ARC layer. Figures 4.2 (c) and (d) finally demonstrate the back side GMR approach, where the GMR grating is patterned at the rear surface of the cell, leaving room for the optimization of the cell anti-reflection characteristics through multilayer and/or nanostructured gratings [47, 87] realized on the top surface of the cell.

The study begins with preliminary simulations of the front-side GMR grating structures aimed at enhancing the interband absorbance, which corresponds to the NIR wavelength range. The gratings are cubic shaped, using a half fill factor with respect to the period, and with a constant height of 150 nm. By varying the period, a shift of the resonance peak can be observed as shown in Fig. 4.3. Examining the gain due to the GMR grating for periods of $\Lambda = 0.2 - 0.6\,\mu\text{m}$, shown in Fig. 4.4, the number of narrowband peaks shows an increase that is proportional to the period.

Due to the low index contrast between the SiO_2 material and air, the front-side gratings utilizing do not efficiently couple the light to the active region. This is similar to observations found in Chapter 2 regarding diffraction gratings using low-index materials. Another major disadvantage of using front-side gratings is that the anti-reflection properties are weaker, and a design compromise arises between strong anti-reflection and diffraction. For this reason, the back-side GMR grating configuration shown in Fig. 4.2 (c) is investigated, where the grating is patterned onto the AlInP back surface field layer. The GMR grating is terminated by a conformal planarizing polymer layer and a planar Ag mirror to achieve the highest possible reflectivity while preventing parasitic electrical losses and optical loss in the mirror.

By tuning the period similarly to the initial test for front-side gratings, we observe an increasing number of resonance peaks that is proportional to the period. The achievable gain is significantly higher than that of front-side GMR gratings due

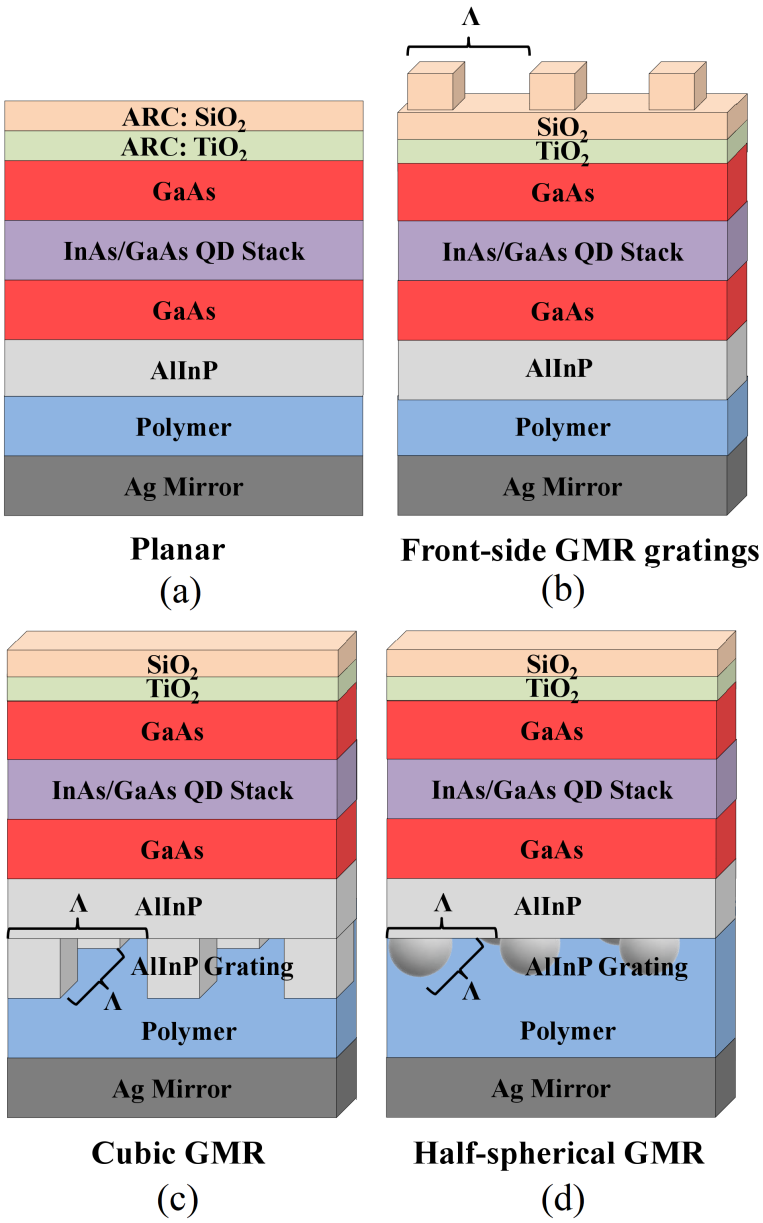

Figure 4.2: The designed IBSCs employing GMR gratings. The layer thicknesses common to all cells are: 110 nm - SiO_2, 55 nm - TiO_2, 300 nm - GaAs, 150 nm - InAs/GaAs QD stack, 200 nm - GaAs, 82 nm - AlInP BSF. (a) Reference planar cell, (b) front-side GMR grating structure, (c) back-side cubic GMR grating structure planarized by a polymer (n=1.55), and (d) back-side half-sphere GMR grating structure with polymer planarization.

to the higher index contrast. Consequently, the use of back-side GMR gratings is

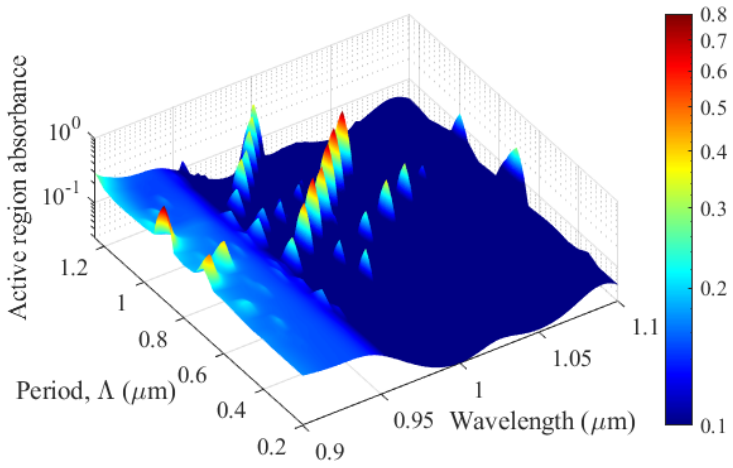

Figure 4.3: The simulated active region absorbance spectra for varying front-side GMR grating periods. A trend is observed showing the peak absorbance shifting in wavelength due to the changing period, as predicted by Equation 4.1.

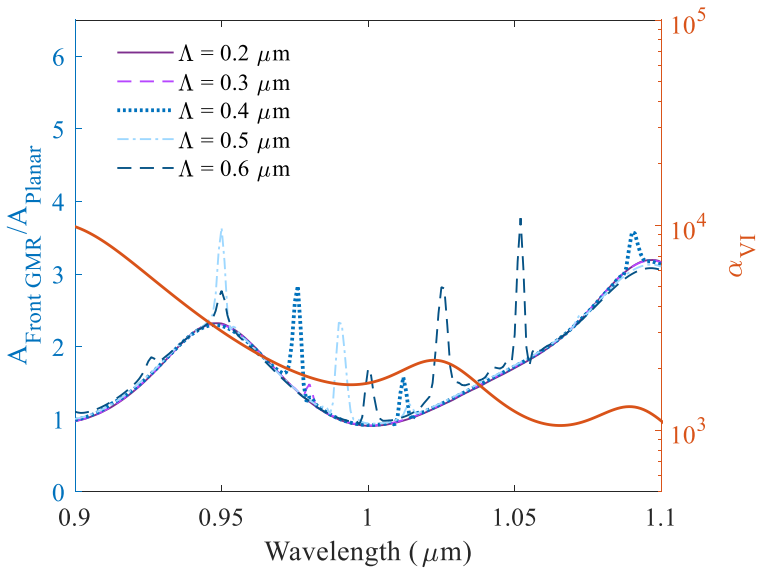

Figure 4.4: The simulated absorbance gain spectrum due to the use of a front-side GMR grating relative to the planar reference cell.

found to be more promising for improved performance. A comparison of front and back side GMR gratings displayed in Fig. 4.6 indicates that back-side GMR gratings significantly outperform their front-side counterpart.

Relative to previously studied diffraction gratings, GMR gratings provide higher

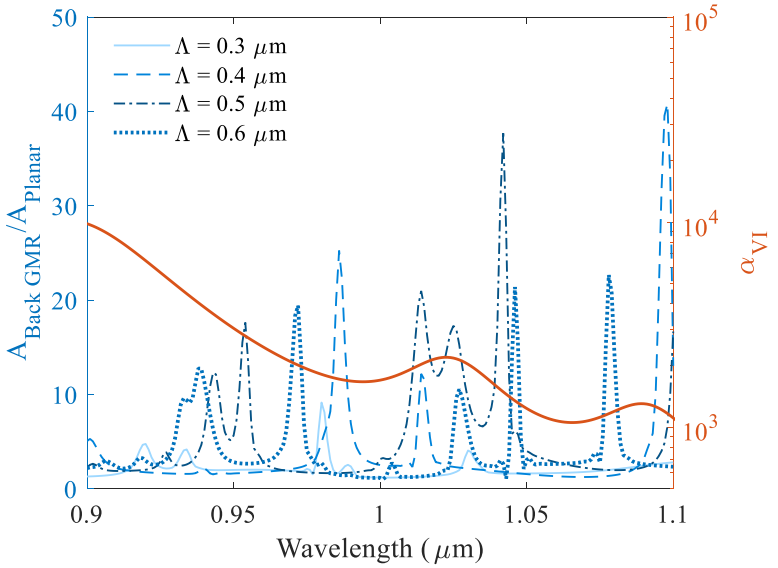

Figure 4.5: The simulated absorbance gain spectrum due to the use of a back-side GMR grating relative to the planar reference cell.

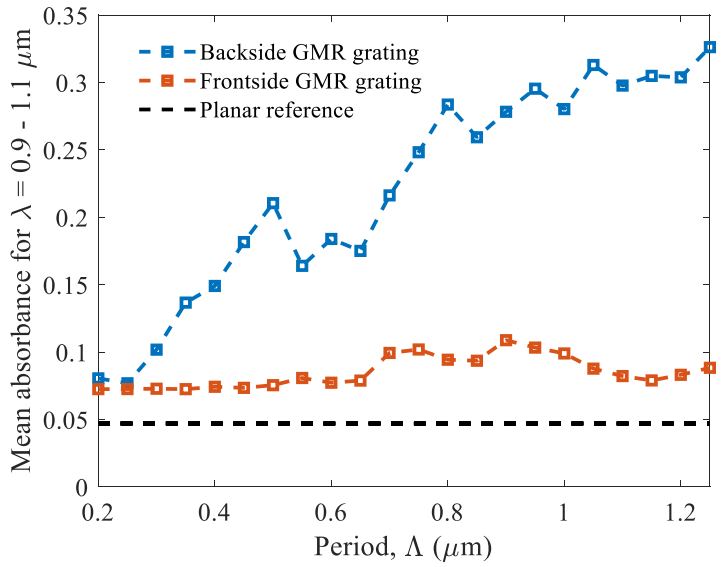

Figure 4.6: A comparison of the achievable mean absorbance vs. grating period is shown for both front and back side GMR configurations. The mean absorbance in the wavelength range corresponding to the NIR interband absorption is used as the metric, with the mean absorbance of planar structure is used as reference.

NIR absorption enhancement that is limited to narrower bands. The GMR method is then more promising for intraband transitions in the MIR range in order to relax the competition between the second photon absorption and thermal escape.

4.4 Intraband enhancement using back-side GMR gratings

The IBSC system for this study consists of a primary VB - IB transition set to 1.13 eV and an IB - CB (second low energy photon) transition to 270 meV. The QD stack is modelled as a homogeneous medium with average complex refractive index in the NIR range as calculated in [31]. For the intraband absorption coefficient (α_{IC}) an average constant value of 200 cm^{-1} at $\lambda_{\mathrm{IC}} = 4.6\,\mu\mathrm{m} \pm 0.3\,\mu\mathrm{m}$ is assumed, which is in line with experimental data of similar QDs [34, 88], while the real part of the refractive index is assumed equal to the GaAs one. Even though the approximation regarding the real refractive index is not strictly correct, the associated error is expected to be marginal. The optical models of the other materials are taken either from the literature [66] or from experimental characterization [47].

Figure 4.7 shows a few examples of resonance conditions predicted according to Equation 4.1 for the waveguiding cell structure in Fig. 4.2(c) and different grating periods, at normal incidence. It is seen that multiple resonances could be sought for in the λ_{IC} range by using grating periods approximately around $3 - 4\,\mu\mathrm{m}$.

The GMR effect is achievable with uni-periodic or bi-periodic grating structures implemented using different geometrical shapes including cubic, pyramidal, or half-spherical gratings. In this study, bi-periodic cubic grating structures were simulated with the RCWA method using RSoft DiffractMOD [69]. TE and TM polarizations were assigned equal weight in the simulations.

Optimization – aimed at maximizing the absorbance in the QD photoactive region at λ_{IC} for normal incidence – was carried out in terms of period and aspect ratio, with a fixed duty cycle of 0.5. The light-trapping effect is quantified by comparing the absorbance in the QD stack at the center wavelength λ_{IC} (A_{GMR}) for the GMR solar cell with the one of an unpatterned solar cell with identical cross-section (A_{planar}) terminated by the Ag mirror. A preliminary optimization carried out in terms of period and aspect ratio (AR =height/period) pointed out a weak dependence of the GMR effect on the grating height in the AR range $0.2 - 0.6$ and an optimum AR value of about 0.32, in line with previous studies [31]. As shown in Fig. 4.8, the absorbance enhancement was also studied considering different periods along the x and y directions to verify the influence of different coupling efficiency to the waveguide polarization modes. As expected, the grating is polarization insensitive for direct incidence, and the maximum enhancement ($\Gamma = A_{\mathrm{GMR}}/A_{\mathrm{planar}} \approx 140$) is found for a symmetric grating with $\Lambda_X = \Lambda_Y = 3.8\,\mu\mathrm{m}$. Two secondary maxima ($\Gamma \approx 90$) are found at $\Lambda_X = \Lambda_Y = 2.27\,\mu\mathrm{m}$ and $\Lambda_X = \Lambda_Y =$

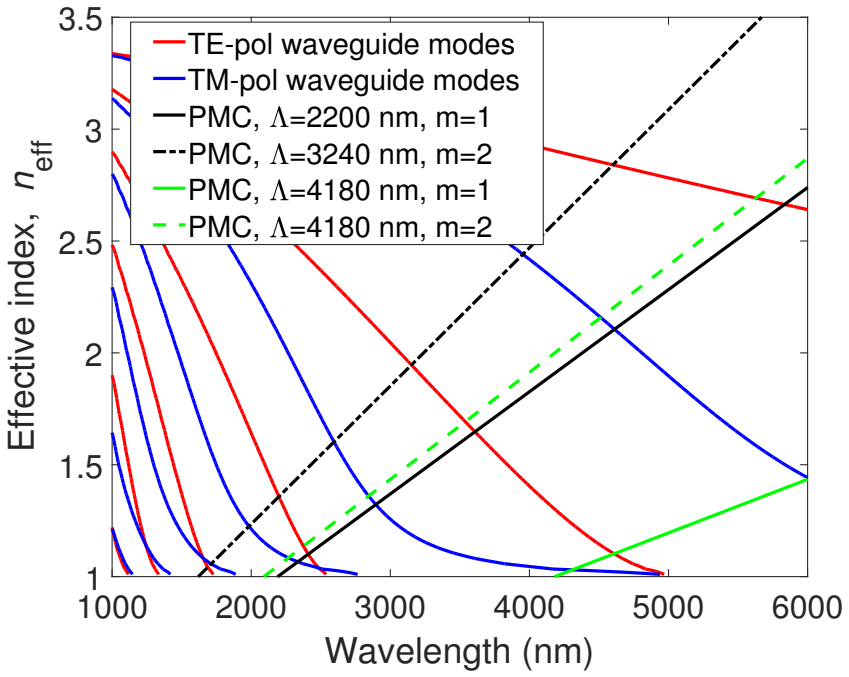

Figure 4.7: Effective refractive index of the guided modes *vs.* wavelength, with phase matching conditions for first (m=1) and second (m=2) order modes of linear grating with different periods.

4.52 μm. According to the analytical calculation reported in Fig. 4.7, it might be argued that the 3.8 μm period induces phase matching with the fundamental mode and possibly further resonances with higher waveguide modes.

4.5 GMR enhancement results

The electric field amplitude and absorbed photon density for the GMR cell and the reference unpatterned cell are shown in Fig. 4.9, for the optimum grating with period $\Lambda = 3.8\,\mu$m and height $h = 1.2\,\mu$m demonstrating significantly higher electric field and enhanced absorption in the QD stack layer.

Figure 4.10(a) compares the spectral absorbance ($A(\lambda)$) in the MIR range for the cubic GMR grating and reference planar solar cells. The GMR cell shows a remarkable increase ($\approx$ 156) of $A(\lambda_{IC})$ with respect to the planar one. Based on a simple Lambert-Beer model of the QD stack, at the peak wavelength λ_{IC}, the effective absorption length of the 150 nm thick QD stack is enhanced by a factor larger than 350. Thus, the QD α_{IC} of 200 cm^{-1} turns into an effective absorption of 7×10^4 cm^{-1}, allowing for the absorption of about 65% of the incident photons. In the 60 nm and 600 nm bands around λ_{IC} the absorbance enhancement is $\approx$ 37

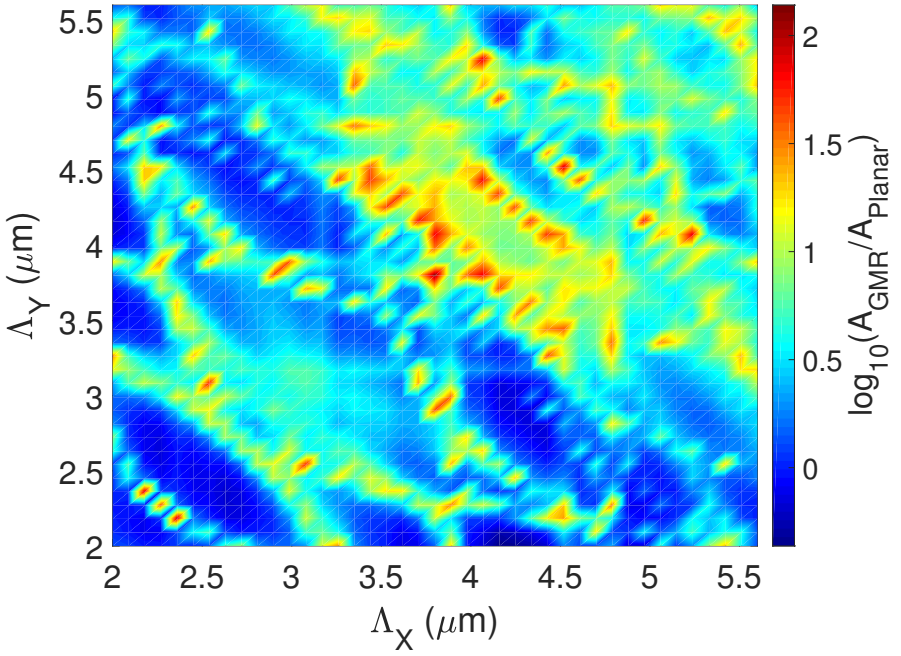

Figure 4.8: Map of the peak absorbance enhancement for cubic grating as a function of grating periods in x and y directions.

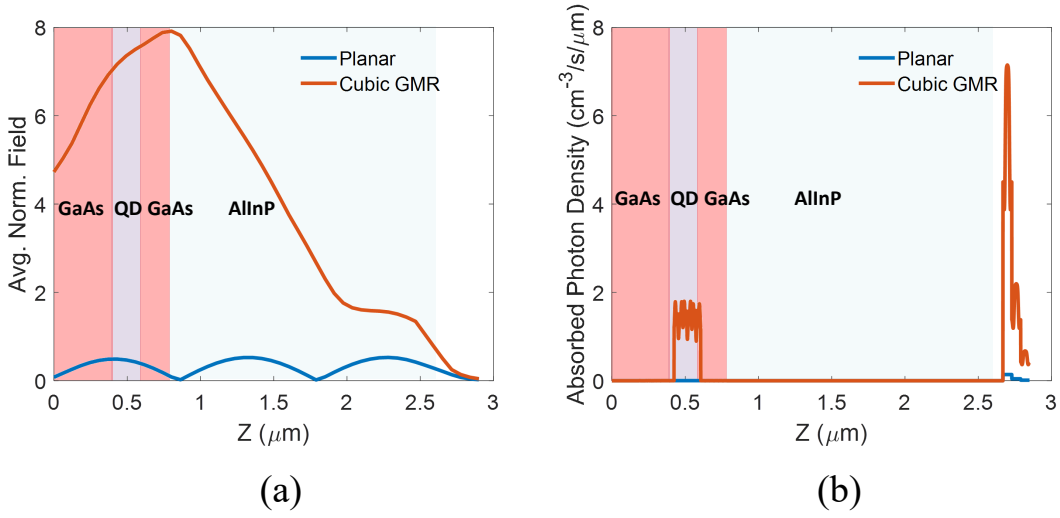

Figure 4.9: (a) Average normalized electric field amplitude and (b) average spatial absorbed photon density at $\lambda_{IC} = 4.6\,\mu$m. The spatial profiles are obtained by averaging across the $x - y$ plane.

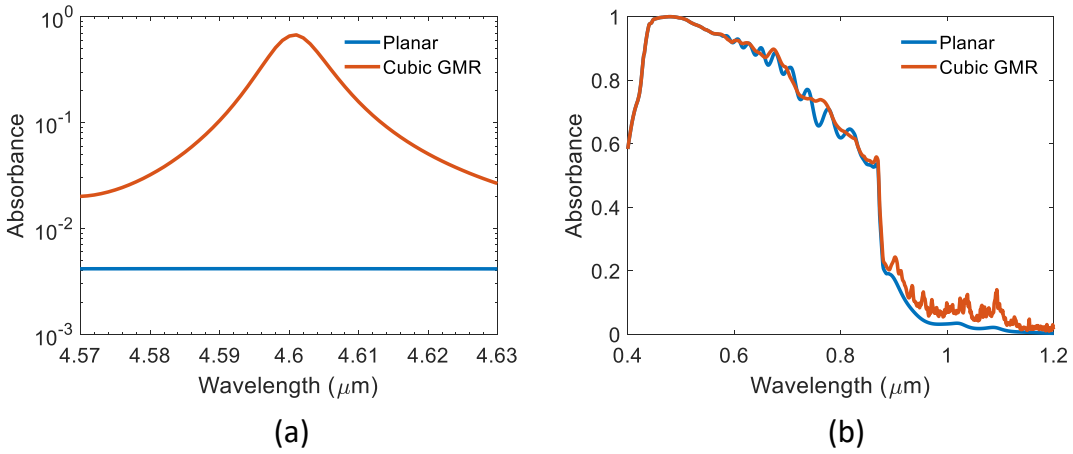

Figure 4.10: Absorbance spectra of the optimum GMR structure and the planar structure in the (a) MIR - QD intraband optical transition - and (b) visible-NIR - GaAs and QD interband transitions - ranges.

and 15, respectively, resulting into an effective α_{IC} of about 10^4 and 4×10^3 cm^{-1}. It is worth noticing that without exploiting light-trapping such high values of the effective α_{IC} could be reached only with QD stack embedding very high in-plane density and/or number of QD layers, well above values achievable with state-of-art QD growth technologies. Finally, Fig. 4.10(b) shows that also in the visible-NIR range the GMR cells demonstrates improved light trapping at wavelengths beyond the GaAs bandgap ($\lambda = 0.895 - 1.2\,\mu$m), leading to QD photocurrent increase from ≈ 0.5 mA/cm^2 in the planar mirrored cell to ≈ 1 mA/cm^2 in the GMR cell.

The angular selectivity of the maximum absorbance enhancement is analyzed in Fig. 4.11. For the sake of comparison, the behavior of a half-spherical GMR grating is investigated, for a sphere radius of $\Lambda/4$ and period ($\Lambda = 5.6\mu$m) optimized to attain the highest possible average absorbance enhancement over the $0^o - 90^o$ range. As expected, light-trapping enhancement above the Lambertian limit implies significant angular selectivity. However, for angles of incidence (θ) up to 9^o, corresponding to a concentration factor slightly higher than 1000 sun ($46000 \times \sin^2(\theta)$), the absorbance enhancement is still high (48) and close to the Lambertian limit. The results compare favorably with the previous studies on the GMR effects in silicon solar cells and QDIPs. In [28] three-fold absorbance enhancement was predicted over a 120 nm bandwidth next to the silicon gap and $\pm 40^o$ angle of incidence, while a 30% integrated absorbance enhancement in the $450 - 750$ nm range was experimentally demonstrated for amorphous silicon cells in [29]. Finally, the resonant-cavity enhanced QDIP in [86] showed absorbance enhancement of 20 at the target wavelength of 8 μm for $\pm 10^o$ angle of incidence.

The IB energy and optical properties depend on several QD parameters such as size and materials. Moreover, α_{IC} is difficult to accurately characterize. Finally, the

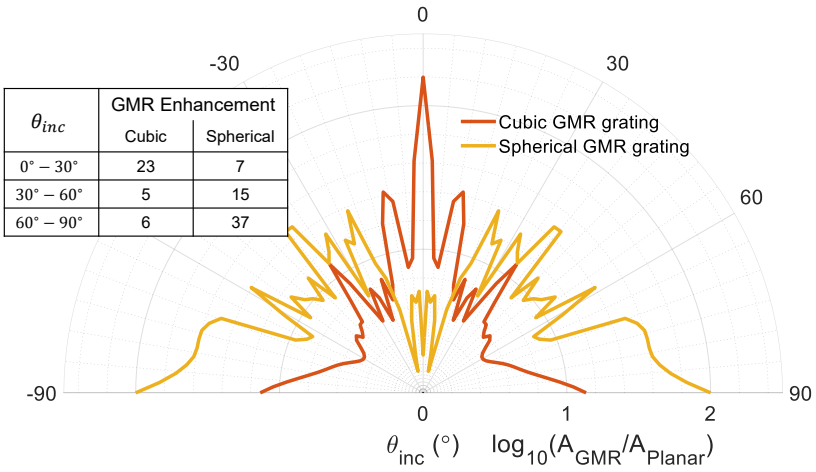

θ_{inc}	GMR Enhancement	
	Cubic	Spherical
0° – 30°	23	7
30° – 60°	5	15
60° – 90°	6	37

Figure 4.11: GMR Gain vs. angle of incidence θ_{inc} for the cubic ($\Lambda = 3.8\,\mu$m) and the half-spherical grating ($\Lambda = 5.6\,\mu$m) at wavelength $\lambda_{\text{IC}} = 4.6\,\mu$m.

full optimization of the IBSC operation implies a strict relation between interband and intraband absorption coefficients and the E_{IC} transition energy [36]. Therefore, it is useful to assess the scaling of the optimum grating parameters and of the obtainable absorbance enhancement with respect to the intraband absorption strength and energy. Figure 4.12(a) reports the GMR enhancement at the peak wavelength as a function of the QD intraband optical coefficient showing significant absorbance enhancement (≈ 50) up to $\alpha_{\text{IC}} = 1000$ cm^{-1}. In Fig. 4.12(b), an analysis is presented that examines how the optimum grating period and aspect ration scale as E_{IC} varies from 270 meV to 600 meV, a range representative of the MIR range wavelengths covered by intraband and intersubband transitions in type-I InAs/GaAs and type-II GaAs/GaSb QDs. A weak sensitivity to the aspect ratio is also observed. As anticipated from the analytical model in Fig. 4.1 decreasing the grating period causes a blue-shift of the resonance wavelengths. In line with this, RCWA simulation results show a decreasing nearly linear trend of the optimum period with E_{IC}. Deviations from a perfect linear behavior are caused by slight changes also of the absorbance of the planar reference. With the optimized period, the GMR enhancement is always found larger than 100 except for the point at highest energy (E_{IC}) where it is limited to about 55, owing to the relatively higher absorbance found in the planar structure. Finally, from the approximated linear dependence of Λ *vs.* E_{IC} the sensitivity of the proposed design to fabrication tolerances can be estimated. From the extracted slope $\Delta\Lambda/\Delta E_{\text{IC}} \approx -3.7$, a maximum shift of $\pm$ 300 nm of the peak absorbance wavelength with respect to the target one ($\lambda_{\text{IC}} = 4.6\mu$m) requires a maximum variation of the period of about $\pm$65 nm, compatible with grating fabrication tolerances.

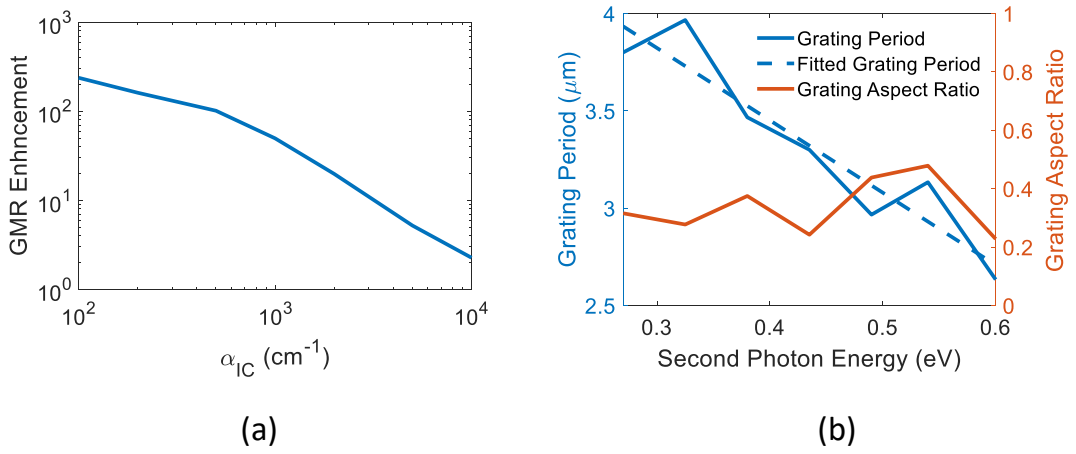

Figure 4.12: (a) GMR enhancement *vs.* QD intraband optical absorption coefficient (α_{IC}) at the peak wavelength. (b) Estimated optimum grating period and aspect ratio (height/period) as a function of the second photon absorption energy (E_{IC}). All the optimum points except the one at highest energy (see text) identify GMR enhancement larger than 100 at E_{IC}.

4.6 Conclusions

Overcoming the efficiency limitation of single-gap solar cells motivates the investigation of IB solar cells, which promise high current and high voltage through the absorption of two sub-bandgap photons. It has been shown that optical path elongation and resonant field enhancement for lower energy photons are made possible using GMR gratings.

The GMR gratings can be employed for interband or intraband transitions but are more useful for the enhancement of the second photon absorption in the MIR-range for direct and oblique incidence angles. Design guidelines are presented for ranges of energy and strength of the second-photon absorption representative of III-V QDs such as InAs/GaAs and GaSb/GaAs systems. The results demonstrate that the GMR concept is suitable for a wide class of QD-IBSCs. An added benefit of the proposed GMR design is the diffraction at NIR wavelengths which also strengthens the primary photon absorption. These effects will result in improved short circuit current density and IB photogeneration rate.

The GMR effect observed from using periodic gratings can potentially be combined with the diffraction effects demonstrated in Chapters 2 and 3. The GMR enhancement in the MIR range can theoretically be realized using different grating shapes with periods that are multiples of the NIR wavelength range. This would enable both GMR at the longer wavelengths as well as diffraction at the shorter ones, in order to address the low absorption in both regions. This could be promising

to IBSCs where both the first and second photon transitions would be simultaneously enhanced. Additionally, multi-resonant enhancement has been studied in [89], where a series of narrowband enhancement peaks can be designed to overlap and result in a wideband absorbance enhancement. Multi-resonant enhancement has been realized for ultra-thin GaAs cells, but can be extended to IBSC systems.

The structures and approaches investigated in this Chapter may also find important application in intraband quantum-dot infrared detectors. Angle-selectivity has been discussed in view of applications in concentrator photovoltaic systems and infrared imaging systems.

Chapter 5

Efficient modelling of thin-film solar cells with periodically textured surfaces

5.1 Introduction

The active regions of the studied thin-film cells range from hundreds of nanometers to a few micrometers, which requires that the previously mentioned back-side diffraction gratings are implemented by wavelength-scale optical structures. The computer-aided design of such structures is a rather challenging task, since their adequate optical modelling requires 2D or even 3D electromagnetic (EM) full-wave simulations. The EM simulation time is particularly critical in view of performing self-consistent electro-optical simulations aimed at describing the entire photovoltaic process, as demonstrated in Fig. 5.1. This allows us to account for local interaction of carriers and for the strong carrier density dependence of optical properties in nanostructured semiconductors. In addition, it could enable the incorporation of specific mechanisms such as the photon recycling effect in cells working close to the radiative limit, where isotropically emitted photons may be reabsorbed [91, 92, 93].

With the aim of developing a comprehensive simulation framework feasible for the computer-aided design and optimization of light-trapping enhanced solar cells, this Chapter presents an efficient simulation strategy for patterned thin-film solar cells. The optical simulation of the periodic structure, which has been identified as a bottleneck from the computational standpoint, is wave-optics simulated once

---

The work presented in this Chapter is based on "Efficient multiphysics modeling of thin-film solar cells with periodically textured surfaces", F. Elsehrawy, A. Tibaldi, and F. Cappelluti [90].

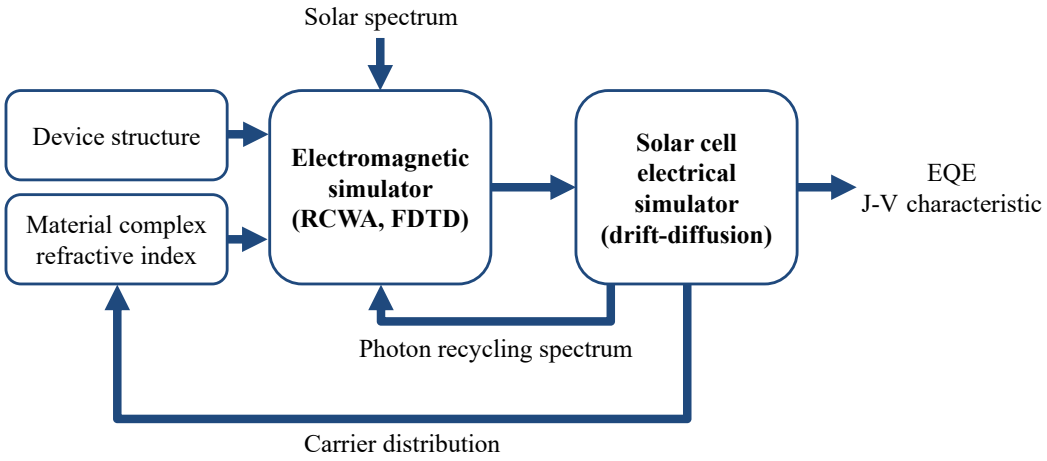

Figure 5.1: The interdependence of electrical and electromagnetic simulations is shown, emphasizing the importance of self-consistent simulations.

by RCWA and a multimodal scattering matrix equivalent description is derived. The remaining solar cell layers, where most of the electro-opto interactions take place, are described by a numerically-stable approach based on the scattering matrix formalism [94, 95], accounting for the multimode interaction with the grating. The optical simulation of the whole structure is then obtained by cascading the scattering matrix of the grating and the one of the planar multilayer region. The approach is validated through comparisons with RCWA simulations of the full solar cell structure. In addition, a method for extracting the grating scattering matrix from the typical output of commercial RCWA software is presented.

Other implementations of computationally efficient optical simulations have been previously studied in the literature. One method proposed in [96, 97] relies on a coupled modelling approach, where the thin-film multilayer structures are treated differently than thick macroscopic layers. This approach enables using rigorous wave-optics electromagnetic simulations for nanotextured interfaces in order to accurately characterize their scattering behavior, and use statistical ray-optics methods such as ray tracing for thick layers or macroscopic features. The combined ray-optics/wave-optics model is useful for modelling wafer-based cells employing periodic texturing, where cells much thicker than the coherence length of sunlight require different simulation methods relative to microscopic textured surfaces that require full-wave methods [78]. Another work demonstrates an efficient optical simulation method, where the textured light trapping structures are modelled using an effective scattering matrix and then incorporated as a boundary condition [34]. The work presented in this Chapter finds novelty in the coupling of optical and electric simulations, while utilizing the computationally efficient full-wave electromagnetic

simulation approach.

5.2 Optical simulation strategy

The geometry of the simulated optical problem is the stack of dielectric layers lying on the patterned diffraction grating sketched in Fig. 5.2. This structure lends itself to a *divide and conquer* computer-aided design strategy. In fact, from the optical modelling standpoint, the critical point lies in the grating, whose purpose is to stimulate light trapping. However, all the absorption processes occur in the stratified dielectric structure, which can be modelled separately.

The grating electromagnetic analysis can be reduced to a waveguide scattering problem consisting of a unit cell including a single period with phase-shift wall pseudoperiodic boundary conditions. In this view, solar light is conveniently described as a superposition of plane-waves characterized by incidence angle θ_{inc} and wavelength λ, allowing the computation of the waveguide phase shift ϕ as:

$$\phi = k_{x0}\Lambda = k_0 n_{\text{in}} \Lambda \sin\theta_{inc} = \frac{2\pi}{\lambda} n_{\text{in}} \Lambda \sin\theta_{inc}. \tag{5.1}$$

where n_{in} is the refractive index of the semi-infinite medium where the incident field is defined. In this work the grating is assumed to be translationally invariant with respect to y, leading to a 2D problem on the (z, x) planes. Still, this is sufficient to demonstrate the effectiveness of the simulation strategy, which can be extended to 3D gratings in a straightforward fashion.

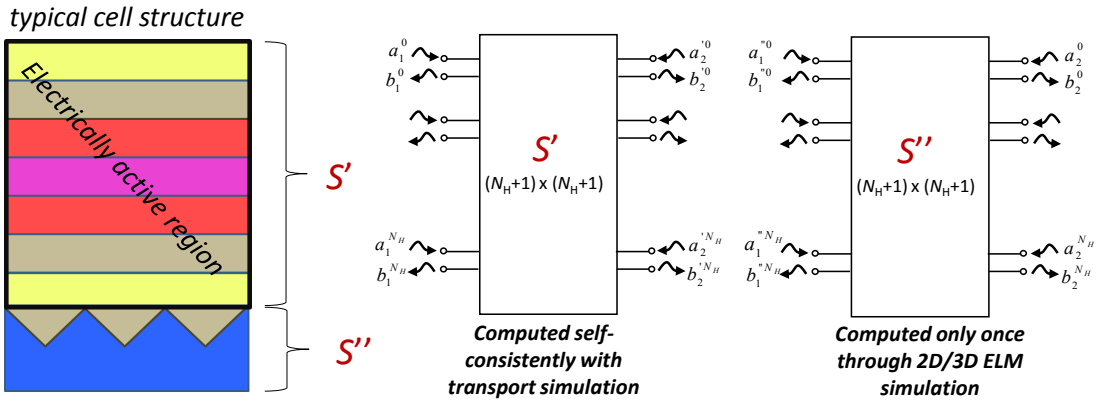

Figure 5.2: Left: sketch of a typical thin-film solar cell structure; the electrically-active region and the patterning aimed at fostering light trapping are emphasized. Right: schematic representation of the scattering matrices describing the main sub-blocks involved in the optical simulation.

For GaAs solar cell applications, the grating period Λ is approximately $3\,\mu$m, so even the unit cell is electrically large. In this context, fully-numerical approaches, such as the finite difference time domain (FDTD) method, are highly computationally-expensive. The RCWA provides a computationally affordable technique that overcomes the approximations of diffraction theory. In this case, the modes of the phase-shift wall waveguide modes are evaluated by expanding the electromagnetic field components as a superposition of Floquet modes identified by their transverse wavenumber:

$$k_{xm} = k_{x0} + \frac{2\pi m}{\Lambda}, \tag{5.2}$$

being m the diffracted order index. The grating simulations adopted in this work are obtained by means of a commercial RCWA solver. Separating the stack and grating simulations allows performing the time-consuming grating simulations just once and obtaining the generalized reflection coefficient seen from the grating input surface and treating it as the stack boundary condition.

The stratified dielectric structure describing the stack of absorbing solar cell layers can be assimilated to a transmission line circuit [98], where the modal transmission lines are coupled only on the grating surface. More in detail, for each i-th region with corresponding refractive index n_i, several transmission lines are defined, one for each m-th Floquet mode, which are characterized by the longitudinal propagation constant:

$$k_{z,mi} = \sqrt{k_0^2 n_i^2 - k_{xm}^2} \tag{5.3}$$

and by the characteristic impedances for TE ($E_z = 0$) and TM ($H_z = 0$) polarizations:

$$Z_{\infty,mi}^{\mathrm{TE}} = \frac{k_0}{k_{z,mi}} Z_0, \qquad Z_{\infty,mi}^{\mathrm{TM}} = \frac{k_{z,mi}}{k_0} Z_0, \tag{5.4}$$

where $Z_0 = \sqrt{\mu_0/\varepsilon_0}$ is the free-space impedance. Propagation in the stratified structure is described in terms of a scattering matrix formalism, which guarantees higher numerical stability than transfer-matrix methods in presence of evanescent modes [94]. The scattering matrix of a transmission line with length t_i is:

$$\mathbf{D} = \mathrm{diag}\{\mathrm{e}^{-\mathrm{j}k_{z,mi}t_i}\}, \tag{5.5}$$

while the 2×2 scattering matrix $\overline{\mathbf{S}}_m$ for the m-th Floquet mode at the interface between its left (1) and right (2) media is:

$$\overline{S}_{m,11} = \frac{Z_{m,2} - Z_{m,1}}{Z_{m,2} + Z_{m,1}}, \quad \overline{S}_{m,21} = \frac{2\sqrt{Z_{m,1} Z_{m,2}}}{Z_{m,1} + Z_{m,2}}, \quad \overline{S}_{m,12} = \overline{S}_{m,21}, \quad \overline{S}_{m,22} = -\overline{S}_{m,11}. \tag{5.6}$$

Finally, given two matrices $\overline{\mathbf{S}}'$, $\overline{\mathbf{S}}''$, their cascade can be computed as:

$$\begin{aligned}
\mathbf{S}_{11} &= \overline{\mathbf{S}}'_{11} + \overline{\mathbf{S}}'_{12}\overline{\mathbf{S}}''_{11}\left(\mathbf{I} - \overline{\mathbf{S}}'_{22}\overline{\mathbf{S}}''_{11}\right)^{-1}\overline{\mathbf{S}}'_{21} \\
\mathbf{S}_{12} &= \overline{\mathbf{S}}'_{12}\left(\mathbf{I} - \overline{\mathbf{S}}''_{11}\overline{\mathbf{S}}'_{22}\right)^{-1}\overline{\mathbf{S}}''_{12} \\
\mathbf{S}_{21} &= \overline{\mathbf{S}}''_{21}\left(\mathbf{I} - \overline{\mathbf{S}}'_{22}\overline{\mathbf{S}}''_{11}\right)^{-1}\overline{\mathbf{S}}'_{21} \\
\mathbf{S}_{22} &= \overline{\mathbf{S}}''_{22} + \overline{\mathbf{S}}''_{21}\left(\mathbf{I} - \overline{\mathbf{S}}'_{22}\overline{\mathbf{S}}''_{11}\right)^{-1}\overline{\mathbf{S}}'_{22}\overline{\mathbf{S}}''_{12}.
\end{aligned} \tag{5.7}$$

By applying eqs. (5.5)÷(5.7) to solve the transmission line circuit for each z section of the solar cell, it is possible to evaluate the current and voltage standing wave patterns $V_m(z)$ and $I_m(z)$ for each m-th mode. The electromagnetic field can be finally computed as:

$$\begin{aligned}
\mathbf{E}(x,z) &= \sum_m \frac{V_m(z)}{\sqrt{\Lambda}} \mathrm{e}^{-\mathrm{j}k_{xm}x} \\
\mathbf{H}(x,z) &= \sum_m \frac{I_m(z)}{\sqrt{\Lambda}} \mathrm{e}^{-\mathrm{j}k_{xm}x}.
\end{aligned} \tag{5.8}$$

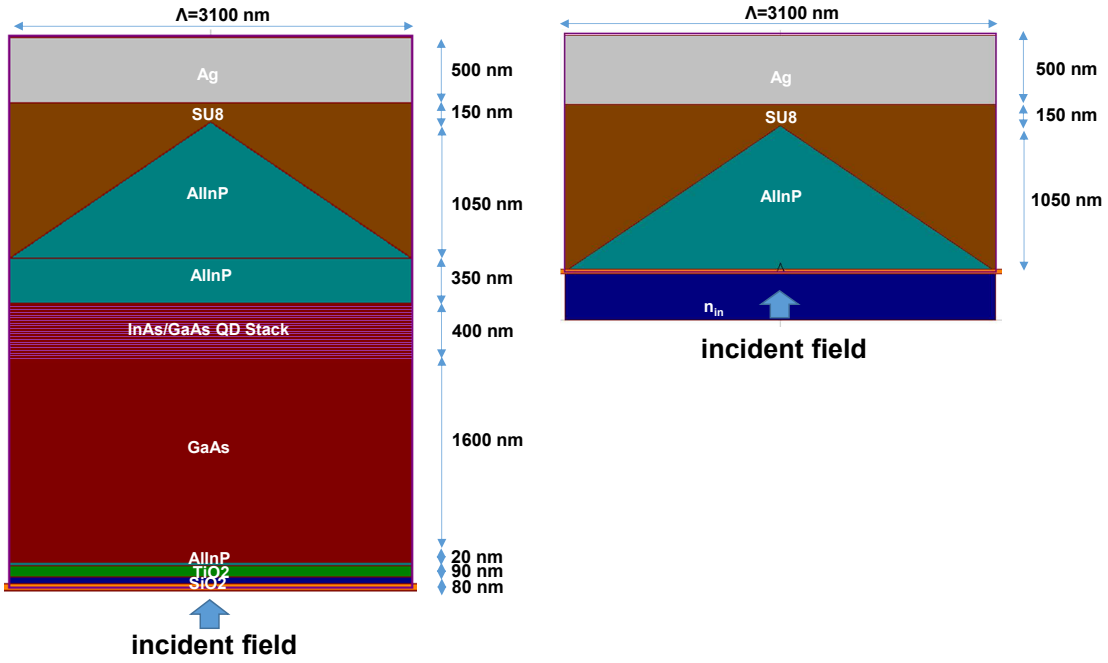

Figure 5.3: Left: detailed geometry of the light trapping-enhanced QD solar cell. Right: detail of the texturing; note that the input refractive index of such a grating is not necessarily coincident with the adjacent layer of the stratification.

5.3 Grating model integration

The simulation framework has been applied to a typical solar cell structure, adapted from the optimized QDSCs in the previous sections. The QDSC structures with diffraction gratings in this study are demonstrated in Fig. 5.3. The cell structure includes the same QD stack and implements a diffraction grating with aspect ratio within the optimum range. The grating dimensions are optimized based on previous work[31] where a period-to-height aspect ratio of $0.32-0.38$ is found to provide the highest light trapping within the active region for an InAs/GaAs QD solar cell. Accordingly, the grating dimensions selected for this study are a period of 3100 nm and a height of 1050 nm, which would result in an effective optical path length enhancement of up to 13 times with respect to a single-pass reference cell.

The optical simulation of the periodic structure is performed on the RSoft DiffractMOD package in order to characterize the response in terms of the structure's wavelength-dependent multimode scattering matrix [69]. The RCWA solver included in DiffractMOD allows great flexibility in the geometry description and could be used for 3D simulations in future studies. The DiffractMOD tool provides as output the complex field coefficients, which are used to construct the scattering matrix representing the grating. The simulations are performed at varying angles of incidence and wavelengths in order to extract the coefficients for a wide spectrum. For each wavelength, the complex reflection coefficients are computed for each excited mode by using angle of incidence corresponding to the relevant mode. The angles $\theta_{inc,m}$ depend on both the m-th incident harmonic to be extracted to build the scattering matrix and the operation wavelength λ. The different incidence angles $\theta_{inc,m}$ are then chosen according to:

$$\theta_{inc,m} = \text{atan}\left(\frac{k_{xm}}{k_{z,m,\text{in}}}\right), \tag{5.9}$$

where k_{xm} is that defined in (5.2) and $k_{z,m,\text{in}}$ is the propagation constant in the input medium n_{in} used in the DiffractMOD grating simulation.

The choice of n_{in} is completely arbitrary, as it defines the reference impedance with respect to which the grating scattering matrix elements are computed. To properly take it into account, it is sufficient to insert, at the end of the stacked layers, a fictional zero-thickness layer with refractive index n_{in}, matching the solar cell and grating matrices. The simulation accuracy increases with the number of harmonics propagated through the stacked layers, *i.e.,* the dimension of the generalized scattering matrix. However, a present limitation of DiffractMOD is that it allows to extract the complex field coefficients only for propagating modes; in this view, it is appropriate to choose a high n_{in} value, so as to increase the number of propagating modes.

DiffractMOD produces the complex reflection and transmission coefficients in the transverse plane (normal to the primary direction). For 2D simulations of a

uniperiodic grating, the E_y field component is associated with TE mode incidence, for propagation in the z direction. The reflection coefficients are then organized in a scattering matrix format with size corresponding to the number of propagating modes as:

$$S_{11}=\begin{bmatrix} S_{11(0,0)} & S_{11(0,-1)} & S_{11(0,1)} & S_{11(0,-2)} & S_{11(0,2)} & \cdots & S_{11(0,-m)} & S_{11(0,m)} \\ S_{11(-1,0)} & S_{11(-1,-1)} & S_{11(-1,1)} & S_{11(-1,-2)} & S_{11(-1,2)} & \cdots & S_{11(-1,-m)} & S_{11(-1,m)} \\ S_{11(1,0)} & S_{11(1,-1)} & S_{11(1,1)} & S_{11(1,-2)} & S_{11(1,2)} & \cdots & S_{11(1,-m)} & S_{11(1,m)} \\ S_{11(-2,0)} & S_{11(-2,-1)} & S_{11(-2,1)} & S_{11(-2,-2)} & S_{11(-2,2)} & \cdots & S_{11(-2,-m)} & S_{11(-2,m)} \\ S_{11(2,0)} & S_{11(2,-1)} & S_{11(2,1)} & S_{11(2,-2)} & S_{11(2,2)} & \cdots & S_{11(2,-m)} & S_{11(2,m)} \\ \vdots & \vdots & \vdots & \vdots & \vdots & \ddots & \vdots & \vdots \\ S_{11(-m,0)} & S_{11(-m,-1)} & S_{11(-m,1)} & S_{11(-m,-2)} & S_{11(-m,2)} & \cdots & S_{11(-m,-m)} & S_{11(-m,m)} \\ S_{11(m,0)} & S_{11(m,-1)} & S_{11(m,1)} & S_{11(m,-2)} & S_{11(m,2)} & \cdots & S_{11(m,-m)} & S_{11(m,m)} \end{bmatrix} \tag{5.10}$$

This results in a matrix of $2m + 1$-by-$2m + 1$ elements for m harmonics. The final matrix will be a combined block matrix comprising both TE and TM mode reflection coefficients, with the elements corresponding to non-propagating modes are set to zero. The extracted scattering matrix can then be used to compute the amplitude and phase information about the plane wave for a multilayer solar cell structure.

5.4 Model validation

Preliminary RCWA 2D simulations have been performed by means of an in-house developed tool [99], which helped to correctly define the **S** matrix obtained from DiffractMOD. In the simulations, the maximum diffracted order considered for (5.9) is $m_{\max} = 24$ (leading to a 49×49 grating scattering matrix for each polarization), which is adequate to achieve good accuracy in the GaAs wavelength range. These simulations also allowed for a cross-validation of the two RCWA codes, which is presented in Fig. 5.4.

The next step of validation is performed by using the grating scattering matrix to simulate the complete solar cell. The simulation results are shown in Fig. 5.5, which reports the electric field maps of the complete cell obtained with DiffractMOD (left) and with our approach (right) at TE mode incidence. The field maps are presented for three wavelengths belonging to different solar cell operation regimes: strong GaAs absorption (0.7 μm, top), where the texturing effect is negligible; GaAs band-edge (0.85 μm, center), where the grating effect can be observed; QD absorption region (1 μm, bottom), where light trapping is particularly effective.

A more quantitative comparison can be obtained by examining the cuts of the electric field maps a $x = 0$, as presented in Fig. 5.6, where strong agreement between the two simulation frameworks is observed. The field amplitudes are normalized.

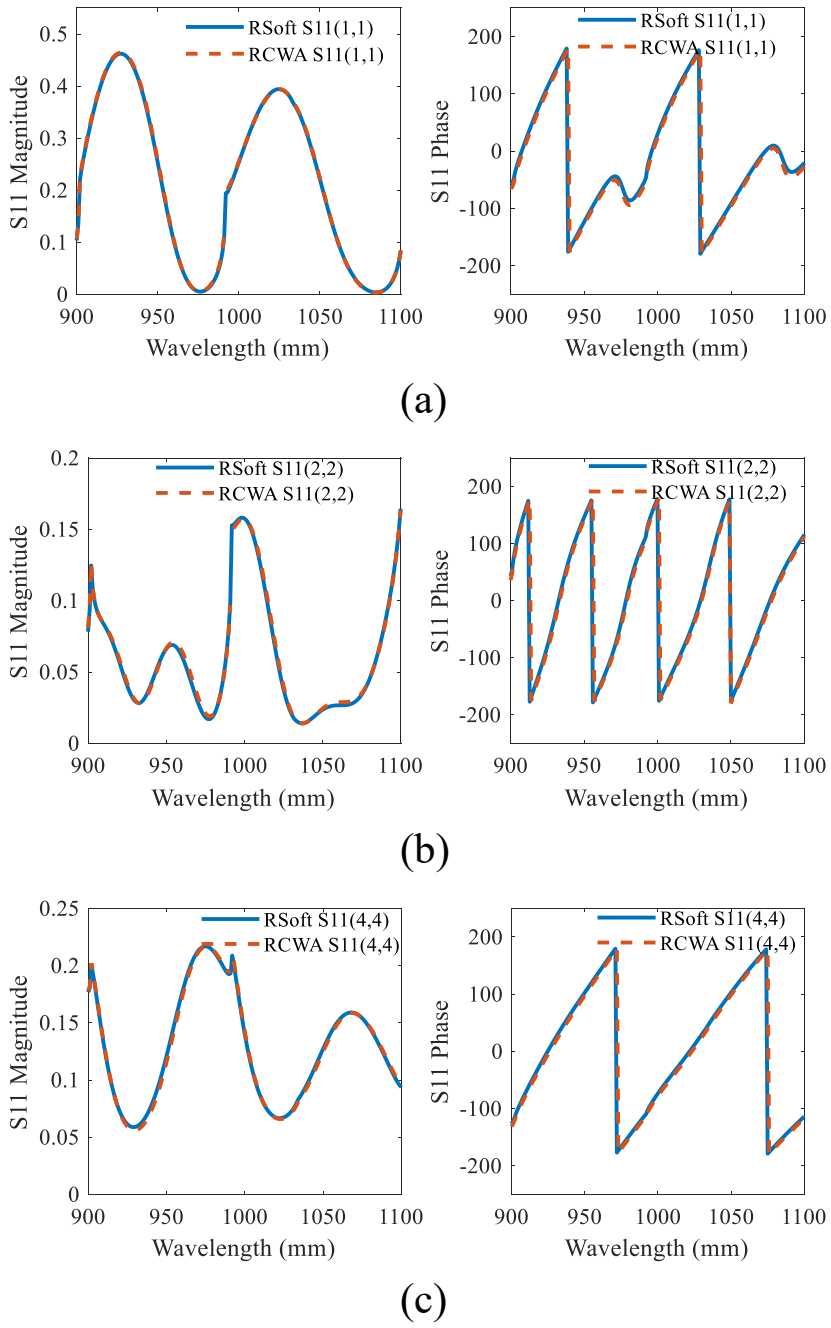

Figure 5.4: Components of the grating scattering matrix extracted from the results of the RSoft DiffractMOD simulation and as calculated by the in-house RCWA solver. The comparison is performed at $\lambda = 900 - 1000$ nm for the reflection coefficient S_{11} of mode $m = 0$ (a), mode $m = 1$ (b), and mode $m = 2$. TE mode polarization is used for the comparison.

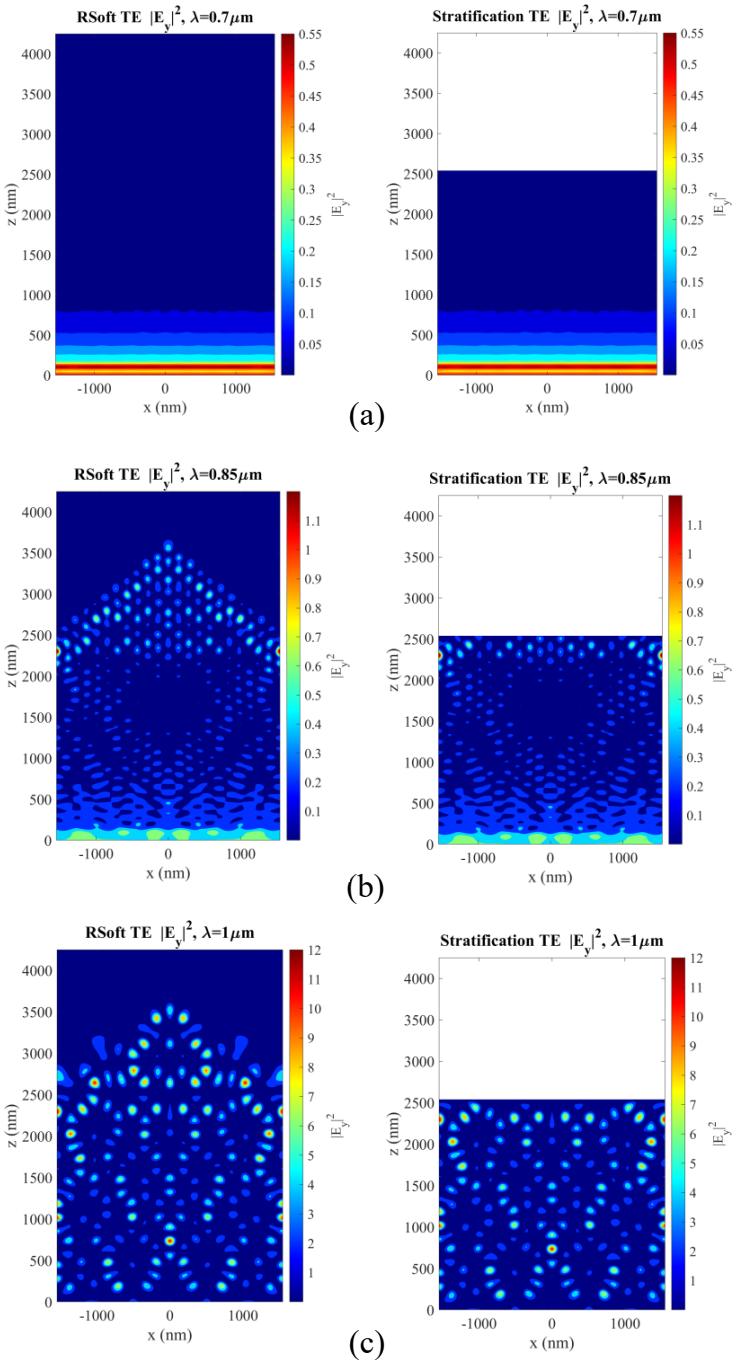

Figure 5.5: Comparison between the electric field maps (E_y component) for TE mode incidence of the examined solar cell as obtained by 2D RSoft DiffractMOD simulations of the entire structure and by the cascade of the scattering matrixes. The maps are calculated at different wavelengths: (a) $\lambda = 0.7\,\mu$m, (b) $\lambda = 0.85\,\mu$m, (c) $\lambda = 1\,\mu$m.

The multilayer simulations using the stratification method can also be used to compute the reflectance of a solar cell over a spectrum. This can be useful in view of ARC optimization. For the solar cell under study, the direct reflectance has been computed and compared with the reference result from DiffractMOD, with the comparison shown in Fig. 5.7 demonstrating strong matching with the reference. The spectrum indicates absorption by the GaAs in the range up to the GaAs band-edge, followed by increased direct reflectance for longer wavelengths.

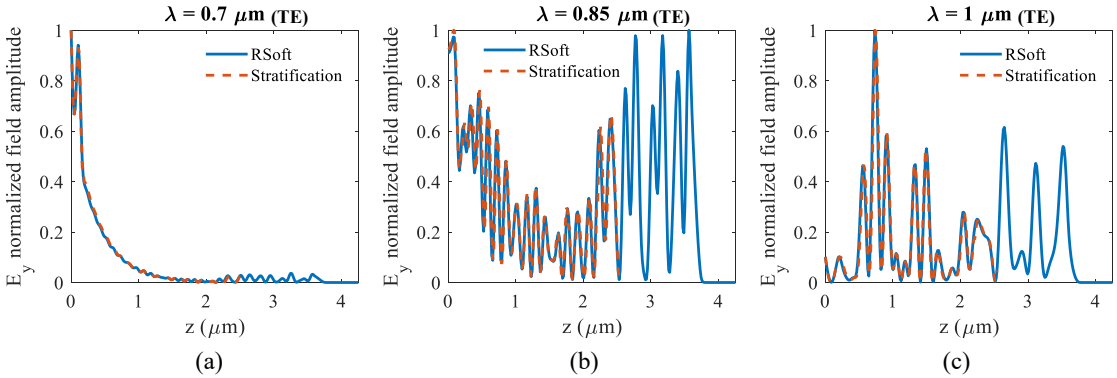

Figure 5.6: Cutline at $x = 0$ of the E_y field component maps in Fig. 5.5, demonstrating the strong matching between the full RCWA simulation and the proposed Stratification method at (a) $\lambda = 0.7\,\mu$m, (b) $\lambda = 0.85\,\mu$m, and (c) $\lambda = 1\,\mu$m, for TE polarization.

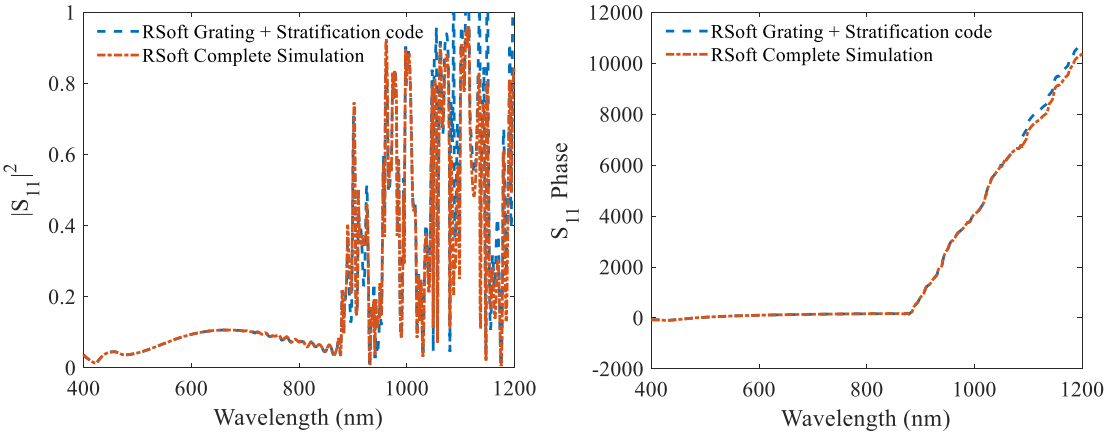

Figure 5.7: Comparison of the $S_{11(0,0)}$ direct reflectance for TE polarization over a wide wavelength range for the complete solar cell simulated using the commercial simulator RSoft and using the efficient method where the grating reflection coefficients are used as input to the in-house developed stratification code.

5.5 Model implementation

After validating the model, the implementation of the studied methodology was done for a test case using the same solar cell structure. The implementation utilizes the extracted grating scattering matrix to enable an efficient full electromagnetic simulation of the solar cell, which is coupled to an electric simulation of the active region comprising a QD stack.

First, the electrical field maps and the absorption coefficients of the different materials in the multilayer structure are used to compute the absorbed photon density G_{ph} for a given volume V as:

$$G_{ph}^{V}(\lambda) = \int_{V} n\alpha|\mathrm{E}|^2 dV(\lambda) SPF(\lambda). \tag{5.11}$$

The spatial photogeneration rate was computed for the studied QDSC structure assuming a unity quantum yield (where each absorbed photon generates an electron/hole pair), as shown in Fig. 5.8 for λ=0.7 μm, 0.85 μm, and 1.2 μm. At lower wavelengths (λ<0.9 μm), the photon absorption is primarily in the GaAs layers while at $\lambda = 1\,\mu$m, the lower energy photons are absorbed in the QD equivalent layer only while the GaAs layers are optically transparent.

Finally, the photogeneration rate is used as an input to electric transport solvers to compute the carrier concentrations within the solar cell. The thin-film QDSC with a grating was used as the test structure for the study. The electrical transport simulation is performed using an in-house developed code that implements a multi-scale model based on a semi-classical transport-Poisson framework, which accounts for the QD dynamics [100]. The electro-optical simulation provides the EQE, which can be deconstructed as the product of the absorbance and the IQE. Figure 5.9 shows the EQE, IQE, and absorbance results obtained for the studied structure using the multilayer solver, as well as the reference active region absorbance obtained using the commercial electromagnetic solver RSoft DiffractMOD.

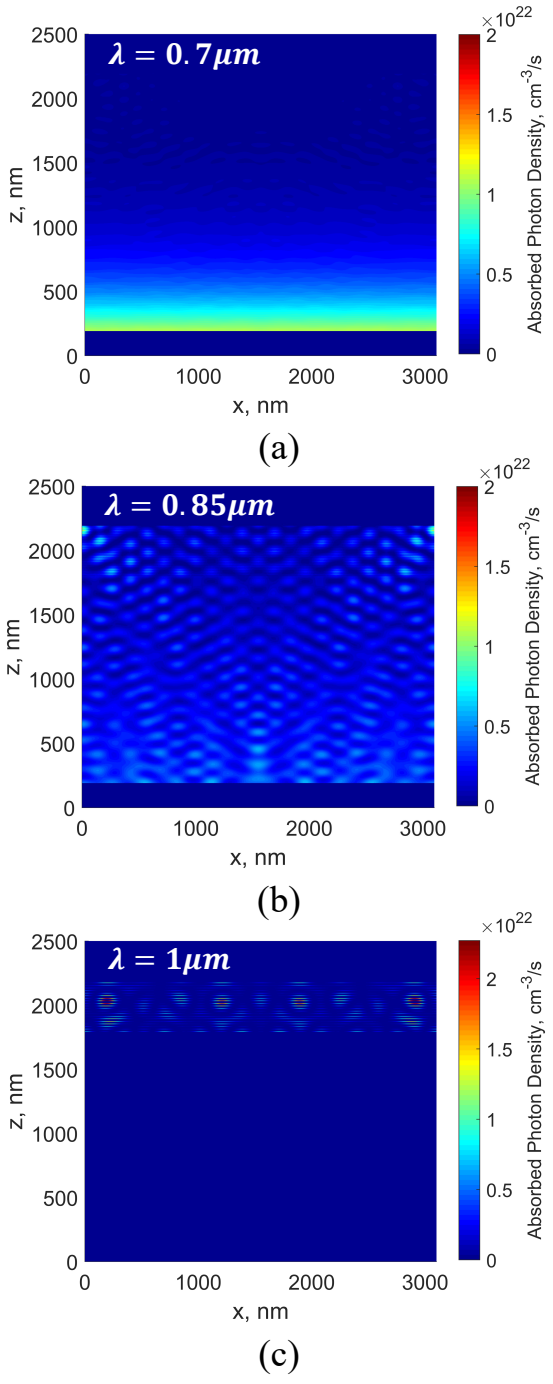

Figure 5.8: The absorbed photon density (G_{ph}) of the examined structure as obtained by the cascade of the scattering matrixes, terminated with the uni-periodic back grating. The maps are calculated at different wavelengths: (a) $\lambda = 0.7\,\mu$m, (b) $\lambda = 0.85\,\mu$m, and (c) $\lambda = 1\,\mu$m, for TE polarization.

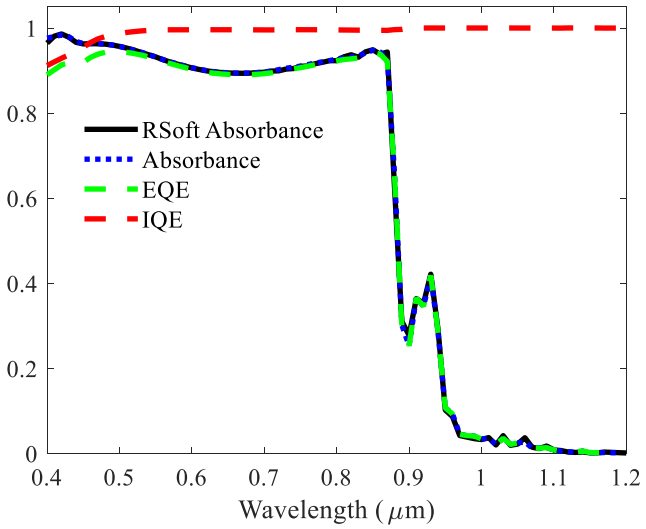

Figure 5.9: The external quantum efficiency (dashed green line), internal quantum efficiency (dashed red line), and absorbance (dotted blue line) are obtained using the electro-optic simulations that utilize the efficient electromagnetic simulation methodology. The solid line indicates the reference active region absorbance spectrum obtained using RSoft DiffractMOD.

5.6 Conclusions

As the studied solar cells become more complex, the possibility of accurately modelling them in an efficient manner becomes increasingly difficult. In particular, the development of a multiphysics simulation platform capable of self-consistently modelling next-generation solar cells incorporating novel materials (e.g. QDs) and optical concepts (e.g. light trapping) has become a significant challenge.

An efficient simulation strategy for patterned thin-film solar cells was presented. The efficient approach demonstrated its potential to replace the computationally intensive optical simulations of the whole device, enabling self-consistent optical-electric simulations feasible for computer-aided design. Several extensions of this strategy are possible, including the application to more complex structures including patterned anti-reflection coatings, and accounting for the photon recycling phenomena, which will play a major role in future devices.

Chapter 6

Conclusions and outlook

Many novel photovoltaic technologies have been developed during recent years with the aim of surpassing the SQ efficiency limit on single-junction solar cells. Among such novel devices, the IBSC has garnered attention due to its spectrum utilization properties and the potential of achieving much higher efficiency than typical single-junction cells. The realization of the IBSC concept is possible using QDs as the IB material where the QD confined states act as intermediate bands that are electrically isolated from the valence and conduction bands. Embedding QDs in III-V materials broadens the absorption bandwidth, where the high absorption of above bandgap photons will be complemented by absorption of sub-bandgap photons in the QD states. Therefore, QDs have the potential to increase the efficiency of III-V solar cells by generating a higher photocurrent while maintaining a high open-circuit voltage. However, they still suffer from multiple limiting factors such as the low absorption exhibited by sub-bandgap QD states and the reduced open-circuit voltage. In addition, the IB operation of QDSCs requires high interband and intraband absorption, which is challenging to achieve due to the competition between second photon absorption and thermal carrier escape.

Light trapping is a promising solution to enhance the photoabsorption, increasing the efficiency of thermally-limited QDSCs and, combined with proper QD material engineering, enabling the IB operating regime. Light trapping enables the enhancement of the effective optical path length, which is also useful when considering thin-film configurations that are advantageous for space applications. Lambertian light trapping is achievable using many diverse photonic structures, with one particularly promising approach being periodic diffraction gratings. The work in Chapter 2 provides a numerical study of light trapping-enhanced QDSCs employing diffraction gratings and nanostructured ARCs to enhance the interband absorption. An optimization of triangular diffraction gratings is performed to maximize the light diffracted to modes propagating at angles higher than the escape cone of GaAs. The relevant parameter that impacts the QD photocurrent is identified to be the grating aspect ratio. By comparing the different configurations based

on the QD photocurrent enhancement, double-side texturing provides the highest performance. Further analysis of the absorbance spectrum beyond the GaAs band edge indicates that the optical path enhancement factor approaches Lambertian limits. This numerical study is complemented in Chapter 3 by experimental characterization of diffraction gratings imprinted on silica and GaAs substrates. Reflectance and diffraction efficiency measurements indicate the light trapping capabilities of textured reflectors. Further development of the studies performed in this work with further experimental measurements or numerical analysis is possible, with one particularly promising direction being the experimental characterization of QDSCs.

The photonic structures studied throughout this work were primarily symmetrical gratings on the front and/or back sides of the solar cell, which were designed with the aim of increasing the effective optical path length of weakly absorbing materials. The shape of the studied diffraction gratings was limited to symmetrical gratings with square-base, while the literature demonstrates that studying asymmetrical or unusual geometries may lead to interesting findings.

One of the main challenges of IBSCs is the thermal escape process that competes with intraband absorption, which is dominant at room temperature operation under 1 sun illumination. A numerical study is presented in Chapter 4 that addresses the first and second photon absorption enhancement of IBSCs using guided-mode resonance gratings. For ultra-thin absorbing layers, resonant gratings enable the guiding of one or few diffracted modes into the active region. The narrowband enhancement achievable using GMR may result in closer matching between intraband and interband absorption. High narrowband enhancement is demonstrated by GMR in the near and mid IR wavelength ranges that correspond to the interband and intraband absorption. The study demonstrates higher impact of GMR on low absorption coefficients, in particular in the MIR wavelength range corresponding to second photon absorption. Multi-resonant enhancement is identified as a potentially viable solution to provide similar enhancement at wider band.

The development of gratings for simultaneous interband and intraband absorption could be realized by combining both absorption enhancement methods. This is promising for IBSC systems that suffer from low first and second photon absorption coefficients. A wideband absorption enhancement can be achieved using diffraction gratings with periods much larger than the wavelength, and narrowband absorption enhancement can be achieved using periodic gratings with feature size in the range of the wavelength. By tuning the grating period and using a thin active region, narrowband enhancement can be possible for the longer wavelengths (second photon), while utilizing a grating shape and aspect ratio that promotes high diffraction at shorter wavelengths (first photon) that are several times smaller than the grating period. The combined effect may allow strong and matching absorption rates of both photons, which is an essential requirement for the proper operation of an IBSC.

The studied solutions allow minimizing the number and density of QD stacks. This results in a smaller open-circuit voltage penalty due to embedding the QDs. Accordingly, an essential objective of the light trapping studies is to decrease the number of QD layers and QD density in order to improve the cell voltage. In addition, growing a smaller number of QD layers is more technologically feasible and results in less defects in the material. The QDSC employing light trapping would demonstrate an increase in the photocurrent while suffering a slightly reduced open-circuit voltage, effectively resulting in an overall higher conversion efficiency for a smaller cell thickness.

A growing research direction is the development of multiphysics simulations on multiple scales to provide a self-consistent electrical and optical solution of the studied solar cells. The issue is particularly relevant to coupled electro-optical simulations of nanostructured absorbers (e.g. QDSCs) that use photonic structures, requiring full-wave electromagnetic simulations. An approach is proposed in Chapter 5 where the photonic structures are reduced to scattering matrices, thereby simplifying the simulation while maintaining accuracy of the results. An electro-optic simulator is used that utilizes the efficient method for periodic photonic structures. The code can be used to model diverse back-side grating shapes and can be modified to incorporate front-side gratings. Combining the computationally efficient electromagnetic tools (e.g. the methods used in Chapter 5) with the electrical modelling tools (as described in Appendix A.2) towards self-consistently coupled simulations has been accomplished.

The investigated photon management techniques have been applied foremost to QDSCs, yet are also applicable to other photovoltaic or photodetection configurations. The proposed methodologies can then act as a useful framework for the study of next-generation solar cells.

Appendix A

Modelling techniques

A.1 Electromagnetic modelling

Modelling of solar cells requires the use of electromagnetic and electrical simulation techniques. Optical modelling is necessary to compute the electromagnetic field propagating through the solar cell illuminated by an incident solar spectrum. Depending on the cell architecture and required accuracy, the absorbed photon density can be computed by solving Maxwell's equations either by approximated approaches or by full-wave numerical schemes, which are recalled in the following sections. The optical generation rate obtained from the electromagnetic (ELM) simulations is then used as input to the continuity equations for charge carriers to compute the electrical behavior of the solar cell under illuminated conditions.

With this respect, it has to be noticed that the development of models for three-dimensional semiconductor systems such as QDSCs also requires ad hoc models to describe the carrier dynamics between extended states in the host material and confined states introduced by the QDs. Towards that end, a Poisson drift-diffusion solver has been developed within our research group at the Politecnico di Torino, which was utilized for the electrical QDSC simulations, and is briefly presented in Sec. A.2.2.

A.1.1 Beer-Lambert model

The Beer-Lambert (BL) model is a simplified model commonly used as the starting point for the study of the light absorption within a structure composed of multiple layers [76]. The model does not account for the reflections caused by the interfaces between different layers, and may be corrected with a front surface reflectance coefficient. The model can be implemented to obtain the estimated absorption as a function of the wavelength (λ) for a specific thickness or per unit length dependent on the position within the structure. The general formulation of the model is found in Equation A.1, which provides the wavelength (λ) and position

(z) dependent absorption in the nth layer (A_n) using simply the nth layer absorption coefficient (α_n), the layer thickness (w_n), and the layer initial position (z_n).

$$A_n(\lambda, z) = \alpha_n(\lambda)\text{exp}(-\sum_{i=1}^{n-1} \alpha_i(\lambda)w_i - \alpha_n(\lambda)(z - z_n)) \tag{A.1}$$

A.1.2 Transfer Matrix Method

The Transfer Matrix Method (TMM) provides an exact solution to multilayer structures, and is more accurate than the BL method as it accounts for the reflection at each interface between different layers [101]. It additionally accounts for the interaction between the incident and reflected waves in terms of coherence effects. This becomes crucial in multilayer structures, where the purpose of some layers is to reduce the front surface reflectance. The TMM outputs the reflection and transmission coefficients for each layer interface.

The method is applicable to one-dimensional structures and is commonly used due to its computational efficiency and accuracy. In particular, this method allows for quick analysis of the effectiveness of multilayer anti-reflection coatings.

The TMM assumes infinite lateral periodicity of the layers, allowing the simplification of the computation [102]. It allows the modelling of the incident light as homogenous polarized EM plane waves, with an electric, E, and a magnetic, H, field component:

$$E = \mathcal{E}\text{exp}\left[i\omega t - \left(\frac{2\pi N}{\lambda}\right) z + \phi\right] \tag{A.2}$$

$$H = \mathcal{H}\text{exp}\left[i\omega t - \left(\frac{2\pi N}{\lambda}\right) z + \phi^{'}\right] \tag{A.3}$$

in which the amplitude of the electric field is indicated by $\mathcal{E}$ and that of the magnetic field by $\mathcal{H}$, with the complex dispersive refractive index denoted by N, the position in the direction of wave propagation by z, the angular frequency by ω, the wavelength of operation by λ, and the phase angles relative to the electric and magnetic components of the EM wave are denoted by ϕ and $\phi^{'}$. The interaction between the electric and magnetic components of the EM waves at the n-layer interface is evaluated using a transfer matrix, assuming a near-infinite substrate, given by:

$$\begin{bmatrix} E \\ H \end{bmatrix} = \left\{ \prod_{q=1}^{n} \begin{bmatrix} \cos(\delta_q) & [i\text{sin}(\delta_q)]/\eta_q \\ i\eta_q\text{sin}(\delta_q) & \cos(\delta_q) \end{bmatrix} \right\} \begin{bmatrix} 1 \\ \eta_m \end{bmatrix} \tag{A.4}$$

where for the q_{th} planar layer, the phase factor is represented by δ_q, the optical admittance by η_q, and η_m being the optical admittance for the infinite substrate. The computation starts with that of the first layer on the side of the incident infinite

medium, followed by the rest of the n-layer structure in the order of propagation. The phase factor δ_q indicates the necessary phase shift in order to shift the z coordinate in the electric and magnetic field interactions in a layer q by its thickness. The Fresnel coefficients are computed in order to obtain the spectral behavior of the reflected, transmitted, and absorbed light in a multilayer structure, using:

$$R = \left(\frac{\eta_0 E - H}{\eta_0 E + H}\right)\left(\frac{\eta_0 E - H}{\eta_0 E + H}\right)^* \tag{A.5}$$

$$T = \frac{4\eta_0 Re(\eta_m)}{(\eta_0 E + H)(\eta_0 E + H)^*} \tag{A.6}$$

$$A = \frac{4\eta_0 Re(\eta_m)}{(\eta_0 E + H)(\eta_0 E + H)^*} \tag{A.7}$$

The TMM can also be combined with the Effective Index Method (EIM) in order to estimate the optical behavior of two-dimensional structures [103]. The EIM entails that a layer composed of multiple materials with different refractive indexes, can be represented with a single index that provides a somewhat rough representation of the layer. As the equivalent layer thickness decreases, the combined method accuracy tends to increase [104].

A.1.3 Rigorous Coupled Wave Analysis

The rigorous coupled wave analysis (RCWA) method extends the TMM for multi-dimensional structures where the wave interaction in the lateral directions is considered as well. The RCWA method provides an efficient formalism for laterally periodic structures, while maintaining accuracy as it theoretically computes an exact solution for Maxwell's equations [71, 70, 105]. The periodicity of the structure is also assumed where a unit cell with specific boundary conditions is defined. Due to the formulism comprising a summation of an infinite series, the point at which the series is truncated defines the simulation resolution, which is determined using a convergence analysis.

The Maxwell's equations are expressed below in their differential form after factoring out the time harmonic factor e^{-iwt}:

$$\begin{aligned}
\frac{\partial}{\partial y}E_z - \frac{\partial}{\partial z}E_y &= i\omega\mu H_x \\
\frac{\partial}{\partial z}E_x - \frac{\partial}{\partial x}E_z &= i\omega\mu H_y \\
\frac{\partial}{\partial x}E_y - \frac{\partial}{\partial y}E_x &= i\omega\mu H_z
\end{aligned} \tag{A.8}$$

$$\begin{aligned}
\frac{\partial}{\partial y}H_z - \frac{\partial}{\partial z}H_y &= -i\omega\varepsilon_0\varepsilon_{r,x}\mu E_x \\
\frac{\partial}{\partial z}H_x - \frac{\partial}{\partial x}H_z &= -i\omega\varepsilon_0\varepsilon_{r,y}\mu E_y \\
\frac{\partial}{\partial x}H_y - \frac{\partial}{\partial y}H_x &= -i\omega\varepsilon_0\varepsilon_{r,z}\mu E_z
\end{aligned} \tag{A.9}$$

in which case the medium takes the form of an index tensor on the diagonal relative to the principle axes containing the elements $\varepsilon_{r,x}$, $\varepsilon_{r,y}$, and $\varepsilon_{r,z}$. By inserting each of the Equations A.8 into each of Equations A.9, the Maxwell's equations can then be expressed in the transverse format as:

$$\begin{aligned}
\frac{\partial}{\partial z}E_x &= \frac{-i}{\omega\varepsilon_0}\frac{\partial}{\partial x}\frac{1}{\varepsilon_{r,z}}\frac{\partial}{\partial y}H_x + \left(\frac{i}{\omega\varepsilon_0}\frac{\partial}{\partial x}\frac{1}{\varepsilon_{r,z}}\frac{\partial}{\partial x} + i\omega\mu\right)H_y \\
\frac{\partial}{\partial z}E_y &= \left(\frac{-i}{\omega\varepsilon_0}\frac{\partial}{\partial y}\frac{1}{\varepsilon_{r,z}}\frac{\partial}{\partial y} - i\omega\mu\right)H_x + \frac{i}{\omega\varepsilon_0}\frac{\partial}{\partial y}\frac{1}{\varepsilon_{r,z}}\frac{\partial}{\partial x}H_y
\end{aligned} \tag{A.10}$$

$$\begin{aligned}
\frac{\partial}{\partial z}H_x &= \frac{i}{\omega\mu}\frac{\partial}{\partial x}\frac{\partial}{\partial y}E_x + \left(\frac{-i}{\omega\mu}\frac{\partial}{\partial x}\frac{\partial}{\partial x} - i\omega\varepsilon_0\varepsilon_{r,y}\right)E_y \\
\frac{\partial}{\partial z}H_y &= \left(\frac{i}{\omega\mu}\frac{\partial}{\partial y}\frac{\partial}{\partial y} + i\omega\varepsilon_0\varepsilon_{r,x}\right)E_x + \frac{-i}{\omega\mu}\frac{\partial}{\partial y}\frac{\partial}{\partial x}E_y
\end{aligned} \tag{A.11}$$

Solving the aforementioned equations in the spatial domain with the appropriate boundary conditions becomes computationally intensive. Additionally, the computation of the order dependent diffraction efficiencies requires the use of fine simulation grids. However, the RCWA method is based in the Fourier domain, which provides the solution more efficiently in order to obtain the amplitudes and angles of each diffraction order.

The RCWA method approximates the curved or sharp edges using a layered geometry, as shown in Fig. A.1. The method allows the simplification of the studied grating structures into homogenous stratified regions in the vertical direction, with constant values for $\varepsilon_{r,x}$, $\varepsilon_{r,y}$, and $\varepsilon_{r,z}$ independently of z. Accordingly, any complex structure can be represented by stacks comprising multiple homogenous layers.

The periodicity of the studied grating structures is exploited by expressing the field components in a periodically repeated layer using Bloch's Theorem as:

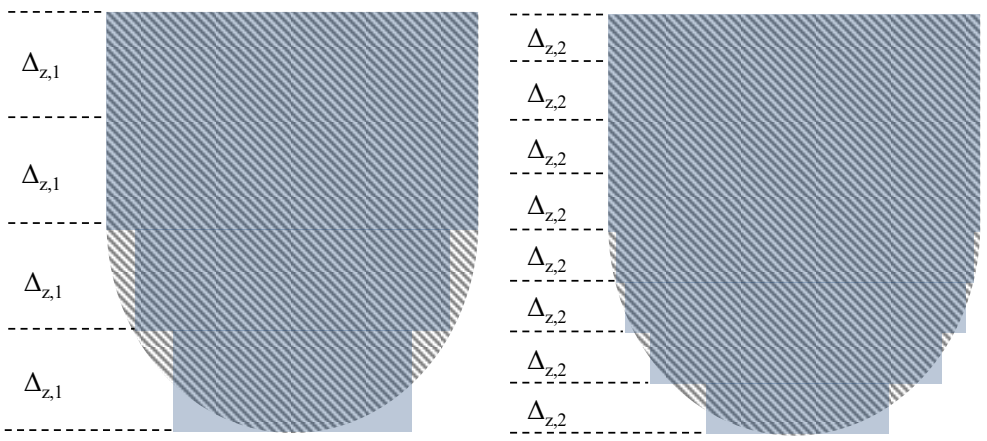

Figure A.1: The structural approximation of curved shapes implemented in the RCWA method.

$$
\begin{aligned}
E_x &= e^{i(k_{x,0}x+k_{y,0}y}\sum_p\sum_q e^{i\left(\frac{2\pi}{\Lambda_x}px+\frac{2\pi}{\Lambda_y}qy\right)}\sum_m a_{x,m,p,q}\left(f_m e^{ik_m z}+g_m e^{-ik_m z}\right)\\
E_y &= e^{i(k_{x,0}x+k_{y,0}y}\sum_p\sum_q e^{i\left(\frac{2\pi}{\Lambda_x}px+\frac{2\pi}{\Lambda_y}qy\right)}\sum_m a_{y,m,p,q}\left(f_m e^{ik_m z}+g_m e^{-ik_m z}\right)\\
H_x &= e^{i(k_{x,0}x+k_{y,0}y}\sum_p\sum_q e^{i\left(\frac{2\pi}{\Lambda_x}px+\frac{2\pi}{\Lambda_y}qy\right)}\sum_m b_{x,m,p,q}\left(f_m e^{ik_m z}+g_m e^{-ik_m z}\right)\\
H_y &= e^{i(k_{x,0}x+k_{y,0}y}\sum_p\sum_q e^{i\left(\frac{2\pi}{\Lambda_x}px+\frac{2\pi}{\Lambda_y}qy\right)}\sum_m b_{y,m,p,q}\left(f_m e^{ik_m z}+g_m e^{-ik_m z}\right)
\end{aligned}
\tag{A.12}
$$

Equations A.12 are then combined with Equations A.10 and A.11 in order to resolve the eigenvalue problem $\mathbf{Ax} = \lambda\mathbf{x}$, where $\mathbf{A}$ is obtained using the operators in Equations A.10 and A.11, $\lambda = k_m^2$ becomes the eigenvalue to be computed, and a and b found in Equation A.12 are obtained from their relative eigenvectors.

Equations A.12 can then be solved for the complete structure by utilizing transmission line theory in order to resolve the necessary boundary value problem [106]. A derivation provides the scattering characteristics of the structure. The amplitudes of the modal current and voltage can then be expressed for the j^{th} layer as:

$$
\begin{aligned}
v_m^{(j)} &= f_m^{(j)}e^{ik_m z}+g_m^{(j)}e^{-ik_m z}\\
i_m^{(j)} &= f_m^{(j)}e^{ik_m z}-g_m^{(j)}e^{-ik_m z}
\end{aligned}
\tag{A.13}
$$

where j corresponds to the layer in question, which is attributed with its own values. Adding the necessary boundary condition at the position z_j^{j+1} in between layers j and $(j+1)$ allows the derivation of:

$$\begin{aligned}\sum_m \begin{pmatrix} a_{x,m,p,q} \\ a_{y,m,p,q} \end{pmatrix}^{(j)} \nu_m^{(j)}(z_j^{j+1}) &= \sum_m \begin{pmatrix} a_{x,m,p,q} \\ a_{y,m,p,q} \end{pmatrix}^{(j+1)} \nu_m^{(j+1)}(z_j^{j+1}) \\ \sum_m \begin{pmatrix} b_{x,m,p,q} \\ b_{y,m,p,q} \end{pmatrix}^{(j)} i_m^{(j)}(z_j^{j+1}) &= \sum_m \begin{pmatrix} b_{x,m,p,q} \\ b_{y,m,p,q} \end{pmatrix}^{(j+1)} i_m^{(j+1)}(z_j^{j+1})\end{aligned} \tag{A.14}$$

This allows the numerical simplification of the problem in order to efficiently solve for periodic structures. Periodic structures are common for solar cells implementing diffraction gratings for the purpose of scattering the incoming light towards the active region. The simulation parameters include the number of harmonics (Fourier orders) to be considered in the approximation as well as the spatial resolution of the complex refractive index (permittivity and absorption coefficient) which determines the number of layers that the structure will be divided into. A finer resolution and higher number of harmonics result in a more accurate output at the expense of computational memory and speed.

A.1.4 Finite Difference Time Domain

For non-periodic photonic structures, the electromagnetic fields can be computed using the discretized form of Maxwell's equations in the time domain [107]. The Finite Difference Time Domain (FDTD) method allows solving Maxwell's equations, which can be expressed in their differential time-dependent form as:

$$\frac{\partial \vec{B}}{\partial t} = -(\nabla \times \vec{E}) - \vec{M} \frac{\partial \vec{D}}{\partial t} = -(\nabla \times \vec{H}) - \vec{J} \tag{A.15}$$

where $\vec{B}$ is the magnetic flux density, $\vec{D}$ is the electric flux density, $\vec{M}$ is the total magnetic current density, and $\vec{J}$ is the total electric field density. In FDTD, the vector form of the equations is expressed in a finite-difference format, allowing them to be solved numerically on a computational grid commonly referred to as the Yee grid [108]. The Yee grid, shown in Fig. A.2, contains the six field components on separate yet intertwined grids that occupy a unit cell in space taking the form of a cube. The Yee grid presents a simple method that is applicable to obtain broadband, full-wave solutions of Maxwell's equations in the time domain.

For a linear and isotropic medium of propagation without dispersive properties, the magnetic and electric flux densities can be described in terms of the electric and magnetic fields, $\vec{E}$ and $\vec{H}$, respectively, with the below relationships:

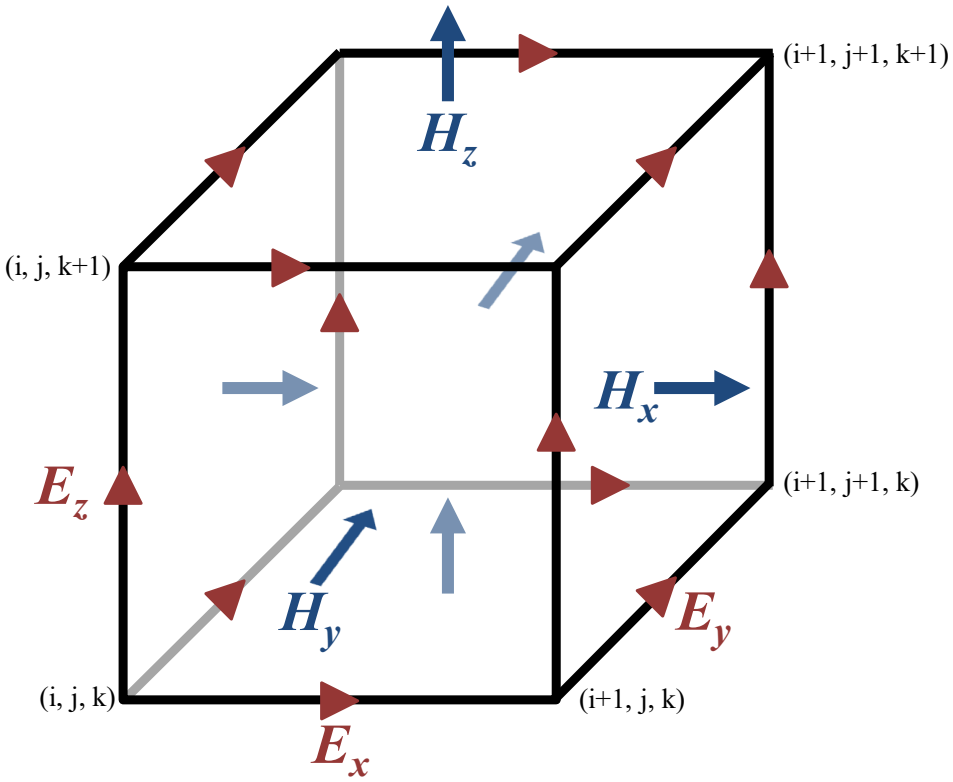

Figure A.2: The Yee computational grid utilized to obtain full-wave solutions of Maxwell's equations using FDTD.

$$\begin{aligned} \frac{\partial \vec{H}}{\partial t} &= -\frac{1}{\mu_0 \mu_r}[(\nabla \times \vec{E}) + (\vec{M_{source}} + \sigma^* \vec{H})] \\ \frac{\partial \vec{E}}{\partial t} &= -\frac{1}{\epsilon_0 \epsilon_r}[(\nabla \times \vec{H}) - (\vec{J_{source}} + \sigma^* \vec{E})] \end{aligned} \tag{A.16}$$

Consequently, the expansion of the curl followed by substitution of the vector components, assuming time invariance for the permittivity and the permeability, results in the expansion of the Equations A.16 into a generalized format comprising of six scalar equations:

$$\begin{aligned}
\frac{\partial H_x}{\partial t} &= -\frac{1}{\mu_0 \mu_r}\left[\left(\frac{\partial E_z}{\partial y} - \frac{\partial E_y}{\partial z}\right) - (M_{source_x} + \sigma^* H_x)\right] \\
\frac{\partial H_y}{\partial t} &= -\frac{1}{\mu_0 \mu_r}\left[\left(\frac{\partial E_z}{\partial x} - \frac{\partial E_x}{\partial z}\right) - \left(M_{source_y} + \sigma^* H_y\right)\right] \\
\frac{\partial H_z}{\partial t} &= -\frac{1}{\mu_0 \mu_r}\left[\left(\frac{\partial E_x}{\partial y} - \frac{\partial E_y}{\partial x}\right) - (M_{source_z} + \sigma^* H_z)\right] \\
\frac{\partial E_x}{\partial t} &= -\frac{1}{\epsilon_0 \epsilon_r}\left[\left(\frac{\partial H_z}{\partial y} - \frac{\partial H_y}{\partial z}\right) - (J_{source_x} + \sigma E_x)\right] \\
\frac{\partial E_y}{\partial t} &= -\frac{1}{\epsilon_0 \epsilon_r}\left[\left(\frac{\partial H_x}{\partial z} - \frac{\partial H_z}{\partial x}\right) - \left(J_{source_y} + \sigma E_y\right)\right] \\
\frac{\partial E_z}{\partial t} &= -\frac{1}{\epsilon_0 \epsilon_r}\left[\left(\frac{\partial H_y}{\partial x} - \frac{\partial H_x}{\partial y}\right) - (J_{source_z} + \sigma E_z)\right]
\end{aligned} \tag{A.17}$$

Using the below notation for temporally and spatially varying functions provides a derivative for space and time of Equations A.17:

$$u^n_{i,j,k} = (i\delta x, j\delta Y, k\delta z, n\delta t) \tag{A.18}$$

where δx, δy, δz, indicate the grid cell's physical dimensions, δt the time step, and δn the time index. The derivative of Equation A.18 in time and space can then be utilized and applied to Equations A.16 in order to derive a set of finite-difference equations that are explicitly coupled and can then be solved for 1D, 2D, or 3D structures.

However, the accuracy of the FDTD method requires high memory resources, as a fine mesh is necessary to avoid numerical instability and dispersion. Solving the discretized equations requires the use of a grid appropriate to the wavelength of operation, where a general recommendation is the use of a grid mesh that is a minimum of 20 times lower than the wavelength. In addition, the discretized Maxwell equations in A.17 do not account for the wavelength dependence of the optical properties of the materials. Accordingly, a dispersive model is necessary for broadband simulations, which expresses the complex refractive indexes of the materials using polynomial functions. To this end, modified Lorenz and Drude-modified Lorenz models are commonly utilized to express the permittivity as a function of frequency. However, some materials exhibit high variations in their refractive indexes, resulting in difficulty in modelling them analytically. The only possibility becomes to run multiple narrow band simulations, which requires higher computational time and resources. Another limitation of the method arises from the inability to easily model materials with a small refractive index such as metals that are commonly used as back reflectors [109].

A.2 Electrical modelling

A.2.1 Detailed Balance

The Detailed Balance (DB) is an approach proposed in 1961 by Shockley and Queisser that allows the calculation of a junction's electrical properties utilizing the balancing of the carrier generation and recombination processes occurring within the solar cell [2]. The method allows the estimation of the maximum attainable efficiency by a multitude of solar cell materials and architectures.

A rudimentary implementation of the DB model requires the absorption band edge energy and an absorption coefficient beyond the edge, providing the photo-carrier generation as well as the radiative recombination. A complete absorption profile provides a more accurate description of the solar cell characteristics.

The radiative generation current (J_{rad}) accounts for the reciprocity between the absorption and emission, and its formalism described in [110] is:

$$J_{rad} = q \int_0^\infty \int_S A(E, \theta, \mathbf{s}) b(E, \Delta\phi) \mathrm{d}\Omega \mathrm{dS} \mathrm{d}E \tag{A.19}$$

in which $A(E, \theta, \mathbf{s})$ represents the probability of a photon with energy E to undergo emission (absorption) at the surface point $\mathbf{s}$ of a device surface S, for the internal angle being θ, and $b(E, \Delta\phi)$ is the photon flux density at a given spectrum due to spontaneous emission. By substituting the spectral photon flux density term with the generalized Planck equation and accounting for the possible light paths leading to absorption, the radiative recombination current as a function of bias voltage and temperature can be expressed as:

$$\begin{aligned} J_{rad}(V,T) &= q\frac{2n^2}{h^3c^2} \int_0^\infty \frac{E^2}{e^{\frac{E-qV}{k_\mathrm{B}T}} - 1} \times \left[\int_S A(E, \theta, \mathbf{s}) \mathrm{d}\Omega \mathrm{dS} \right] \mathrm{d}E \\ &= q\frac{2n^2}{h^3c^2} \int_0^\infty \frac{E^2}{e^{\frac{E-qV}{k_\mathrm{B}T}} - 1} \times [A_{front}(E) + A_{back}(E)] \mathrm{d}E \end{aligned} \tag{A.20}$$

where V is the bias voltage, T the ambient temperature, n the medium refractive index, h Planck's constant, c the speed of light, and the $A_{front}(E)$ and $A_{back}(E)$ represent the probability of said photon to undergo emission (absorption) at the front or back side of the cell. The light absorbed can take one of several paths that impact the absorptivity based on the angle of incidence of each path.

Light incident onto the front surface at an angle lower than that corresponding to the escape cone ($\theta < \theta_c$) will pass through the structure, while that incident at higher angles will be reflected. Within the structure, some light is incident onto the back surface at angles exceeding that of the escape cone ($\theta > \theta_c$), resulting in total internal reflection and effectively going through the structure twice. Other light within the structure reaches the back surface at an angle lower than that of the escape cone ($\theta < \theta_c$) and may either escape at the front side or be partially

reflected into the structure. The combined reflection processes are combined and represented using reflection coefficients.

The photogeneration of carriers within the solar cell due to the incident solar irradiance $H(E)$ can be expressed as:

$$J_{\mathrm{SC}} = q \int_0^{\infty} [1 - R(E)] A_n(E) H(E) \mathrm{d}E \tag{A.21}$$

where R corresponds to the reflection at normal incidence and A_n the absorptivity at normal incidence, which is expressed by $A(E) = 1 - e^{-\alpha(E)w}$ for a junction thickness w and an absorption coefficient α.

Therefore, the total current can be computed using the DB model as:

$$J = J_{\mathrm{SC}} + J_{rad}(0, T_a) - J_{rad}(V, T_{cell}) \tag{A.22}$$

where the term $J_{rad}(V, T_{cell})$ represents the radiative recombination for a value of bias voltage V and a cell temperature of T_{cell} while $J_{rad}(0, T_a)$ represents the carrier generation as a result of thermal radiation at the temperature value T_a. Assuming a cell temperature $T_a = T_{cell}$ and an energy $E \gg k_{\mathrm{B}}T$, the Equation A.22 can be simplified to:

$$J = J_{\mathrm{SC}} - J_{01} \left(e^{\frac{qV}{k_{\mathrm{B}}} T_{cell}} - 1 \right) \tag{A.23}$$

for a reverse saturation current J_{01} expressed by:

$$J_{01} = q \frac{2n^2}{h^3 c^2} \int_0^{\infty} E^2 e^{-\frac{E}{k_{\mathrm{B}} T_{cell}}} [A_{front}(E) + A_{back}(E)] \mathrm{d}E \tag{A.24}$$

A model with a higher degree of complexity, and accordingly accuracy, is the two-diode model, which accounts for the radiative recombination as well as the non-radiative recombination. In this case, the coefficient representing the non-radiative recombination can be estimated using an ideality factor which models the recombination losses. The estimated values for the saturation current as well as that of the ideality factors can be obtained from the cell structure and its material properties. The radiative efficiency can then be defined as the ratio of the radiative current to a total reference current, which can alternatively be used to derive the non-radiative recombination coefficient.

A.2.2 QDSC drift-diffusion model

Poisson-Drift-Diffusion (PDD) is commonly used for the modelling of semiconductors due to its accuracy, as it is capable of modelling carrier dynamics [111, 112]. The Poisson and continuity equations can be expressed as:

$$-\nabla \cdot (\epsilon \nabla \varphi) - \rho = 0 \tag{A.25}$$

$$\begin{aligned} q\frac{\partial n}{\partial t} - \nabla \cdot \mathbf{J}_n &= q(G-R) \\ q\frac{\partial p}{\partial t} + \nabla \cdot \mathbf{J}_p &= q(G-R) \end{aligned} \tag{A.26}$$

where ϵ is the electric permittivity in the simulated material, q is the elementary charge constant, φ is the electric potential within the device, n and p represent the electron and hole (i.e. charge carriers) densities per unit volume, respectively, ρ is the charge density in a unit volume, $\mathbf{J}_n$, $\mathbf{J}_p$ are the vector electric current density for a unit area, G is photogeneration rate, and R is the recombination rate.

The Poisson equation in Equation A.25 describes the localized variation in the electric field as a result of the charge density for a point in a volume. The drift-diffusion model adds the description of charge carrier transport as a result of:

- An electric field $E = -\nabla\varphi$ that causes carriers to move at a velocity v, resulting in drift current.
- A concentration gradient characterized by electron and hole diffusivity coefficients D_n and D_p, resulting in diffusion current.

The combined DD model accounts for both contributions as:

$$\begin{aligned} \mathbf{J}_n &= -q\mu_n n\nabla\varphi + qD_n\nabla n \\ \mathbf{J}_p &= -q\mu_p p\nabla\varphi + qD_p\nabla p \end{aligned} \tag{A.27}$$

where μ is the mobility for electrons or holes, characterizing the drift velocity. The contributions in Equation A.27 of the drift (left) and diffusion (right) are independent, but the diffusivity coefficients can be related to the mobilities of electrons and holes by:

$$\begin{aligned} D_n &= \mu_n \frac{n}{q\frac{\partial n}{\partial \varphi_n}} \\ D_n &= \mu_p \frac{p}{q\frac{\partial p}{\partial \varphi_p}} \end{aligned} \tag{A.28}$$

The differential form of the equations describes the local microscopic mechanisms in a material. Solving the equations for pre-defined structures and with specified boundary conditions is performed to obtain the potential distribution as well as the distribution of electrons and holes, enabling the computation of the relevant currents for a specified cross section. The inputs to the system include the mobilities, dopings, diffusion coefficients, and the recombination mechanisms. Closed form solutions can be obtained using analytical methods for simple structures [113]. In most cases, however, numerical methods are employed.

The semiclassical drift-diffusion model can be quantum corrected to include the physics of the QD material, leading to an approximated yet accurate description of

the interaction between confined and extended states [68, 114, 100]. The approach proposed in [68] is a classical drift-diffusion framework for transport of bulk carriers coupled with QD rate equations to properly treat QD carrier dynamics, as shown in Fig. A.3 for an active region comprising of an N-layer QD stack in the active region material. The model accounts for band to band charge transfer due to photogeneration and recombination whereas the charge transfer between subband energy states happens only through thermal cascaded intersubband capture and relaxation. This is a proper choice at room temperature for the InAs/GaAs material system since optical intersubband processes are negligible with respect to the thermally activated ones [115]. On the other hand, the model can be extended to deal with intersubband optical transitions in material systems with relatively higher energy subband separation (or for lower operating temperature) where thermal transitions are somewhat suppressed [116].

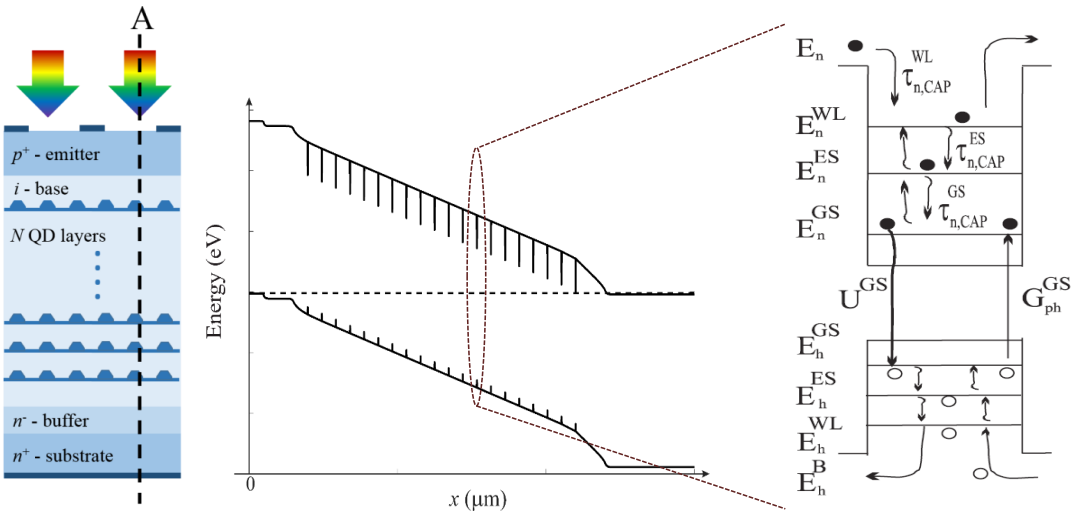

Figure A.3: The energy band of a QDSC is shown, highlighting the carrier dynamics. The figure was adapted from [68].

Appendix B

Experimental characterization of QDSCs

B.1 Purpose of the study

As temperature-dependent photoluminescence may provide further insight into the carrier dynamics [117], the measurements were performed to the QDSC samples grown by the Optoelectronics Research Centre (ORC) group at the Tampere University. However, one of the main challenges faced by this characterization approach is the difficulty in data analysis due to the multiple underlying mechanisms affecting the measured parameters.

Despite the complexity of the analysis process, the PL measurements assist in the estimation of multiple parameters. For instance, the band edge of a material can be extracted using the peak energy of the PL signal. In addition, the activation energy can be estimated using the behavior of the PL with varying temperatures. Finally, the light ideality factor of the grown samples can be estimated through varying of the excitation power and measuring the corresponding change in the PL signal.

B.2 Theoretical background

Photoluminescence is the process of light emission by a material following the absorption of photons incident from an excitation source. Various underlying mechanisms within the material will result in different emission properties. Regarding experimental characterization, PL measurements involve the excitation using photons with a pre-determined energy and intensity, followed by the measurement of the energy and intensity of the emitted photons from the material due to the excitation.

B.2.1 Excitation sources

In the specific case of PL for QDSCs, the excitation can be classified into three schemes: non-resonant, quasi-resonant, and resonant excitations, which are shown in Fig. B.1 [118].

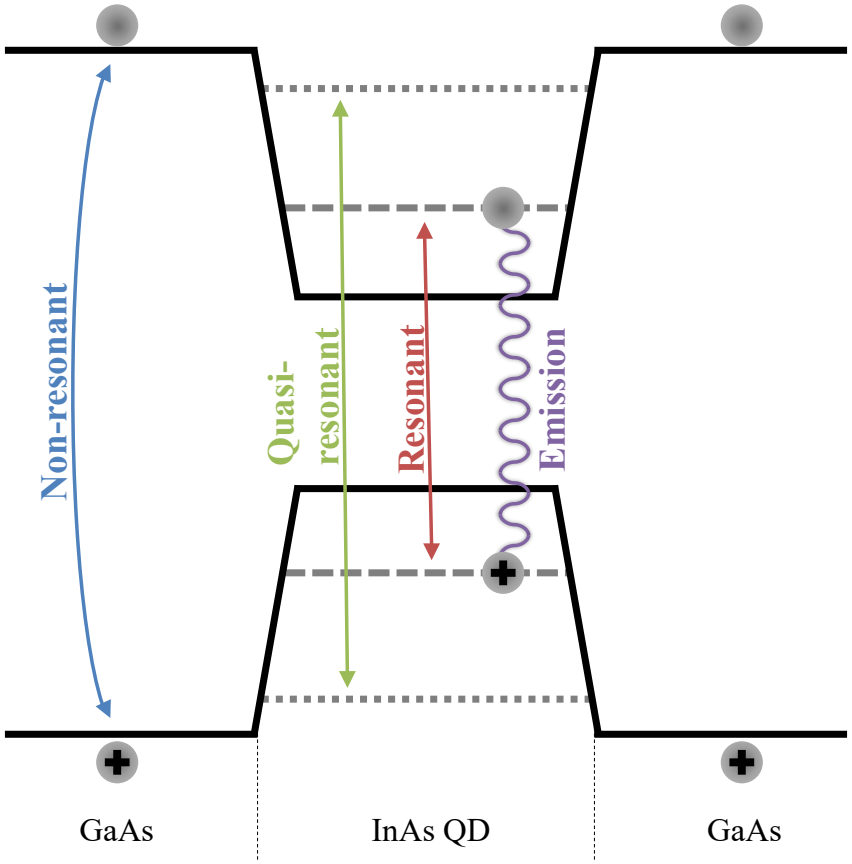

Figure B.1: PL excitation mechanisms: non-resonant, quasi-resonant, and resonant excitation.

For non-resonant excitation, the sample is excited with high energy photons, resulting in excess energy. This is commonly used in PL measurements where the excitation source can be a laser diode and the excitation energy can be filtered using optical filters. The challenge arises when distinguishing between the barrier excitation and quasi-resonant excitation.

Regarding quasi-resonant excitation, the excitation energy is tuned to be beyond the ground state energy, but below the absorption edge of the barrier.

As for resonant excitation, the laser's emission wavelength corresponds to the lowest exciton resonance of the QW or QD system, resulting in minimal excess

injected energy into the system and high efficiency. The main advantage of resonant emission is that it allows the highest photon distinguishability for better understanding of the system mechanisms. However, the detection of the PL signal becomes more challenging since diffuse scattering or background light noise may interfere with the detected signal.

B.2.2 Temperature-dependent photoluminescence measurements

The variation in the measured PL signal can be analyzed in multiple ways to obtain relevant parameters. First, the energy corresponding to the maximum point on the PL intensity vs. energy spectrum (i.e. the peak energy) can be observed relative to the variation in temperature. In particular, the direct and indirect energy gaps for a bulk semiconductor material depend on the temperature according to the empirical Varshni formula:

$$E_g(T) = E_g(T=0) - \frac{\alpha_v T^2}{T + \beta_v} \tag{B.1}$$

where E_g is the energy band gap, $E_g(T = 0)$ is the energy band gap at a temperature approaching 0 K, and α_v and β_v are the variable Varshni parameters [119].

Next, the variation of the integrated intensity of the PL signal with temperature can also be interpreted according to the modified Arrhenius formula [120, 121]. Assuming a single channel for the non-radiative recombination, the simplified 3-parameter Arrhenius formula can be expressed as:

$$I(T) = \frac{I_0}{1 + a\exp(-E_\mathrm{a}/k_\mathrm{B}T)} \tag{B.2}$$

where $I(T)$ is the integrated intensity of the PL signal at a temperature T, I_0 is the integrated intensity at a temperature approaching 0 K, E_a is the non-radiative activation energy, and k_B is Boltzmann's constant. The left side is commonly divided by I_0 for normalization of the intensity. The activation energy E_a in quantum well (QD) and QD systems is usually referred to as the energy barrier experienced by a trapped carrier, which is correlated to the energy difference between the conduction band of the barrier top and the carrier's energy state [121]. The parameter a is the ratio between radiative and non-radiative carrier lifetimes, which can be given by:

$$a = \frac{\tau_R}{\tau_0} \tag{B.3}$$

where τ_R represents the radiative lifetime of carriers and τ_0 represents the constant associated with the non-radiative lifetime of carriers. For bulk GaAs cells and

simplified models of InAs/GaAs QDSCs, the temperature dependence of the radiative carrier lifetime is not taken into account, and therefore the parameter a can be assumed to be a constant [120]. In the case of a model involving the variation of the radiative lifetime varies with the temperature, τ_R is then given by:

$$\tau_R = \tau_{R0} T \tag{B.4}$$

and the parameter a is thereby expressed as:

$$a = a_0 T = \frac{\tau_{R0} T}{\tau_0} \tag{B.5}$$

The addition of multiple non-radiative recombination channels to the QDSC model would also result in additional terms corresponding to each channel, with activation energies $E_{a,n}$ for n channels [120]. The comprehensive modified Arrhenius formula can therefore expanded to:

$$I(T) = \frac{I_0}{1 + \sum^{n} a_{0,n} T \exp(-E_{a,n}/k_{\mathrm{B}} T)} \tag{B.6}$$

B.2.3 Intensity-dependent photoluminescence measurements

Another characterization method consists of the variation of the excitation source's power and measuring the corresponding increase in the integrated intensity of the PL signal over multiple values. The linear variation of the power ideally produces a linear shift in the intensity, with the slope commonly referred to as the Ideality Factor (IF) [122, 123]. Using PL measurements allows the estimation of the IF, which is correlated with the ratio that is more accurately predicted using open-circuit voltage measurements of the solar cell under various solar concentrations. An ideality factor approaching 1 indicates a linear dependence while that above 1 indicates a superlinear dependence, which is associated with reduced performance.

B.2.4 Limitations of the PL study

The QD samples used in this study are within a doped p-i-n junction, which behave differently from undoped samples during PL measurements. In addition, non-resonant and resonant PL excitations have different effects based on the type of sample studied [120]. In general, carriers undergo transport from the energy barriers to the quantum wells when the non-resonant excitation method is used. The two main mechanisms are drift and diffusion, which account for carrier transport in the PL measurement process. Diffusion occurs due to the carrier concentration gradient and drift occurs due the electric field in the structure. For samples with a p-n or p-i-n junction, due to the existence of a built-in electric field, the carriers could undergo transport from the barriers to the quantum wells due to both diffusion

and drift. However, for samples without a doped p-n junction, the carriers that are generated in the barriers can undergo transport to the quantum wells only through the diffusion mechanism under non-resonant PL excitation. This complicates the characterization of samples including p-n junctions. A way to mitigate this is utilizing resonant excitation, where the carriers can only be generated within the quantum wells, while the barriers cannot be excited optically as the excitation source energy is lower than that of the barrier band gap. Therefore, resonant PL excitation does not result in any carrier transport from the barriers to the quantum wells. Temperature-dependent PL intensity measurements under resonant excitation conditions allow the characterization of thermal activation characteristics of the non-radiative recombination mechanisms within the quantum dots. However, for non-resonant excitation, the temperature-dependent integrated PL intensity demonstrates the combined impact of carriers undergoing transport from the energy barriers into the wells, as well as carriers recombining in the wells. Consequently, a traditional analysis using the Arrhenius plot does not provide insight into the non-radiative mechanisms.

B.3 Experimental set-up and parameters

The temperature-dependent photoluminescence measurements were performed at the Tampere University laboratories using a setup mainly comprising of an excitation source, reference and sample photodetection blocks, an attenuation block, and a cryogenic temperature-regulated chamber. The analyzed structures are described in Table B.1. Two architectures are investigated: shallow junction (SJ) and deep junction (DJ). The SJ configuration comprises a shallow 100 nm n-GaAs emitter and a 2100 nm p-GaAs while the DJ configuration has a deep 2100 nm n-GaAs emitter and a 100 nm p-GaAs base. The growth process and characterization of the QDSC samples are further elaborated in [124].

A coherent, continuous-wave laser diode operating at a wavelength of 680 nm was used as the non-resonant excitation source for the study, which was sufficient to excite the GaAs and the InAs QDs beyond the band edge. The laser signal was mechanically chopped at 275 Hz. The PL signal measurement set-up employed a monochromator to disperse the light. Next, an InGaAs photodetector (with a cut-off at 1.7μm) was used to detect the intensity of dispersed PL signal, and the output was read by a lock-in amplifier to measure the signal. The detector time constant (shutter speed) was maintained at 100 ms and the sensitivity was varied manually according to measured signal amplitude. The laser and photodetector temperatures were regulated using thermoelectric (Peltier) cooling systems. A shortpass filter with a 700 nm cut-off wavelength is placed before the chopper to eliminate noise in the laser signal. In addition, a longpass filter with a 750 nm cut-off wavelength is placed before the monochromator to clip the short wavelength range of the incoming

Table B.1: The QDSC samples characterized using photoluminescence measurements. Light is incident at the first layer.

DJ/GaAs (Sample ID: 2262)	**DJ/QD (Sample ID: 2272)**
300 nm n-GaAs contact	300 nm n-GaAs contact
20 nm n-AlInP window	20 nm n-AlInP window
2100 nm n-GaAs	2100 nm n-GaAs
435 nm i-GaAs	435 nm i-GaAs with InAs QDs
100 nm p-GaAs base	100 nm p-GaAs base
75 nm p-$Al_{0.2}Ga_{0.8}As$ BSF	75 nm p-$Al_{0.2}Ga_{0.8}As$ BSF
50 nm p-GaAs contact	50 nm p-GaAs contact
GaAs wafer	GaAs wafer
SJ/GaAs (Sample ID: 2275)	**SJ/QD (Sample ID: 2274)**
300 nm n-GaAs contact	300 nm n-GaAs contact
20 nm n-AlInP window	20 nm n-AlInP window
100 nm n-GaAs	100 nm n-GaAs
435 nm i-GaAs	435 nm i-GaAs with InAs QDs
2100 nm p-GaAs base	2100 nm p-GaAs base
75 nm p-$Al_{0.2}Ga_{0.8}As$ BSF	75 nm p-$Al_{0.2}Ga_{0.8}As$ BSF
50 nm p-GaAs contact	50 nm p-GaAs contact
GaAs wafer	GaAs wafer

PL signal and reduce measured noise.

The temperature-dependent PL was measured for a laser power density of 3 W/cm^2 obtained by injecting a current of 640 mA. The sample was placed in a closed-loop cryostat, allowing the temperature to be varied from 15 K to 300 K for the PL measurements. The laser spot area was approximately 1 mm^2. The power of the laser is controlled using an attenuation wheel to vary the power incident on the QDSC samples. The laser power was measured using a reference photodetector for normalization of the results and excitation power-dependent PL measurements were performed for a laser power of 0.6–35 mW at room temperature.

B.4 Measured PL results and analysis

Initially, measurements were performed for the unetched samples, with the 300 nm GaAs contact layer. The measured PL at varied temperature is shown in

Fig. B.2. The PL spectra demonstrate excessive noise due to the doped GaAs contact layer, which is possibly related to the dopant material that causes a tail in the PL signal for wavelengths beyond 900 nm. Accordingly, the GaAs contact layer was etched by being placed in an etchant solution for a predetermined period of time, which resulted in the updated structure starting with the AlInP window layer.

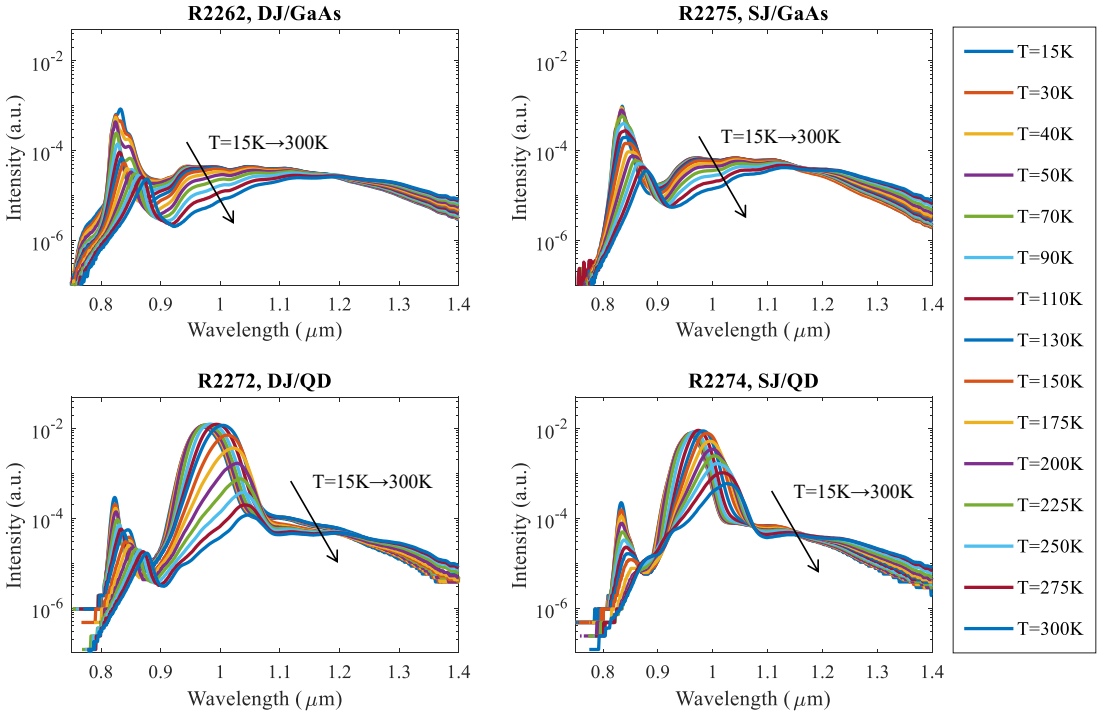

Figure B.2: Spectral PL intensity measurements at varying temperatures for the samples prior to etching of the GaAs contact layer.

Following the etching, the samples were measured using the same PL set-up at various temperatures between 15 K and 300 K. The spectra, shown in Fig. B.3, demonstrate a clearer peak at the GaAs band-edge and for the QDSC samples, and two additional peaks corresponding to the GS and ES of the InAs QDs, as the WL peak is indifferentiable from the GaAs peak. At room temperature, the peak wavelengths for the DJ/QD sample were at 1.05μm and 0.935μm, corresponding to a GS bandgap energy of 1.18 eV and an ES bandgap energy of 1.33 eV. The peak wavelengths for the SJ/QD sample were in a similar range, at 1.025μm and 0.928μm, corresponding to bandgap energies of 1.21 eV and 1.34 eV for the GS and the ES, respectively. The measurements were then post-processed to express the PL intensity as a function of both the temperature (K) and the energy (eV) in the 2D Arrhenius figure shown in Fig. B.4 [125].

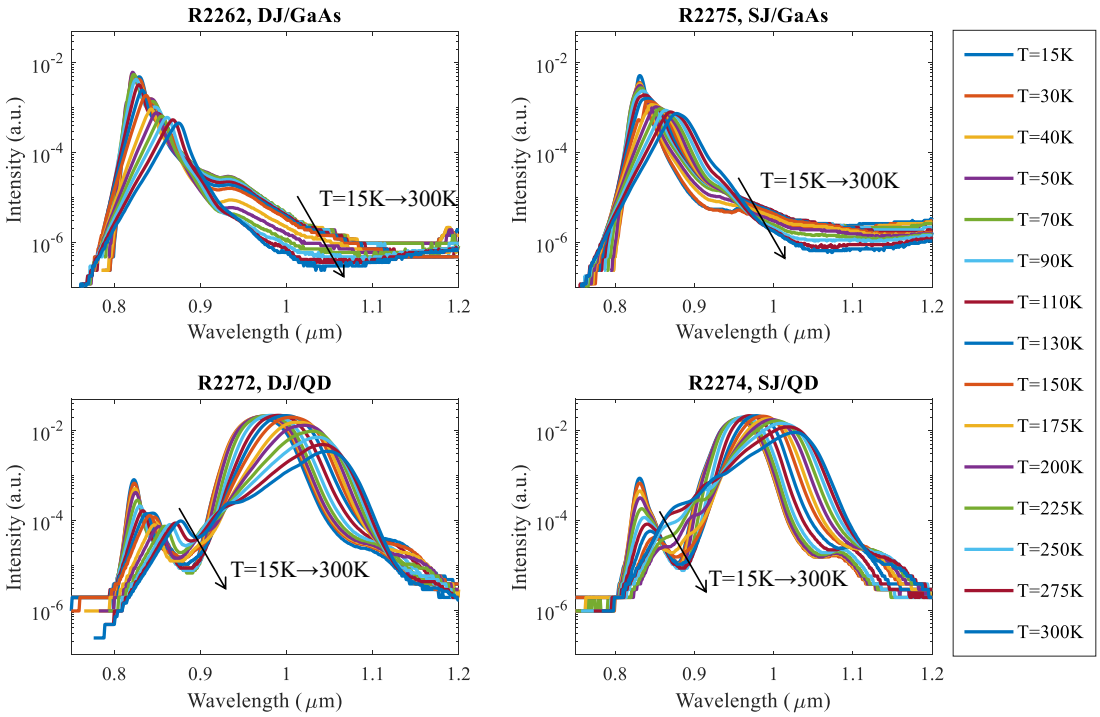

Figure B.3: Spectral PL intensity measurements at varying temperatures for the samples after etching of the GaAs contact layer.

Figure B.4 allows the observation of the trends predicted using the Varshni model, in which there is a visible shift of the peak energy when the temperature is varied, corresponding to a shift of the band-edge. In addition, the integrated intensity and the full width at half maximum show visible variation at the different temperatures as described in the modified Arrhenius formula. Accordingly, the measurements are processed to quantify the variations relative to the temperature.

Initially, the validity of the results is checked by comparing the Varshni parameters of the reference GaAs samples with those found in the literature [126]. A previous analysis found in [127] provided Varshni parameters of α_v=0.5405 meV/K and β_v=204 K. Another study in [128] used ellipsometry to produce a Varshni parameter set comprising of $E_g(T = 0)$=1.517 eV, α_v=0.55 meV/K and β_v=225 K. More recent parameter sets proposed by [129] and [130], which are obtained using photoluminescence measurements, result in $E_g(T = 0)$=1.519 eV, α_v=0.895–1.06 meV/K and β_v=538–671 K. In contrast, the performed measurements of the reference GaAs solar cell samples result in α_v=0.5 meV/K and β_v=250 K, which is in line with the values in the literature. A plot showing the peak energy shift of the GaAs samples relative to temperature variation is shown in Fig. B.5 (a), along with plots utilizing the mentioned GaAs Varshni parameters from the literature. In addition, the peak energy shift of the QDSC samples is displayed in Fig. B.5

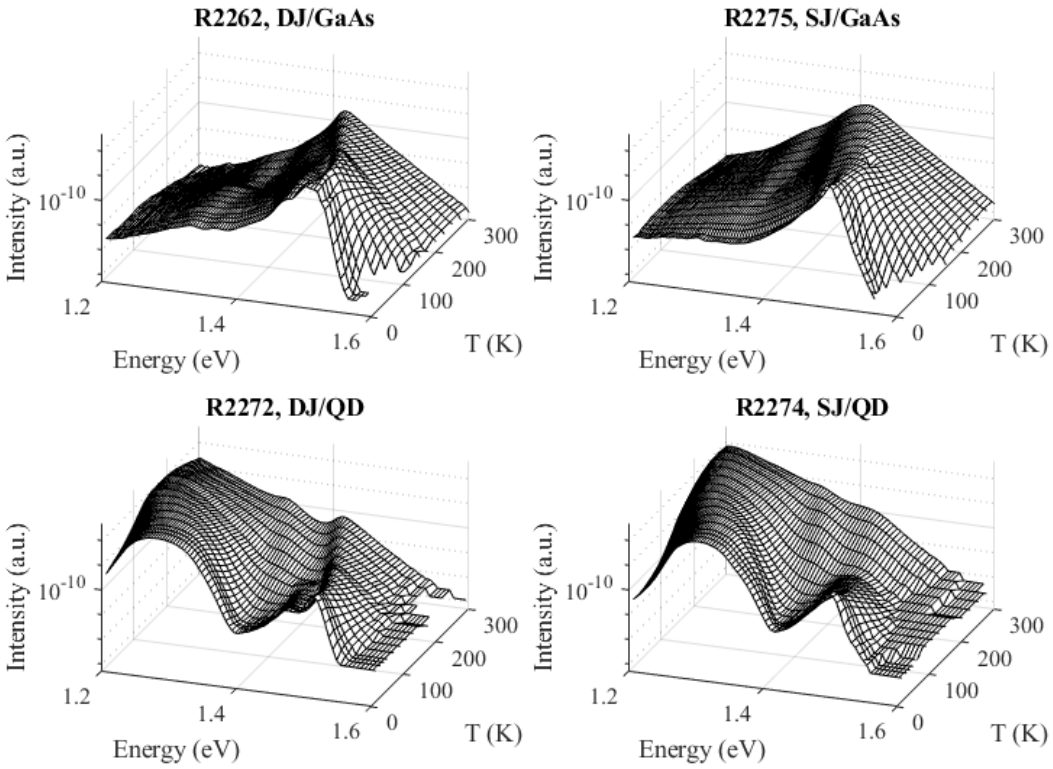

Figure B.4: Measured spectral PL intensity vs. energy vs. temperature, exhibiting the behavior predicted by the Varshni and Arrhenius models.

(b), demonstrating similar trends for an estimated $E_g(T = 0)$ of around 1.275–1.3 eV. The fitting of the measured GaAs and QD samples provides the parameters described in Table B.2.

Table B.2: Fitted parameters extracted from PL peak energy measurements.

Sample	$E_g(T = 0)$ (eV)	α_v (meV/K)	β_v (K)
R2262, DJ/GaAs	1.495	0.5	250
R2272, DJ/QD	1.275	0.5	250
R2274, SJ/QD	1.297	0.5	250
R2275, SJ/GaAs	1.51	0.5	250

Next, the integrated photoluminescence (IPL) is investigated for the temperature varied PL spectra. The IPL is analyzed for the QDSC samples, as shown in Fig. B.6. It is suggested in [121] that the temperature dependence of the radiative

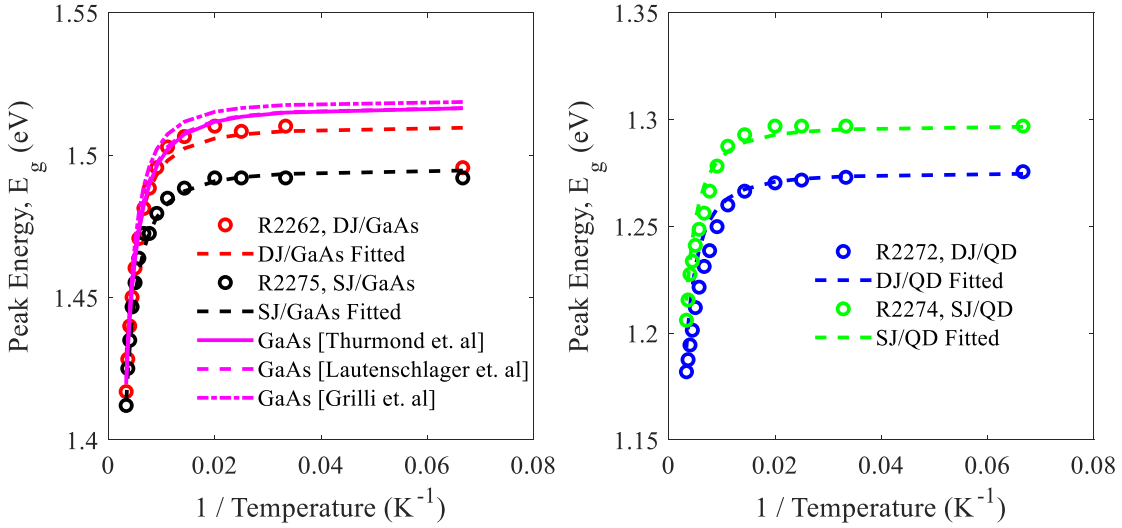

Figure B.5: The variation in the peak energy is shown vs. temperature, indicating the energy gap E_g shift according to Varshni's law. GaAs and InAs measurements are fitted and compared to GaAs Varshni parameters obtained from the literature.

carrier lifetime (derived using Eqn. B.3) is relatively constant for the QD states, and only becomes relevant at very high values of InAs coverage, which is not applicable to the studied samples. The activation energy E_a is therefore estimated through using the standard Arrhenius formula in Eqn. B.2 by plotting the natural logarithm of the integrated intensity ratio as $\ln(\frac{\int I_{T=0}}{\int I} - 1)$ against the inverse temperature T^{-1}, and obtaining the slope for each range of temperatures [131]. After obtaining the slopes, they are multiplied by the constant $-k_\mathrm{B}$ to compute E_a.

The temperature range was divided into three segments: 15–50 K, 70–110 K, and 130–300 K. The patterns shown by the measured samples are consistent with the literature [123]. In the low temperature regime, the IPL is relatively constant. In the intermediate temperature regime, the IPL begins to decrease and occasionally kinks may be observed. In the high temperature regime, the curve approaches a straight line indicating exponential quenching caused by thermal escape from the quantum dots. Therefore, the activation energy is commonly estimated at the high temperature regime, and the range used to estimate the activation energy is 130–300 K. The estimated values of E_a are listed in Table B.3. Future measurements could be performed at even higher excitation intensities, which possibly suppresses the irregularities in the temperature-dependent PL characteristics in QW structures [132].

Additional parameters such as the peak intensity and the full width at half maximum (FWHM) can also be extracted, which are displayed in Fig. B.7. The peak intensity demonstrates typical behavior for all samples, where it increases

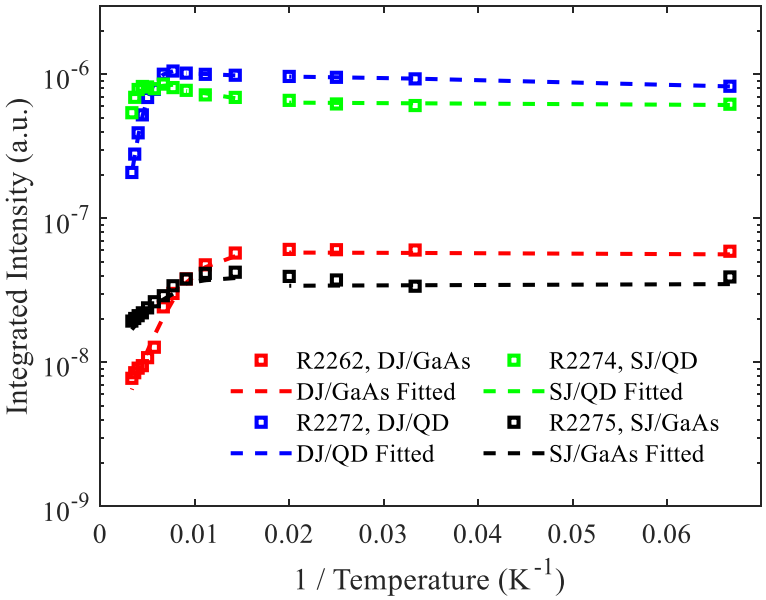

Figure B.6: The temperature dependent integrated intensity is fitted to obtain the activation energy from the slopes at different temperature ranges. The activation energy is extracted from the temperature range 130–300 K for the QDSC and GaAs reference samples.

Table B.3: Extracted activation energies for the different samples from temperature-dependent PL measurements in the high temperature regime (130–300 K).

Sample	E_a (meV)
R2262, DJ/GaAs	38
R2272, DJ/QD	104
R2274, SJ/QD	42
R2275, SJ/GaAs	29

exponentially with a linearly decreasing temperature, and then converges to a constant value at a temperature of around 100 K. The FWHM of the GaAs samples in Fig. B.7 (b) also exhibits a typical trend, where it decreases until converging to a constant value around lower temperatures. The DJ/QD sample exhibits a mean FWHM of 0.0715 eV and a standard deviation of 4.5 meV while the SJ/QD exhibits a mean FWHM of 0.0652 eV and standard deviation of 4.2 meV. However, the FWHM of the QDSC samples shows a significant kink at higher temperatures, which is consistent with other studies in the literature [122].

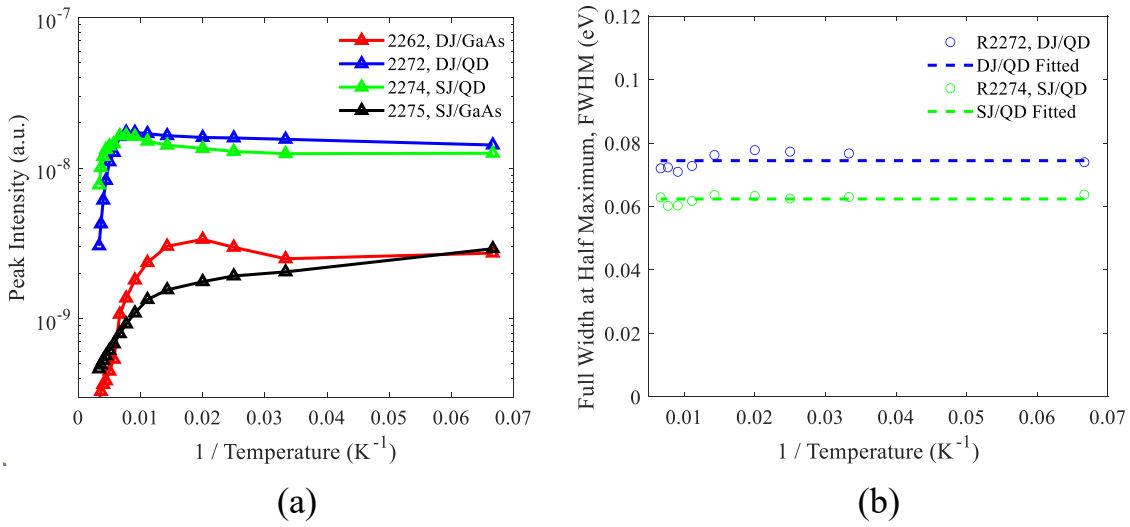

Figure B.7: (a) The peak intensity and (b) full width at half maximum (FWHM) are plotted against the temperature variation for the different samples and the temperature-dependent behavior is analyzed with reference to observed trends the literature.

The measurements of the PL response at room temperature were then repeated for varying excitation intensities (controlled using the attenuation wheel). The PL spectra of the different GaAs and QD samples for different laser powers are displayed in Fig. B.8. At lower excitation intensity, the measured signal becomes very low and the background noise becomes the limiting factor. Nevertheless, the final measurement range is over one order of magnitude, which is sufficient for the study.

The PL intensity is integrated and plotted versus the excitation power, as shown in Fig. B.9. The measured points are fitted and the slope is calculated in order to provide an estimate of the IF. The resulting values of IF for the different samples are detailed in Table B.4. The GaAs reference cells demonstrate IF values closer to 1 than the QD samples due to reduced defects that result in recombination mechanisms. In addition, the SJ configuration also provides improved IF for both the reference GaAs and the QD samples relative to the DJ configuration.

B.5 Future QDSC characterization activities

A preliminary study of experimentally characterizing QDSCs was performed in order to provide more accurate parameters for electrical modelling. The characterization was performed using temperature and excitation density dependent photoluminescence measurements of the available QDSC samples. Future work

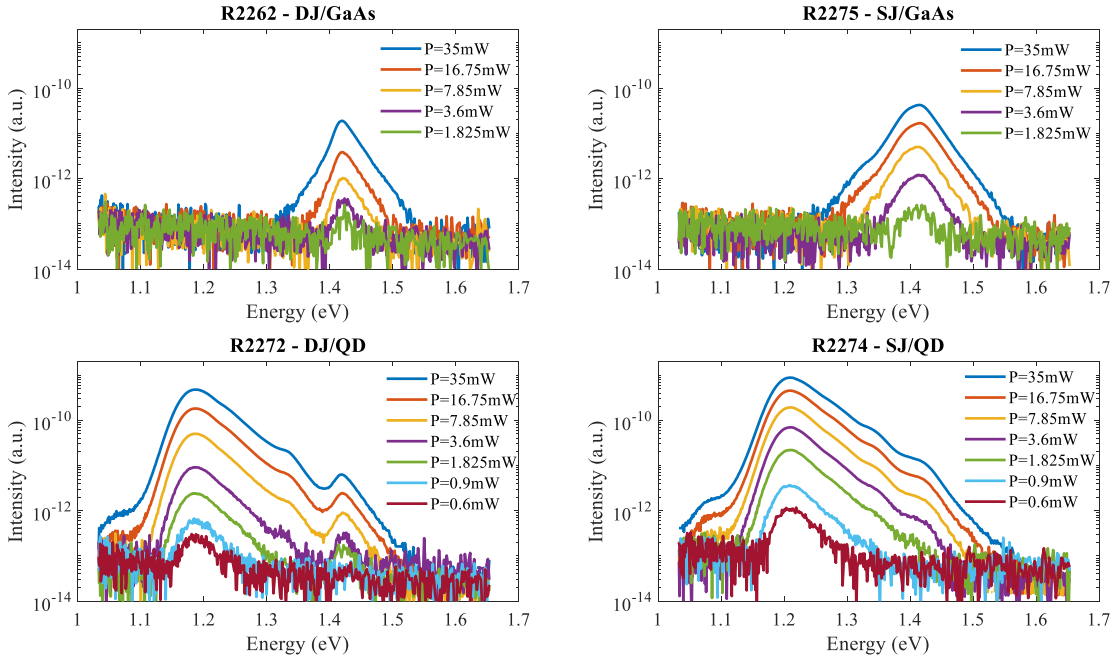

Figure B.8: The measured PL spectra are shown at varied excitation power for the QDSC and GaAs samples at room temperature.

Table B.4: Extracted ideality factors for the different samples from variable excitation PL measurements at room temperature.

Sample	IF
R2262, DJ/GaAs	1.24
R2272, DJ/QD	1.90
R2274, SJ/QD	1.65
R2275, SJ/GaAs	1.59

involves the integration of the extracted parameters into updated QD models.

In addition, further parameters can be extracted using different excitation methods (i.e. resonant excitation) as well as by characterizing undoped samples. The estimation of radiative and non radiative recombination rates of the QDSCs would also be useful. Finally, repeating the temperature analysis at higher excitation intensity could be improve the accuracy of the PL results by eliminating kinks in the PL spectra.

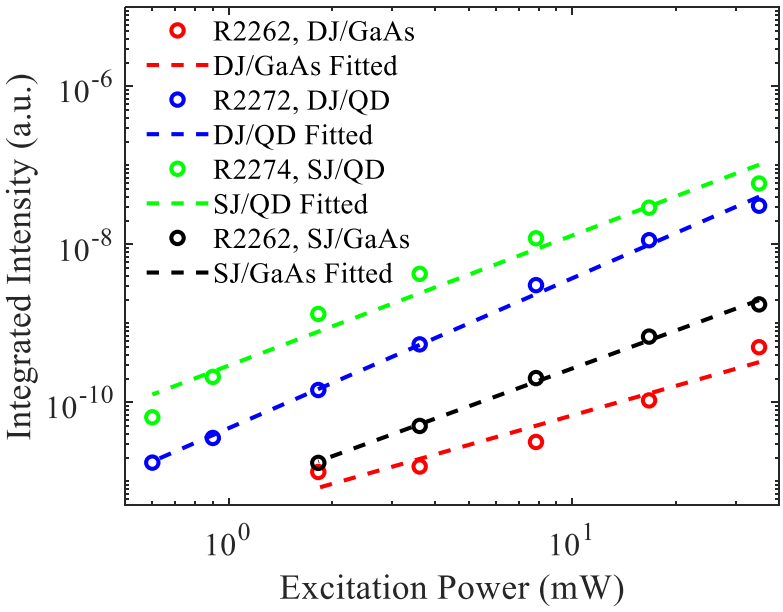

Figure B.9: The measured integrated intensity for the different samples relative to the excitation power is shown, for measurements performed at room temperature. The integrated intensity is fitted to obtain the slope, indicating the IF.

Bibliography

[1] M. A. Green et al. “Solar cell efficiency tables (version 50)”. In: *Prog. Photovolt.* 25.7 (2017), pp. 668–676.

[2] W. Shockley and H. J. Queisser. “Detailed balance limit of efficiency of p-n junction solar cells”. In: *J. Appl. Phys.* 32.3 (1961), pp. 510–519.

[3] E. D. Jackson. *Transactions of the Conference on the Use of Solar Energy-the Scientific Basis*. University of Arizona Press, 1955, pp. 122–126.

[4] N. J. Ekins-Daukes. “III-V Solar Cells”. In: *Solar Cell Materials* (2014), p. 113.

[5] A. Martì and G. L. Araujo. “Limiting efficiencies for photovoltaic energy conversion in multigap systems”. In: *Sol. Energy Mater. Sol. Cells* 43.2 (1996), pp. 203–222.

[6] F. Cappelluti et al. “Enabling high-efficiency inas/gaas quantum dot solar cells by epitaxial lift-off and light management”. In: *2017 IEEE 44th Photovoltaic Specialist Conference (PVSC)*. IEEE. 2017, pp. 1189–1192.

[7] A. Luque and A. Martì. “Increasing the Efficiency of Ideal Solar Cells by Photon Induced Transitions at Intermediate Levels”. In: *Phys. Rev. Lett.* 78.26 (1997), pp. 5014–5017.

[8] P. Würfel and U. Würfel. *Physics of solar cells: from basic principles to advanced concepts*. J. Wiley & Sons, 2009.

[9] T. Tiedje et al. “Limiting efficiency of silicon solar cells”. In: *IEEE Trans. Electron Devices* 31.5 (1984), pp. 711–716.

[10] G. Lush and M. Lundstrom. “Thin film approaches for high-efficiency III–V cells”. In: *Solar cells* 30.1-4 (1991), pp. 337–344.

[11] S. Mokkapati and K. R. Catchpole. “Nanophotonic light trapping in solar cells”. In: *J. Appl. Phys.* 112.10 (2012), p. 101101.

[12] M. L. Brongersma, Y. Cui, and S. Fan. “Light management for photovoltaics using high-index nanostructures”. In: *Nature materials* 13.5 (2014), p. 451.

[13] A. Mellor et al. “The feasibility of high-efficiency InAs/GaAs quantum dot intermediate band solar cells”. In: *Sol. Energy Mater. Sol. Cells* 130 (2014), pp. 225–233.

[14] T. Inoue et al. “Enhanced light trapping in multiple quantum wells by thin-film structure and backside grooves with dielectric interface”. In: *IEEE J. Photovolt.* 5.2 (2015), pp. 697–703.

[15] A. P. Cedola et al. “Physics-Based Modeling and Experimental Study of Si-Doped InAs/GaAs Quantum Dot Solar Cells”. In: *Int. J. Photoenergy* 2018 (2018).

[16] E. Yablonovitch and G. D. Cody. “Intensity enhancement in textured optical sheets for solar cells”. In: *IEEE Trans. Electron Devices* 29.2 (1982), pp. 300–305.

[17] P. Campbell and M. A. Green. “Light trapping properties of pyramidally textured surfaces”. In: *J. Appl. Phys.* 62.1 (1987), pp. 243–249.

[18] O. D. Miller, E. Yablonovitch, and S. R. Kurtz. “Strong internal and external luminescence as solar cells approach the Shockley–Queisser limit”. In: *IEEE J. Photovolt.* 2.3 (2012), pp. 303–311.

[19] K. Bittkau et al. “Nanoscale investigation of light-trapping in a-Si: H solar cell structures with randomly textured interfaces”. In: *Phys. Status Solidi (a)* 205.12 (2008), pp. 2766–2776.

[20] J. Krč et al. “Effect of surface roughness of ZnO: Al films on light scattering in hydrogenated amorphous silicon solar cells”. In: *Thin solid films* 426.1-2 (2003), pp. 296–304.

[21] O. Kluth et al. “Texture etched ZnO: Al coated glass substrates for silicon based thin film solar cells”. In: *Thin solid films* 351.1-2 (1999), pp. 247–253.

[22] P. Kowalczewski, M. Liscidini, and L. C. Andreani. “Light trapping in thin-film solar cells with randomly rough and hybrid textures”. In: *Opt. Express* 21.105 (2013), A808–A820.

[23] H. Feng Lu et al. “Plasmonic quantum dot solar cells for enhanced infrared response”. In: *Appl. Phys. Lett.* 100.10 (2012), p. 103505.

[24] P. Spinelli et al. “Plasmonic light trapping in thin-film Si solar cells”. In: *J. Opt.* 14.2 (2012), p. 024002.

[25] H. A. Atwater and A. Polman. “Plasmonics for improved photovoltaic devices”. In: *Materials For Sustainable Energy: A Collection of Peer-Reviewed Research and Review Articles from Nature Publishing Group*. World Scientific, 2011, pp. 1–11.

[26] P. Bermel et al. “Improving thin-film crystalline silicon solar cell efficiencies with photonic crystals”. In: *Opt. Express* 15.25 (2007), pp. 16986–17000.

[27] Y. Yi et al. *Light trapping in thin film solar cells using textured photonic crystal*. US Patent 7,482,532. Jan. 2009.

[28] Y. C. Lee et al. "Enhanced light trapping based on guided mode resonance effect for thin-film silicon solar cells with two filling-factor gratings". In: *Opt. Express* 16.11 (2008), pp. 7969–7975.

[29] T. Khaleque and R. Magnusson. "Light management through guided-mode resonances in thin-film silicon solar cells". In: *Journal of Nanophotonics* 8.1 (2014), pp. 083995–083995.

[30] S. Manzoor et al. "Revisiting light trapping in silicon solar cells with random pyramids". In: *2016 IEEE 43rd Photovoltaic Specialists Conference (PVSC)*. IEEE. 2016, pp. 2952–2954.

[31] A. Musu et al. "Nanostructures for light management in thin-film GaAs quantum dot solar cells". In: *Solid-State Lighting*. Optical Society of America. 2016, JW4A–45.

[32] S. Turner et al. "Periodic dielectric structures for light-trapping in InGaAs/GaAs quantum well solar cells". In: *Opt. Express* 21.S3 (May 2013), A324–A335. DOI: 10.1364/OE.21.00A324.

[33] B. L. Smith et al. "Inverted growth evaluation for epitaxial lift off (ELO) quantum dot solar cell and enhanced absorption by back surface texturing". In: *Photovoltaic Specialists Conference (PVSC), 2016 IEEE 43rd*. IEEE. 2016, pp. 1276–1281.

[34] A. Mellor et al. "A numerical study of Bi-periodic binary diffraction gratings for solar cell applications". In: *Sol. Energy Mater. Sol. Cells* 95.12 (2011), pp. 3527–3535.

[35] A. Luque and A. Martì. "The intermediate band solar cell: progress toward the realization of an attractive concept". In: *Adv. Mater.* 22.2 (2010), pp. 160–174.

[36] Y. Okada et al. "Intermediate band solar cells: Recent progress and future directions". In: *Applied physics reviews* 2.2 (2015), p. 021302.

[37] G. Jolley et al. "The role of intersubband optical transitions on the electrical properties of InGaAs/GaAs quantum dot solar cells". In: *Prog. Photovolt: Res. Appl.* (2012). DOI: 10.1002/pip.2161.

[38] K. Tanabe et al. "High-efficiency InAs/GaAs quantum dot solar cells by metalorganic chemical vapor deposition". In: *Appl. Phys. Lett.* 100 (2012), pp. 1293905–193905-3.

[39] B. M. Kayes et al. "27.6% conversion efficiency, a new record for single-junction solar cells under 1 sun illumination". In: *Photovoltaic Specialists Conference (PVSC), 2011 37th IEEE*. IEEE. 2011, pp. 000004–000008.

[40] S. M. Hubbard et al. “Nanostructured photovoltaics for space power”. In: *Journal of Nanophotonics* 3.1 (2009), pp. 031880–031880.

[41] C. Kerestes et al. “Strain effects on radiation tolerance of triple-junction solar cells with InAs quantum dots in the GaAs junction”. In: *IEEE J. Photovoltaics* 4.1 (2013), pp. 224–232.

[42] V. Aroutiounian et al. “Quantum dot solar cells”. In: *JAP* 89.4 (2001), pp. 2268–2271.

[43] F. Cappelluti et al. “Light-trapping enhanced thin-film III-V quantum dot solar cells fabricated by epitaxial lift-off”. In: *Sol. Energy Mater. Sol. Cells* 181 (2018), pp. 83–92.

[44] F. Cappelluti et al. *Quantum Dot-Based Thin-Film III–V Solar Cells*. Springer, 2020.

[45] F. Cappelluti et al. “Numerical study of thin-film quantum-dot solar cells combining selective doping and light-trapping approaches”. In: *Photovoltaic Specialists Conference (PVSC), 2016 IEEE 43rd*. IEEE. 2016, pp. 1282–1286.

[46] G.J. Bauhuis et al. “26.1% thin-film GaAs solar cell using epitaxial lift-off”. In: *Sol. Energy Mater. Sol. Cells* 93.9 (2009), pp. 1488–1491.

[47] J. Tommila et al. “Nanostructured broadband antireflection coatings on AlInP fabricated by nanoimprint lithography”. In: *Sol. Energy Mater. Sol. Cells* 94.10 (2010), pp. 1845–1848.

[48] J. Tommila et al. “Moth-eye antireflection coating fabricated by nanoimprint lithography on 1 eV dilute nitride solar cell”. In: *Prog. Photovolt.* 21.5 (2013), pp. 1158–1162.

[49] F. Elsehrawy et al. “Improved Light Trapping in Quantum Dot Solar Cells Using Double-sided Nanostructuring”. In: *Optics and Photonics for Energy and the Environment*. Optical Society of America. 2018, JM4A–5.

[50] Y. Shoji, K. Watanabe, and Y. Okada. “Photoabsorption improvement in multi-stacked InGaAs/GaAs quantum dot solar cell with a light scattering rear texture”. In: *Sol. Energy Mater. Sol. Cells* 204 (2020), p. 110216.

[51] G. T. Nelson et al. “Modeling of practical light management for absorption enhancement in III-V multi-junction and quantum-dot solar cells”. In: *2018 IEEE 7th World Conference on Photovoltaic Energy Conversion (WCPEC)(A Joint Conference of 45th IEEE PVSC, 28th PVSEC & 34th EU PVSEC)*. IEEE. 2018, pp. 2913–2917.

[52] T. Aho et al. “Comparison of metal/polymer back reflectors with half-sphere, blazed, and pyramid gratings for light trapping in III-V solar cells”. In: *Opt. Express* 26.6 (2018), A331–A340.

[53] B. Lipovšek, J. Krč, and M. Topič. "Microtextured light-management foils and their optimization for planar organic and perovskite solar cells". In: *IEEE J. Photovolt.* 8.3 (2018), pp. 783–792.

[54] O. Isabella et al. "Advanced light trapping scheme in decoupled front and rear textured thin-film silicon solar cells". In: *J. Sol.* 162 (2018), pp. 344–356. ISSN: 0038-092X.

[55] S. E. Han and G. Chen. "Toward the Lambertian limit of light trapping in thin nanostructured silicon solar cells". In: *Nano Lett.* 10.11 (2010), pp. 4692–4696.

[56] H.L. Chen et al. "A 19.9%-efficient ultrathin solar cell based on a 205-nm-thick GaAs absorber and a silver nanostructured back mirror". In: *Nature Energy* 4.9 (2019), pp. 761–767.

[57] M. van Eerden et al. "A facile light-trapping approach for ultrathin GaAs solar cells using wet chemical etching". In: *Prog. Photovolt.* (2019).

[58] T. K. Chong et al. "Optimal wavelength scale diffraction gratings for light trapping in solar cells". In: *J. Opt.* 14.2 (2012), p. 024012.

[59] O. Isabella et al. "Front/rear decoupled texturing in refractive and diffractive regimes for ultra-thin silicon-based solar cells". In: *Optical Nanostructures and Advanced Materials for Photovoltaics*. Optical Society of America. 2013, PM4C–2.

[60] K. X. Wang et al. "Absorption enhancement in ultrathin crystalline silicon solar cells with antireflection and light-trapping nanocone gratings". In: *Nano Lett.* 12.3 (2012), pp. 1616–1619.

[61] A. Gaucher et al. "Ultrathin epitaxial silicon solar cells with inverted nanopyramid arrays for efficient light trapping". In: *Nano Lett.* 16.9 (2016), pp. 5358–5364.

[62] C. S. Schuster et al. "How to assess light trapping structures versus a Lambertian Scatterer for solar cells?" In: *Opt. Express* 22.102 (2014), A542–A551.

[63] E. E. Perl et al. "Ultrabroadband and wide-angle hybrid antireflection coatings with nanostructures". In: *IEEE J. Photovolt.* 4.3 (2014), pp. 962–967.

[64] H. K. Raut et al. "Anti-reflective coatings: A critical, in-depth review". In: *Energy Environ. Sci.* 4.10 (2011), pp. 3779–3804.

[65] L. A. Pettersson, L. S. Roman, and O. Inganäs. "Modeling photocurrent action spectra of photovoltaic devices based on organic thin films". In: *J. Appl. Phys.* 86.1 (1999), pp. 487–496.

[66] E. D. Palik. *Handbook of optical constants of solids*. Vol. 3. Academic press, 1998.

[67] Y. Jiang, S. Pillai, and M. A. Green. "Realistic silver optical constants for plasmonics". In: *Sci. Rep.* 6 (2016), p. 30605.

[68] M. Gioannini et al. "Simulation of quantum dot solar cells including carrier intersubband dynamics and transport". In: *IEEE J. Photovolt.* 3.4 (2013), pp. 1271–1278.

[69] CA Synopsys Inc. Mountain View. "RSoft diffractMOD User Guide". In: *v2016.09* (2016).

[70] J. P. Hugonin, R. Petit, and M. Cadilhac. "Plane-wave expansions used to describe the field diffracted by a grating". In: *JOSA* 71.5 (1981), pp. 593–598.

[71] M. G. Moharam and T. K. Gaylord. "Rigorous coupled-wave analysis of metallic surface-relief gratings". In: *JOSA A* 3.11 (1986), pp. 1780–1787.

[72] A. W. Walker et al. "Impact of photon recycling on GaAs solar cell designs". In: *IEEE J. Photovoltaics* 5.6 (2015), pp. 1636–1645.

[73] G. Bauhuis et al. "Deep junction III–V solar cells with enhanced performance". In: *Phys. Status Solidi (a)* 213.8 (2016), pp. 2216–2222.

[74] F. Elsehrawy, T. Niemi, and F. Cappelluti. "Guided-mode resonance gratings for enhanced mid-infrared absorption in quantum dot intermediate-band solar cells". In: *Opt. Express* 26.6 (2018), A352–A359.

[75] A. Zhang et al. "Advanced light-trapping effect of thin-film solar cell with dual photonic crystals". In: *Nanoscale research letters* 10.1 (2015), p. 214.

[76] D. F. Swinehart. "The beer-lambert law". In: *J. Chem. Educ.* 39.7 (1962), p. 333.

[77] Micro Resist Technology GmbH. *OrmoComp UV inprint*. Accessed: January 2018. URL: `http://www.microresist.de/en/product/hybrid-polymers-0`.

[78] M. Peters et al. "Electro–optical modelling of solar cells with photonic structures". In: *25th European PV Solar Energy Conference and Exhibition*. 2010, pp. 87–91.

[79] F. Elsehrawy et al. "Back grating optimization for light trapping in thin-film quantum dot solar cells". In: *19th Italian National Conference on Photonic Technologies (Fotonica 2017)*. IET Digital Library, 2017.

[80] A. Luque et al. "Operation of the intermediate band solar cell under nonideal space charge region conditions and half filling of the intermediate band". In: *J. Appl. Phys.* 99 (2006), p. 094503.

[81] K. Yoshida, Y. Okada, and N. Sano. "Self-consistent simulation of intermediate band solar cells: Effect of occupation rates on device characteristics". In: *Appl. Phys. Lett.* 97 (2010), p. 133503.

[82] R. Strandberg and T. Reenaas. "Optimal Filling of the Intermediate Band in Idealized Intermediate-Band Solar Cells". In: *Trans. Electron Dev.* 58.8 (2011), pp. 2559–2565.

[83] D.G. Sellers et al. "Analyzing carrier escape mechanisms in InAs/GaAs quantum dot p-i-n junction photovoltaic cells". In: *Applied Physics Letters* 104.22 (2014), p. 223903.

[84] K. Yoshida, Y. Okada, and N.Sano. ""Device simulation of intermediate band solar cells: effects of doping and concentration". In: *J. Appl. Phys.* 112 (2012), p. 084510.

[85] S. S. Wang et al. "Guided-mode resonances in planar dielectric-layer diffraction gratings". In: *JOSA A* 7.8 (1990), pp. 1470–1474.

[86] C. C. Wang and S. D. Lin. "Resonant cavity-enhanced quantum-dot infrared photodetectors with sub-wavelength grating mirror". In: *J. Appl. Phys.* 113.21 (2013), p. 213108.

[87] E. E. Perl et al. "Design of antireflective nanostructures and optical coatings for next-generation multijunction photovoltaic devices". In: *Opt. Express* 22.105 (2014), A1243–A1256.

[88] Y. Harada, T. Maeda, and T. Kita. "Intraband carrier dynamics in InAs/GaAs quantum dots stimulated by bound-to-continuum excitation". In: *J. Appl. Phys.* 113.22 (2013), p. 223511.

[89] A. Cattoni. "Multi-resonant light trapping in ultra-thin solar cells (Conference Presentation)". In: *Photonics for Solar Energy Systems VII*. Vol. 10688. International Society for Optics and Photonics. 2018, p. 106880I.

[90] F. Elsehrawy, A. Tibaldi, and F. Cappelluti. "Efficient multiphysics modeling of thin-film solar cells with periodically textured surfaces". In: *Physics, Simulation, and Photonic Engineering of Photovoltaic Devices VIII*. Vol. 10913. International Society for Optics and Photonics. 2019, 109130K.

[91] P. Bermel. "Photon management modeling and beyond for photovoltaics". In: *Opt. Commun.* 314 (2014), pp. 66–70.

[92] S. M. Durbin and J. L. Gray. "Numerical modeling of photon recycling in solar cells". In: *IEEE Trans. Electron Devices* 41.2 (1994), pp. 239–245.

[93] G. Letay, M. Hermle, and A. W. Bett. "Simulating single-junction GaAs solar cells including photon recycling". In: *Prog. Photovolt.* 14.8 (2006), pp. 683–696.

[94] R. Rumpf. "Improved formulation of scattering matrices for semi-analytical methods that is consistent with convention". In: *Prog. Electromagn. Res.* 35 (2011), pp. 241–261.

[95] R. Orta, A. Tibaldi, and P. Debernardi. "Bimodal resonance phenomena–part I: generalized Fabry–Perot interferometers". In: *IEEE J. Quantum Electron.* 52.12 (2016), pp. 6100508-1–8.

[96] M. Topič et al. "Approaches and challenges in optical modelling and simulation of thin-film solar cells". In: *Sol. Energy Mater. Sol. Cells* 135 (2015), pp. 57–66.

[97] J. Krč et al. "Optical Modelling and Simulations of Thin-Film Silicon Solar Cells". In: *Photovoltaic Modeling Handbook* (2018), pp. 93–140.

[98] T. Tamir and S. Zhang. "Modal transmission-line theory of multilayered grating structures". In: *IEEE J. Light. Technol.* 14.5 (1996), pp. 914–927.

[99] A. Tibaldi, P. Debernardi, and R. Orta. "High-contrast gratings performance issues in tunable VCSELs". In: *IEEE J. Quantum Electron.* 51.12 (2015), pp. 2400407-1–8.

[100] A. Khalili et al. "Multiscale device simulation of quantum dot solar cells". In: *Physics, Simulation, and Photonic Engineering of Photovoltaic Devices VIII*. Vol. 10913. International Society for Optics and Photonics. 2019, 109131N.

[101] P. Pettersson. *Modelling and verification of real-time systems using timed automata: theory and practice*. Department of Computer systems, Univ., 1999.

[102] H. A. Macleod. *Thin-film optical filters*. CRC press, 2010.

[103] E. Peral and J. Capmany. "Generalized Bloch wave analysis for fiber and waveguide gratings". In: *IEEE J. Light. Technol.* 15.8 (1997), pp. 1295–1302.

[104] K. S. Chiang. "Effective-index analysis of optical waveguides". In: *Physics and Simulation of Optoelectronic Devices III*. Vol. 2399. International Society for Optics and Photonics. 1995, pp. 2–12.

[105] L. Li. "Multilayer modal method for diffraction gratings of arbitrary profile, depth, and permittivity". In: *JOSA A* 10.12 (1993), pp. 2581–2591.

[106] E. Noponen and J. Turunen. "Eigenmode method for electromagnetic synthesis of diffractive elements with three-dimensional profiles". In: *JOSA A* 11.9 (1994), pp. 2494–2502.

[107] A. Taflove and S. C. Hagness. *Computational electrodynamics: the finite-difference time-domain method*. Artech house, 2005.

[108] K. Yee. "Numerical solution of initial boundary value problems involving Maxwell's equations in isotropic media". In: *IEEE Trans. Antennas Propag.* 14.3 (1966), pp. 302–307.

[109] Lumerical Inc. Y. H. Chen. *Simulations with silver*. Published: March 2019. URL: `https://kx.lumerical.com/t/simulations-with-silver/32025`.

[110] J. Nelson et al. “Observation of suppressed radiative recombination in single quantum well pin photodiodes”. In: *J. Appl. Phys.* 82.12 (1997), pp. 6240–6246.

[111] J. Nelson. *The physics of solar cells*. World Scientific Publishing Company, 2003.

[112] S. M. Sze. “Physics of Semiconductor Devices, Jhon Wiley &”. In: *New York* (1981), pp. 96–98.

[113] M. P. Lumb et al. “Incorporating photon recycling into the analytical drift-diffusion model of high efficiency solar cells”. In: *J. Appl. Phys.* 116.19 (2014), p. 194504.

[114] F. Cappelluti, M. Gioannini, and A. Khalili. “Impact of doping on InAs/GaAs quantum-dot solar cells: a numerical study on photovoltaic and photoluminescence behavior”. In: *Sol. Energy Mater. Sol. Cells* 157 (2016), pp. 209–220.

[115] G. Jolley et al. “The role of intersubband optical transitions on the electrical properties of InGaAs/GaAs quantum dot solar cells”. In: *Prog. Photovolt.* 21.4 (2013), pp. 736–746.

[116] J. Hwang et al. “Thermal emission in type-II GaSb/GaAs quantum dots and prospects for intermediate band solar energy conversion”. In: *J. Appl. Phys.* 111.7 (2012), p. 074514.

[117] H. Lee, W. Yang, and P. C. Sercel. “Temperature and excitation dependence of photoluminescence line shapein InAs/GaAs quantum-dot structures”. In: *Phys. Rev. B* 55.15 (1997), p. 9757.

[118] G. C. Shan et al. “Single photon sources with single semiconductor quantum dots”. In: *Front. Phys.* 9.2 (2014), pp. 170–193.

[119] Y. P. Varshni. “Temperature dependence of the energy gap in semiconductors”. In: *physica* 34.1 (1967), pp. 149–154.

[120] Y. Fang et al. “Investigation of temperature-dependent photoluminescence in multi-quantum wells”. In: *Sci. Rep.* 5 (2015), p. 12718.

[121] C. G. Bailey et al. “Temperature dependent photoluminescence spectroscopy of InAs/GaAs solar cells”. In: *2010 35th IEEE Photovoltaic Specialists Conference*. IEEE. 2010, pp. 000364–000369.

[122] T. E. Nee et al. “Temperature and excitation dependence of photoluminescence spectra of InAs/GaAs quantum dot heterostructures”. In: *2006 IEEE Conference on Emerging Technologies-Nanoelectronics*. IEEE. 2006, pp. 433–437.

[123] E. C. Le Ru, J. Fack, and R. Murray. "Temperature and excitation density dependence of the photoluminescence from annealed InAs/GaAs quantum dots". In: *Phys. Rev. B* 67.24 (2003), p. 245318.

[124] A. Tukiainen et al. "Comparison of 'shallow'and 'deep'junction architectures for MBE-grown InAs/GaAs quantum dot solar cells". In: *2018 IEEE 7th World Conference on Photovoltaic Energy Conversion (WCPEC)(A Joint Conference of 45th IEEE PVSC, 28th PVSEC & 34th EU PVSEC)*. IEEE. 2018, pp. 2950–2952.

[125] J. V. Li et al. "Measuring temperature-dependent activation energy in thermally activated processes: A 2D Arrhenius plot method". In: *Rev. Sci. Instrum.* 81.3 (2010), p. 033910.

[126] I. Vurgaftman, J. R. Meyer, and L. R. Ram-Mohan. "Band parameters for III–V compound semiconductors and their alloys". In: *J. Appl. Phys.* 89.11 (2001), pp. 5815–5875.

[127] C. D. Thurmond. "The standard thermodynamic functions for the formation of electrons and holes in Ge, Si, GaAs, and GaP". In: *J. Electrochem. Soc.* 122.8 (1975), pp. 1133–1141.

[128] P. Lautenschlager et al. "Interband critical points of GaAs and their temperature dependence". In: *Phys. Rev. B* 35.17 (1987), p. 9174.

[129] E. Grilli et al. "High-precision determination of the temperature dependence of the fundamental energy gap in gallium arsenide". In: *Phys. Rev. B* 45.4 (1992), p. 1638.

[130] M. El Allali et al. "Experimental determination of the GaAs and Ga 1- x Al x As band-gap energy dependence on temperature and aluminum mole fraction in the direct band-gap region". In: *Phys. Rev. B* 48.7 (1993), p. 4398.

[131] M. Leroux et al. "Temperature quenching of photoluminescence intensities in undoped and doped GaN". In: *J. Appl. Phys.* 86.7 (1999), pp. 3721–3728.

[132] C. Cetinkaya et al. "Optical properties of n-and p-type modulation doped GaAsBi/AlGaAs quantum well structures". In: *J. Alloys Compd.* 739 (2018), pp. 987–996.